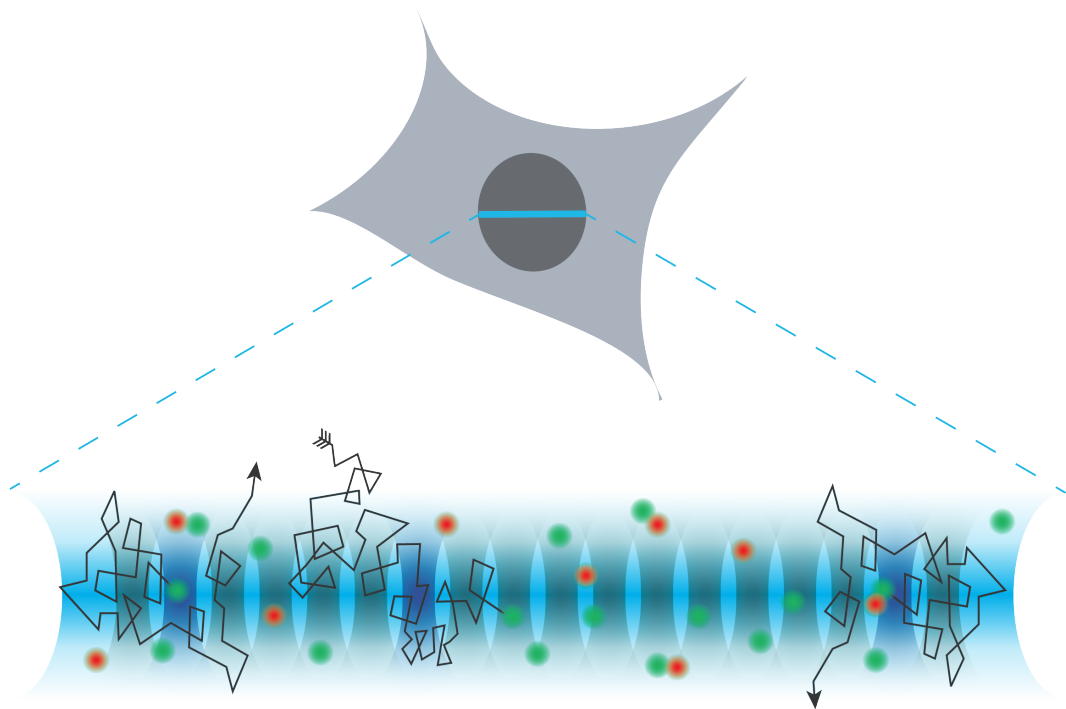


**Protein Mobility and Interaction Measurements  
in Living Cells by Dual-Color Multi-Focus  
Fluorescence Cross-Correlation Spectroscopy**



**Dissertation submitted by  
Michael Baum**









**Dissertation**  
**submitted to the**  
**Combined Faculties for the Natural Sciences and for Mathematics**  
**of the Ruperto-Carola University of Heidelberg, Germany**  
**for the degree of**  
**Doctor of Natural Sciences**

**Put forward by**

**Dipl.-Phys. Michael Baum**  
**Born in Schwäbisch Hall**  
**Oral examination: 21.05.2014**



**Protein Mobility and Interaction Measurements  
in Living Cells by Dual-Color Multi-Focus  
Fluorescence Cross-Correlation Spectroscopy**

**Referees:**

**PD Dr. Karsten Rippe**

**Prof. Dr. Ulrich Schwarz**



## **Proteinmobilitäts- und Interaktionsmessungen mithilfe von Zwei-Farben-Multi-Fokus-Fluoreszenz-Kreuzkorrelations-Spektroskopie in lebenden Zellen**

Das Innere lebender Zellen ist ein dicht gepacktes und heterogenes Medium, das aus festen Strukturen und einer einbettenden viskosen Flüssigkeit besteht. In dieser komplexen Umgebung sind der Transport und die Interaktionen von Proteinen räumlich moduliert. Außerdem werden anormale Phänomene des Proteintransportes in lebenden Zellen beobachtet, die Einfluss auf die Kinetik biologischer Reaktionen und die Effizienz von Suchprozessen haben. Für das Verständnis des anomalen Proteintransportes in Zellen muss die Mobilität von Proteinen mit hoher Auflösung auf multiplen Skalen aufgenommen werden. In dieser Arbeit werden experimentelle und theoretische Grundlagen für parallele Mobilitätsmessungen auf vielen Längenskalen durch Fluoreszenz-Korrelations-Spektroskopie mit linien-konfokalen Mikroskopen entwickelt. Aufgenommene Fluoreszenzsignale werden entweder für Proteinmobilitätskartierungen autokorreliert oder zur Bestimmung der Permeabilität intrazellulärer Strukturen kreuzkorreliert. Diese Methodik wird zur Kartierung der skalenabhängigen Mobilität von Monomeren und Multimeren des inerten grün fluoreszierenden Proteins (GFP) im Cytoplasma und Zellkern lebender Zellen genutzt. Darüber hinaus wird aus der Zeitabhängigkeit des apparenten Diffusionskoeffizienten extrahiert, dass die Struktur der intrazellulären Umgebung der eines porösen Mediums gleicht. Die hier entwickelte Methodik liefert auf multiplen Skalen quantitative Daten für Mobilität und Interaktionen, die in der Systembiologie für das Verständnis der funktionellen Organisation lebender Zellen verwendet werden können.

## **Protein mobility and interaction measurements in living cells by dual-color multi-focus fluorescence cross-correlation spectroscopy**

The interior of living cells is a crowded and heterogeneous medium that consists of solid structures and an embedding viscous fluid. In this complex environment, protein transport and interactions are spatially modulated. Further, anomalous protein transport phenomena are observed in living cells that impact on the kinetics of biological reactions and efficiency of target search processes. To understand anomalous protein transport in cells, protein mobility has to be mapped with high resolution on multiple scales. In this thesis, an experimental and theoretical framework for parallelized mobility measurements on multiple length scales by fluorescence correlation spectroscopy with line confocal microscopes is developed. Acquired fluorescence signals are either auto-correlated for protein mobility mapping or cross-correlated to probe the permeability of the intracellular structure. By applying this methodology, the scale-dependent mobility of inert green fluorescent protein (GFP) monomers and multimers is mapped in the cytoplasm and nucleus of living cells. Furthermore, it is retrieved from the time dependence of measured apparent diffusion coefficients that the structure of the intracellular environment appears as that of a porous medium. The methodology developed here yields quantitative mobility and interaction data on multiple scales that can be used in systems biology for understanding the functional organization of living cells.



# Contents

<b>I Introduction.....</b>	<b>1</b>
<b>II Theory .....</b>	<b>3</b>
II.1 Diffusion .....	3
II.1.1 Normal diffusion.....	3
II.1.2 Anomalous diffusion .....	9
II.1.3 Confined diffusion.....	12
II.2 Confocal fluorescence microscopy.....	13
II.2.1 Fluorescence .....	13
II.2.2 Confocal laser scanning microscopy .....	14
II.2.3 Molecule detection efficiency of confocal microscopes .....	16
II.3 Fluorescence fluctuation microscopy techniques .....	20
II.3.1 Fluorescence recovery after photobleaching .....	21
II.3.2 Fluorescence correlation spectroscopy .....	24
II.3.3 Dual-color fluorescence cross-correlation spectroscopy .....	26
II.3.4 Dual-focus fluorescence cross-correlation spectroscopy.....	29
II.3.5 Scanning FCS and pair-correlation analysis.....	32
II.3.6 Multi-focus fluorescence (cross-) correlation spectroscopy .....	33
<b>III Biological background.....</b>	<b>35</b>
III.1 Cytoplasm.....	35
III.1.1 Cytoskeleton.....	35
III.1.2 Cytoplasmic organelles and vesicle traffic.....	36
III.1.3 Cytosol .....	36
III.2 Nucleus.....	37
III.2.1 Desoxyribonucleic acid .....	37
III.2.2 Chromatin fibers.....	38
III.2.3 Higher order chromatin structures.....	38
III.3 STAT signalling to chromatin as response to viral infections .....	41
<b>IV Results .....</b>	<b>42</b>
IV.1 Instrument characterization and reference measurements .....	42
IV.1.1 Correction of correlation curves' offset .....	42

IV.1.2 Impact of laser illumination intensity on measured mobility .....	43
IV.1.3 <i>In vitro</i> characterization and reference measurements .....	44
IV.2 Signal correction in Fourier space .....	49
IV.3 Improved MDE model for line-confocal microscopes .....	54
IV.3.1 Derivation of an MDE model function for line-confocal microscopes .....	54
IV.3.2 Derivation of a spatial cross-correlation function for double cone MDE.....	58
IV.3.3 Measurement of the MDE structural parameters .....	59
IV.4 Mobility and diffusion barrier mapping by 1D-FCS .....	68
IV.5 Mobility measurements on multiple time and length scales.....	75
IV.5.1 Inert GFP monomers and multimers in unperturbed living cells.....	75
IV.5.2 Mobility of inert GFP <sub>3</sub> after degradation of cytoskeletal filaments.....	84
IV.5.3 Mobility of inert GFP <sub>3</sub> after perturbations of the chromatin structure .....	86
IV.5.4 Non-inert and endogenous STAT2 proteins and chromodomains.....	88
IV.6 Protein interaction measurements by dual-color FCCS.....	90
IV.6.1 Reference measurements .....	90
IV.6.2 Dimerization of STAT1 and STAT2 proteins in the cytoplasm.....	93
<b>V Discussion.....</b>	<b>95</b>
V.1 Impact of the microscope's MDE on FCS measurement results .....	95
V.2 Anomalous diffusion measurements in living cells .....	97
V.3 Intracellular structure from a diffusing protein's point of view.....	101
V.4 Perspectives and conclusions .....	104
<b>VI Materials and Methods .....</b>	<b>106</b>
<b>VII References .....</b>	<b>110</b>



*“Can one hear the shape of a drum?”*

Mark Kac. (1966).  
Amer. Math. Monthly 73, 1-23.



## **Publications**

Baum M, Wachsmuth M, Erdel F & Rippe K. (2014).

*Mapping the intracellular structure from a diffusing protein's point of view.*

Nature Communications, under revision.

Erdel F, Müller-Ott K, Baum M, Wachsmuth M & Rippe K. (2011).

*Dissecting chromatin interactions in living cells from protein mobility maps.*

Chromosome Res. 19, 99-115.

## **Presentations**

Short talk and poster presentation.

*Seeing is Believing – Imaging the Processes of Life. (2013).*

European Molecular Biology Laboratory & Organization (EMBL & EMBO).

Talk and poster presentation.

*Third Biological Diffusion and Brownian Dynamics Brainstorm. (2013).*

Heidelberg Institute for Theoretical Studies (HITS).

Poster presentation.

*Seeing is Believing – Imaging the Processes of Life. (2011).*

European Molecular Biology Laboratory & Organization (EMBL & EMBO).



## Abbreviations

AC	Auto-Correlation
CC	Cross-Correlation
CLSM	Confocal Laser Scanning Microscopy
DLS	Dynamic Light Scattering
EM-CCD	Electron-Multiplying Charge-Coupled Device
FCS	Fluorescence Correlation Spectroscopy
FCCS	Fluorescence Cross-Correlation Spectroscopy
FRAP	Fluorescence Recovery After Photobleaching
GFP	Green Fluorescent Protein
HP1	Heterochromatin Protein 1
MDE	Molecule Detection Efficiency
MSD	Mean Squared Displacement
PFG-NMR	Pulsed Field Gradient Nuclear Magnetic Resonance
PSF	Point Spread Function
QDots	Quantum Dots
RFP	Red Fluorescent Protein
SPIM	Selective Plane Illumination Microscopy
STAT	Signal Transducer and Activator of Transcription
STED	Stimulated Emission Depletion
1D-FCS	One-Dimensional Fluorescence Correlation Spectroscopy
2D-FCS	Two-Dimensional Fluorescence Correlation Spectroscopy
3PEA	Pixel-wise Photobleaching Profile Evolution Analysis



# **I Introduction**

The interior of living cells is a crowded and highly heterogeneous environment (Ellis, 2001) that is composed of solid structures such as membrane-enclosed organelles, vesicles and cytoskeletal filaments in the cytoplasm or chromatin in the nucleus (Alberts et al., 2002). These intracellular structures are embedded by viscous fluid. In this complex medium, most proteins are randomly transported by diffusion to the sites where they are active (Gorski et al., 2006; Phair and Misteli, 2000). However, diffusive motions of proteins are hindered in living cells due to confining geometries and binding interactions. By surrounding highly accessible regions with dense materials that are barriers for diffusing molecules, cells can create specific reaction volumes and guide proteins like enzymes or transcription factors to sites where they are active. In addition to collisions with obstacles, proteins can form complexes or transiently bind to slowly moving cellular structures. Due to these microscopic interactions, the diffusion of molecules in living cells deviates significantly from that in homogeneous aqueous solutions (Hofling and Franosch, 2013; Wachsmuth et al., 2000; Weiss et al., 2003). It is spatially modulated and slowed down in a time and length scale dependent manner. Therefore, this kind of motion is called anomalous diffusion. For these anomalous transport phenomena, an increased rate of biological reactions and efficiency of target search processes was postulated (Guigas and Weiss, 2008). To study protein transport and interaction processes in living cells, it is important to map molecular mobility with high spatial and temporal resolution over a large time and length scale range.

To meet these high methodological demands, an experimental and theoretical framework for parallelized fluorescence correlation spectroscopy (FCS) measurements along a line in the sample, which is referred to as 1D-FCS, was developed in this thesis. It allowed for measuring protein mobility at hundreds of positions within a length scale range from 200 nm to 3.0  $\mu\text{m}$  at 50  $\mu\text{s}$  temporal resolution and 200 nm spatial resolution by line-confocal fluorescence microscopy. In the setup used here, a line in the sample is continuously illuminated with laser light. The emitted fluorescence light is recorded at equally spaced detection positions with a highly sensitive electron-multiplying charge-coupled device (EM-CCD) camera (Heuvelman et al., 2009). For protein mobility mapping, each acquired fluorescence signal is auto-correlated with a copy of itself and the calculated correlation

curves are fitted with model functions that describe the underlying transport process. Additionally, signals from different detection volume elements can be cross-correlated to measure molecule transport between them via a spatial FCCS analysis (Brinkmeier et al., 1999; Dertinger et al., 2007; Dittrich and Schwille, 2002). Cross-correlation analysis is used for imaging of diffusion barriers and permeability of intracellular structures (Digman and Gratton, 2009). In addition to spatial cross-correlation, signals from two spectral detection channels can be cross-correlated, which is referred to as dual-color fluorescence cross-correlation spectroscopy (dual-color FCCS) (Bacia et al., 2006; Rippe, 2000; Schwille et al., 1997; Weidemann et al., 2002). Such experiments can probe the interactions between proteins that were fluorescently labeled with different color, allowing for studying a protein's interaction kinetics.

The methodology developed here mapped the mobility of inert green fluorescent protein (GFP) monomers and multimers (Dross et al., 2009; Pack et al., 2006) in human U2OS cells to identify diffusion barriers. Since 1D-FCS with line-confocal microscopes measures diffusion of molecules on multiple length scales, their mean squared displacement (MSD) was reconstructed as a function of time. Scale-dependent diffusion of GFP monomers and multimers was measured in the cytoplasm and nucleus of living cells. The observed time dependence of the apparent diffusion coefficient was that for diffusion in porous media and revealed how the cellular environment was 'sensed' from a diffusing protein's point of view. Several structural parameters of the intracellular environment, e.g. the connectivity of the accessible space or the specific structure surface probed by the protein were retrieved. The drug-induced perturbances of these features and their effect on protein transport were evaluated with respect to the depolymerization of cytoskeletal filaments and the decondensation of chromatin. Furthermore, the time-dependence mobility of non-inert endogenous STAT2 signaling proteins (Stark and Darnell, 2012) was measured in the cytoplasm. In the nucleus, the mobility of chromatin-interacting heterochromatin protein 1 (HP1) (Grewal and Jia, 2007; Müller et al., 2009) and its isolated chromodomain was measured on multiple scales. Finally, interactions of STAT1 and STAT2 proteins in the cytoplasm of living U2OS cells were studied with dual-color FCCS analysis.

The methodology developed in this thesis lays the groundwork for a multi-scale spatial FCCS analysis of protein mobility and interactions in living cells. It can be easily transferred to recently emerging FCS techniques with single plane illumination microscopes (SPIM) (Capoulade et al., 2011; Singh et al., 2013; Wohland et al., 2010).



## II Theory

### II.1 Diffusion

In living cells, molecules are mostly randomly transported to sites where they are active by diffusion (Gorski et al., 2006; Phair and Misteli, 2000). Diffusion is a random movement of particles driven by thermal energy that is of the order of  $E_{\text{therm}} = k_{\text{B}}T$ , with the Boltzmann constant  $k_{\text{B}}$  and the absolute temperature  $T$  (Einstein, 1905). Due to frequent collisions with other moving particles, their momenta change continuously in direction and magnitude. Particle concentration gradients are equilibrated by diffusion (Fick, 1855). On the micrometer scale, spreading of particles in space by diffusion is a very efficient transport process. However, in complex and crowded media like the interior of living cells, free spreading of diffusing molecules is hindered due to collisions with immobile obstacles and adherence to cellular material due to transient binding interactions (Hofling and Franosch, 2013; Wachsmuth et al., 2000; Weiss et al., 2003). These microscopic processes result in anomalous diffusion phenomena that are different to normal diffusion in aqueous solution and dependent on the observation time and length scale. Only effective or apparent diffusion coefficients can be measured in living cells because of microscopic interactions.

#### II.1.1 Normal diffusion

##### II.1.1.1 Random walks

A theoretical approach to describe the random movement of molecules due to diffusion is the concept of so-called random walks (Berg, 1993; Stewart, 2001). Simple realizations of random walks are for example discrete movements of particles on two-dimensional Cartesian grids: Particles move randomly in one time step with equal probability from one grid vertex to one of the neighboring vertices. Each time step mimics a collision event with other diffusing particles. This model gives non-self-avoiding random walks, i.e. vertices can be visited arbitrarily often by particles. After  $n$  time steps, the net displacement of a particle is expressed by

$$\vec{r}(n) = \sum_{i=1}^n \vec{e}_i. \quad (\text{Eq. 1})$$

The unit vectors  $\vec{e}_i$  in Eq. 1 represent the  $i$ th time step of a random walker's trajectory on the grid. In this simplified model, only the direction of movement changes, whereas the step size is constant. Since particles move randomly from one grid vertex to another one with equal probability, different steps of their walks are not correlated (Bunde and Havlin, 1995):

$$\langle \vec{e}_i \cdot \vec{e}_j \rangle_{i \neq j} = 0. \quad (\text{Eq. 2})$$

Accordingly, the limit of the random walks' mean displacements after a large enough number  $n$  of time steps approaches zero:

$$\lim_{n \rightarrow \infty} (\vec{r}(n)) = \vec{0}. \quad (\text{Eq. 3})$$

Therefore, the mean squared displacements (MSD) of the random walks are used to characterize this random movement (Bunde and Havlin, 1995)

$$\text{MSD}(n) = \langle \vec{r}^2(n) \rangle = \left\langle \left( \sum_{i=1}^n \vec{e}_i \right)^2 \right\rangle = n + 2 \sum_{i < j} \langle \vec{e}_i \cdot \vec{e}_j \rangle = n. \quad (\text{Eq. 4})$$

Remarkably, the MSD of normal random walks grows linearly with the number of time steps  $n$ . The MSD is proportional to the circular area on a two-dimension grid that is covered by the particles' trajectories. For illustration, three exemplary computer-simulated random walks on a two-dimensional Cartesian grid with a total number of  $N = 500$  time steps that start at the origin  $x = y = 0$  are depicted in Figure 1a. The corresponding squared displacements of the random walks' trajectories are shown in Figure 1b. Additionally, the ensemble average of one thousand random walks' squared displacements is illustrated as black curve in Figure 1b. As theoretically calculated in Eq. 4, the average MSD of the random walks grows linearly as function of the number of time steps  $n$ . Isotropic diffusion in homogeneous environments can be understood as the continuous limit of these computer simulated random walks.

To simulate the hindrance due to collisions with immobile obstacles, lattice vertices were randomly blocked by these obstacles (Saxton, 1994). The effect of binding on the diffusion

process was studied by Monte Carlo simulations for different binding energy distributions and for long-tailed waiting time distributions (Saxton, 1996).

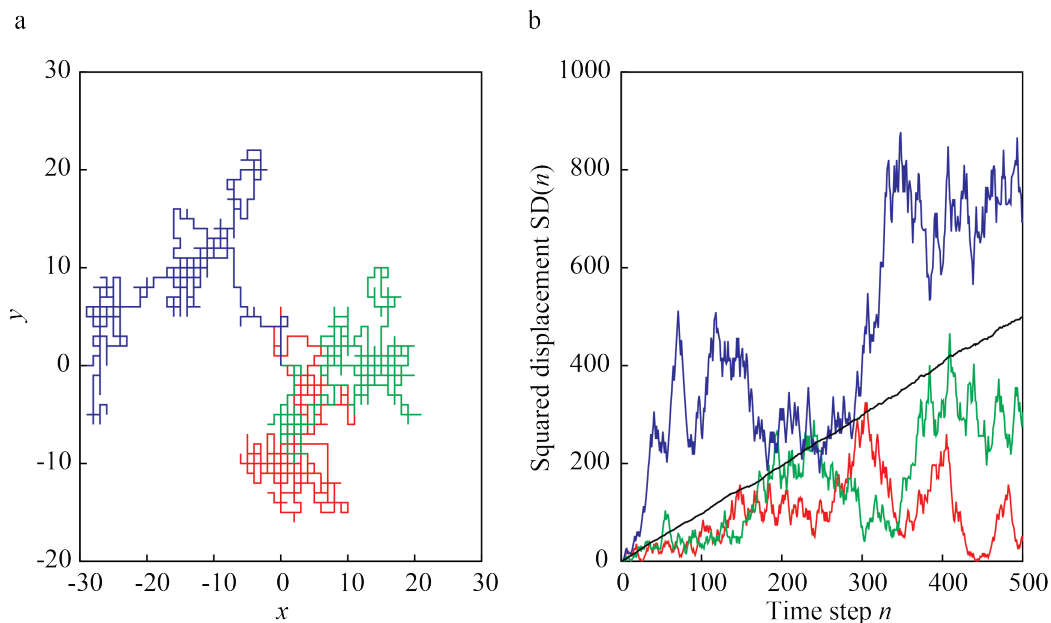


**Figure 1:** (a) Three simulated random walks on a Cartesian grid with a total number of  $N = 500$  time steps. (b) The corresponding squared displacements of the random walks in panel a. By averaging over one thousand squared displacement curves, the MSD of the ensemble grows linearly with time (black line). The random walks were simulated with MATLAB.

### II.1.1.2 The master equation

Another approach to describe diffusion theoretically is based on the master equation that gives the time evolution of a particle's probability to occupy a vertex of the Cartesian grid (van Kampen, 1992). A sketch of a one-dimensional grid with all relevant variables for the formulation of the master equation is given in Figure 2.

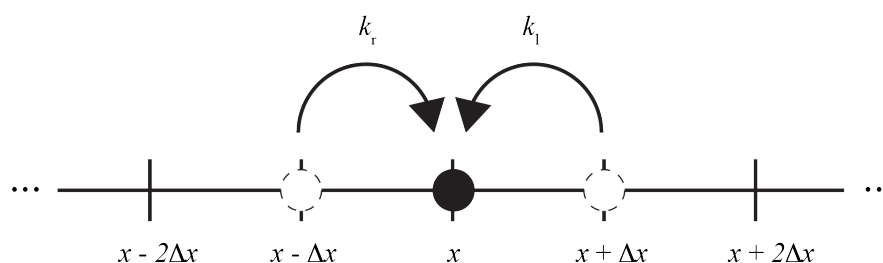


**Figure 2:** Random walk on a one-dimensional grid with a vertex distance  $\Delta x$ . The rate constants for particles to jump to the neighboring vertex on the right and left side are  $k_r$  and  $k_l$ , respectively.

The temporal change of the probability  $P(x,t)$  that a particle occupies the grid vertex at position  $x$  and time  $t$  is given by

$$\frac{\partial}{\partial t} P(x,t) = \underbrace{k_l P(x+\Delta x,t) + k_r P(x-\Delta x,t)}_{\text{Gain}} - \underbrace{k_l P(x,t) + k_r P(x,t)}_{\text{Loss}}. \quad (\text{Eq. 5})$$

Particles have two possibilities to reach the grid vertex  $x$  within a time step  $\Delta t$ : Either from the vertex on the left or from the vertex on the right side. Furthermore, particles can move from a vertex  $x$  to the neighboring vertex on their left or on their right side. Expanding the probability  $P(x,t)$  around the position  $x$  into a Taylor series results in

$$P(x \pm \Delta x, t) = P(x, t) \pm \Delta x \frac{\partial}{\partial x} P(x, t) + \frac{\Delta x^2}{2} \frac{\partial^2}{\partial x^2} P(x, t) + O(\Delta x^3). \quad (\text{Eq. 6})$$

By inserting Eq. 6 into Eq. 5 one obtains the Fokker-Planck equation (Fokker, 1914; Planck, 1917), which is a second order partial differential equation:

$$\frac{\partial}{\partial t} P(x, t) = (k_l - k_r) \Delta x \frac{\partial}{\partial x} P(x, t) + (k_l + k_r) \frac{\Delta x^2}{2} \frac{\partial^2}{\partial x^2} P(x, t). \quad (\text{Eq. 7})$$

In Eq. 7, the term of order  $\Delta x$  is the drift term that vanishes for symmetric transport processes, i.e.  $k_r = k_l$ . Furthermore, the term of order  $\Delta x^2$  describes diffusion processes with a diffusion coefficient

$$D = (k_l + k_r) \frac{\Delta x^2}{2}. \quad (\text{Eq. 8})$$

If the jump rates to the left and right vertex are  $k_r = k_l = 0.5$ , then Eq. 7 is equivalent to the diffusion equation. Normal isotropic diffusion in only one dimension is described by Eq. 9, but it can be easily generalized for higher dimensionality:

$$\frac{\partial}{\partial t} P(x, t) = D \frac{\partial^2}{\partial x^2} P(x, t). \quad (\text{Eq. 9})$$

### II.1.1.3 Fick's laws of diffusion

An empirical approach to diffusion was introduced by Adolf Fick in 1855 (Fick, 1855) who used continuous concentration scalar fields. Fick's first law postulates that gradients in the particle concentration  $c(\vec{r}, t)$  generate particle flux  $\vec{J}(\vec{r}, t)$  from positions of high concentration to positions of low concentration:

$$\vec{J}(\vec{r}, t) = -D\vec{\nabla}c(\vec{r}, t). \quad (\text{Eq. 10})$$

In Eq. 10,  $D$  is the diffusion coefficient (or tensor for anisotropic diffusion) and  $\vec{\nabla}$  is the vector differential operator or Nabla operator. According to Fick's first law, particle concentration heterogeneities are equilibrated by diffusive flux. The temporal evolution of the concentration field is described by Fick's second law, which can be derived by using the mass continuity equation

$$\frac{\partial}{\partial t}c(\vec{r}, t) = -\text{div } \vec{J}(\vec{r}, t). \quad (\text{Eq. 11})$$

It states that if the concentration in an infinitesimal volume  $dV$  around position  $\vec{r}$  changes, there is a particle flux  $\vec{J}$  through the volume's surface. By inserting Eq. 10 into Eq. 11, Fick's second law is obtained:

$$\frac{\partial}{\partial t}c(\vec{r}, t) = \vec{\nabla} \cdot [D\vec{\nabla} c(\vec{r}, t)]. \quad (\text{Eq. 12})$$

For isotropic diffusion,  $D$  is a constant and Eq. 12 simplifies to the diffusion equation:

$$\frac{\partial}{\partial t}c(\vec{r}, t) = D\Delta c(\vec{r}, t). \quad (\text{Eq. 13})$$

In Eq. 13,  $\Delta$  represents the Laplace operator

$$\Delta = \vec{\nabla}^2 = \vec{\nabla} \cdot \vec{\nabla} = \frac{\partial^2}{\partial x^2} + \frac{\partial^2}{\partial y^2} + \frac{\partial^2}{\partial z^2}. \quad (\text{Eq. 14})$$

The solution of Eq. 13 in  $d$  dimensions for the initial condition that  $N_0$  particles are localized at position  $\vec{r}'$  at time  $t = 0$ , i.e.  $c(\vec{r}, t = 0) = N_0 \delta(\vec{r} - \vec{r}')$ , is given by

$$c(\vec{r}, \Delta t) = \frac{N_0}{(4\pi D \Delta t)^{d/2}} \exp\left(-\frac{(\vec{r} - \vec{r}')^2}{4D \Delta t}\right). \quad (\text{Eq. 15})$$

The probability density  $p_{\text{diff}}$  for a particle to be after a time lag  $\Delta t = 0$  at position  $\vec{r}'$  and after a time lag  $\Delta t = t$  at position  $\vec{r}$  can be calculated by normalizing Eq. 15 with the initial particle number  $N_0$ . The result is the so-called diffusion propagator, which is in three dimensions given by

$$p_{\text{diff}}(\vec{r}, \vec{r}', t) = \frac{1}{(4\pi D t)^{3/2}} \exp\left(-\frac{(x - x')^2 + (y - y')^2 + (z - z')^2}{4D t}\right). \quad (\text{Eq. 16})$$

It describes the diffusive spreading of particles that are released at position  $\vec{r}'$  into space after time  $t$  by a three-dimensional Gaussian function with  $1/e$  half widths  $\sqrt{4Dt}$ . An exemplary one-dimensional probability density function is depicted in Figure 3 for a diffusion coefficient  $D = 30 \mu\text{m}^2\text{s}^{-1}$  and different time lags.

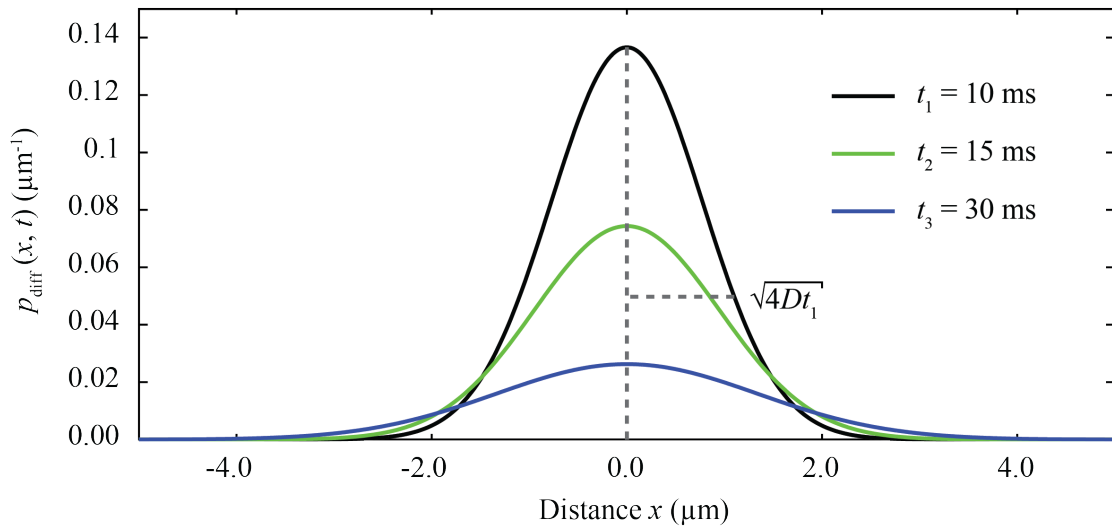


**Figure 3:** One-dimensional probability density function  $p_{\text{diff}}(x, t)$  for spreading of particles in space due to diffusion with a diffusion coefficient  $D = 30 \mu\text{m}^2\text{s}^{-1}$  after  $t_1 = 10$  ms,  $t_2 = 15$  ms and  $t_3 = 30$  ms.

The MSD of particles as a function of time can be calculated as the second moment of the particles' probability density distribution

$$\text{MSD}(t) = \int_{-\infty}^{+\infty} \bar{r}^2 p_{\text{diff}}(\bar{r}, t) d^3 r. \quad (\text{Eq. 17})$$

It can be shown that diffusing particles' MSD grows linearly with time  $t$  and that the proportionality constant is the diffusion coefficient  $D$ :

$$\text{MSD}(t) = 2dDt. \quad (\text{Eq. 18})$$

The variable  $d$  in Eq. 18 represents the dimensionality of the diffusion process. One-dimensional is for example the diffusion of proteins like transcription factors due to unspecific binding and sliding along DNA fibers until a specific binding site is reached. Two-dimensional is the diffusive movement of proteins or lipids in cellular membranes, and three-dimensional is diffusion of signaling molecules in the cellular fluid.

The Stokes-Einstein equation (Einstein, 1905) gives a relation between the diffusion coefficient of spherical particles of radius  $r$  in fluids of viscosity  $\eta$  at low Reynolds numbers and at the absolute temperature  $T$ :

$$D = \frac{k_B T}{6\pi\eta r}. \quad (\text{Eq. 19})$$

### II.1.2 Anomalous diffusion

The interior of living cells is crowded due to high concentrations of macromolecules and cellular organelles. Furthermore, interacting molecules can bind to sites on cellular structures with broad affinity distributions. In this complex and disordered environment, diffusion of molecules is hindered and their MSD cannot be described by linearly growing functions (Hofling and Franosch, 2013; Schwille et al., 1999b; Wachsmuth et al., 2000). In this thesis diffusion of particles with a non-linear MSD will be in general called anomalous diffusion – independent of the origin of the anomaly and the actual time dependence. Anomalous diffusion was found in simulations including collisions with immobile

obstacles (Saxton, 1994) and binding reactions (Saxton, 1996). In the literature, anomalous diffusion processes with MSDs growing faster than linearly with time are called superdiffusive. Here, only diffusion processes with less than linearly growing MSD that are called subdiffusive were studied. For the description of anomalous diffusion by random walks, different steps are not independent, i.e. the correlation term in Eq. 4 does not vanish for  $i \neq j$ . An anisotropy in the step direction probability may occur due to collisions with impermeable and immobile obstacles: After the collision with an obstacle, a backward step is more probable than a forward step into the occupied space. Other disturbing factors of random walks' isotropy are for example drift processes like flow or directed motion due to active transport and interactions with the surrounding structure because of attractive and repulsive electrostatic forces or binding reactions. The cross-correlation term in Eq. 4 vanishes for random walk steps that are far apart in time ( $i \ll j$ ), so that the diffusion process finally becomes normal again on large time and length scales.

Percolation clusters with a fractal geometry that is self-similar on all length scales are commonly used to describe the spatial distribution of obstacles in living cells. The fractal geometry is characterized by a single parameter, which is the fractal dimension  $d_f$  that gives the mass  $m$  enclosed in a sphere of radius  $r$  (Bunde and Havlin, 1995)

$$m(r) \sim r^{d_f}. \quad (\text{Eq. 20})$$

In a three-dimensional rigid body, the fractal dimension  $d_f$  is an integer. However, the fractal dimension of fractal structures is reduced and non-integer. The trajectories of particles' random walks in fractal structures are also described as fractal structures of fractal dimension  $d_w$ .

The MSD of a random walk in  $d$  dimensions is related to its fractal dimension  $d_w$  by a power law:

$$\text{MSD}(t) = 2dD_{\text{app}}(t)t = 2d\Gamma t^{d_w/2} = 2d\Gamma t^\alpha, \quad (\text{Eq. 21})$$

with the transport coefficient  $\Gamma$ , the anomaly parameter  $\alpha = d_w/2$  and the time-dependent apparent diffusion coefficient



$$D_{\text{app}}(t) = \Gamma t^{\alpha-1}. \quad (\text{Eq. 22})$$

If the fractal dimension of random walks is  $d_w = 2$ , Eq. 21 gives the MSD of normally diffusing particles that is proportional to time. For fractal dimensions  $d_w < 2$ , the MSD grows less than linearly with time (Figure 4 a).

The corresponding random walks are more compact than for normal diffusion. Therefore, the probability to return to an already visited position is increased. If the obstacle concentration is higher than a critical value, the so-called percolation threshold, the accessible open space is not connected over long distances anymore. Only for obstacle concentrations near the percolation threshold, analytical and numerical relations between the fractal dimension  $d_w$  of random walks in a static structure of fractal dimension  $d_f$  were derived (Havlin et al., 1984). Moreover, random walks can have fractal dimensions of  $d_w > 2$ , if active transport accelerates the diffusion process (superdiffusion).

To describe subdiffusion, continuous time random walks (CTRWs) can be used to include waiting times between consecutive steps of the walk (Condamin et al., 2008). Long-tailed waiting time distributions of CTRWs can mimic transient immobilization of particles due to binding reactions or trapping in dead ends of the cellular structure.

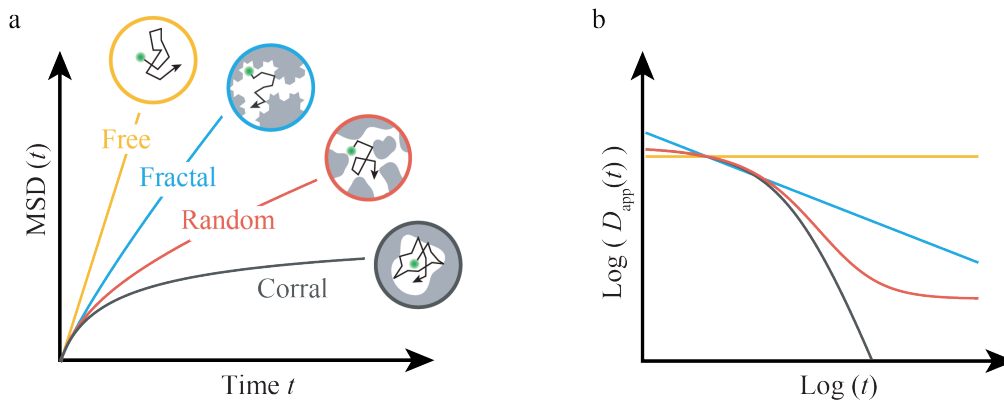


**Figure 4: (a)** Characteristic MSD plots for free diffusion, hindered diffusion in fractal percolation clusters or media with random barriers, and confined diffusion in corraling structures. **(b)** The corresponding apparent diffusion coefficients are plotted as a function of time in a double-logarithmic representation. In this representation, the difference between the diffusion laws in fractal and random structures is more pronounced.

More complicated time dependencies of the MSD (Figure 4a) than a simple power for diffusion in a fractal percolation cluster were found for diffusion in media of randomly

distributed barriers (Novikov et al., 2011) and in porous media with broad distributions of pore sizes (Loskutov and Sevriugin, 2013). Characteristic for these diffusive processes are normal diffusion regimes on the microscopic and macroscopic scale that are connected by a crossover regime.

### II.1.3 Confined diffusion

In disordered media with high obstacle concentrations, the accessible open space is not completely connected for diffusing molecules: There are corrals formed by impermeable barriers that prevent molecules from diffusing out of these regions. This diffusion behavior was observed by single particle tracking of nuclear bodies in the nucleus of living cells (Görisch et al., 2004). The confined diffusion of particles in corrals can be theoretically described by using three-dimensional harmonic potentials

$$U(\vec{r}) = \frac{k}{2}(\vec{r} - \vec{r}_c)^2, \quad (\text{Eq. 23})$$

which generate restoring forces that keep the particles near the center of the corral  $\vec{r}_c$  and mimic the corral boundaries:

$$\vec{F}(\vec{r}) = -\vec{\nabla}U(\vec{r}) = -k(\vec{r} - \vec{r}_c). \quad (\text{Eq. 24})$$

These forces generate an additional particle flux

$$\vec{J}(\vec{r}, t) = -\frac{c(\vec{r}, t)}{\gamma} \vec{\nabla}U(\vec{r}). \quad (\text{Eq. 25})$$

The additional particle flux in media with friction coefficient  $\gamma$  has to be considered in the diffusion equation (Eq. 13). The modified diffusion equation is given by

$$\begin{aligned} \frac{\partial}{\partial t} c(\vec{r}, t) &= D\Delta c(\vec{r}, t) + \frac{1}{\gamma} \vec{\nabla} \left[ \vec{\nabla}U(\vec{r}) c(\vec{r}, t) \right] \\ &= D\Delta c(\vec{r}, t) + \frac{k}{\gamma} \vec{\nabla} \left[ (\vec{r} - \vec{r}_c) c(\vec{r}, t) \right]. \end{aligned} \quad (\text{Eq. 26})$$

The solution of this partial differential equation for the boundary condition that a particle is at time  $t = 0$  at position  $\vec{r}'$  describes the so-called Ornstein-Uhlenbeck process and is given by the transition probability density  $p_{\text{conf}}$  (van Kampen, 1992)

$$p_{\text{conf}}(\vec{r}, \vec{r}', t) = \left( \frac{k}{2\pi D\gamma [1 - \exp(-2k\gamma^{-1}t)]} \right)^{3/2} \exp \left( - \frac{k \left( (\vec{r} - \vec{r}_c) - (\vec{r}' - \vec{r}_c) \exp(-k\gamma^{-1}t) \right)^2}{2D\gamma [1 - \exp(-2k\gamma^{-1}t)]} \right). \quad (\text{Eq. 27})$$

Eq. 27 converges to the transition probability density  $p_{\text{diff}}$  of free diffusion (Eq. 16) for a vanishing potential, i.e. for  $k\gamma^{-1} \rightarrow 0$ .

## II.2 Confocal fluorescence microscopy

### II.2.1 Fluorescence

The phenomenon of fluorescence is the observation that certain matter emits light after illumination with mostly shorter wavelength light. This can be explained on a molecular level since atoms and molecules have different quantum states of distinct energy values. Transitions between different energy states are correlated to absorption or emission of photons. These transitions can be illustrated in so-called Jablonski energy diagrams as shown in Figure 5. Fluorescent dyes can be excited from the ground state  $S_0$  to a higher energy state  $S_1$  by absorption of photons that correspond to light of frequency  $\nu_A$  and energy  $h\nu_A$  ( $h$  is the Planck constant) if the photons' energy matches the energy difference between these states (Lakowicz, 2006). After non-radiative relaxation to a lower energy level of  $S_1$  by disposing energy for vibration and rotation of the dye molecule, a fluorescence photon of lower energy  $h\nu_F$  is emitted. The difference between the frequency of the absorption and fluorescence photon  $\Delta\nu = \nu_A - \nu_F$  is called Stokes shift. A typical lifetime of several nanoseconds is observed for the first excited singlet state  $S_1$ . If a second photon is absorbed during this time period, the fluorescent dye is excited to even higher energy levels, which may result in covalent interactions that change the molecular structure and may finally lead to irreversible photobleaching of the fluorophore. Furthermore, dye molecules can undergo an electron spin conversion to the first triplet state  $T_1$ . This process is called intersystem crossing. The  $T_1$  state has a lifetime of milliseconds to several

seconds because the crossover to the singlet ground state via emission of a phosphorescence photon of energy  $h\nu_p$  is extremely unlikely according to quantum mechanics. From the triplet state  $T_1$ , the dye molecule can undergo a second intersystem crossing back to the first excited singlet state  $S_1$  and emit a fluorescence photon. This process can lead to blinking of the fluorescent molecule on different time scales, depending on the lifetimes of the involved quantum states. The discovery of fluorescent proteins allows for non-invasive labeling of molecules like DNA or proteins with fluorophores in living cells, which is the basis of fluorescence confocal microscopy.

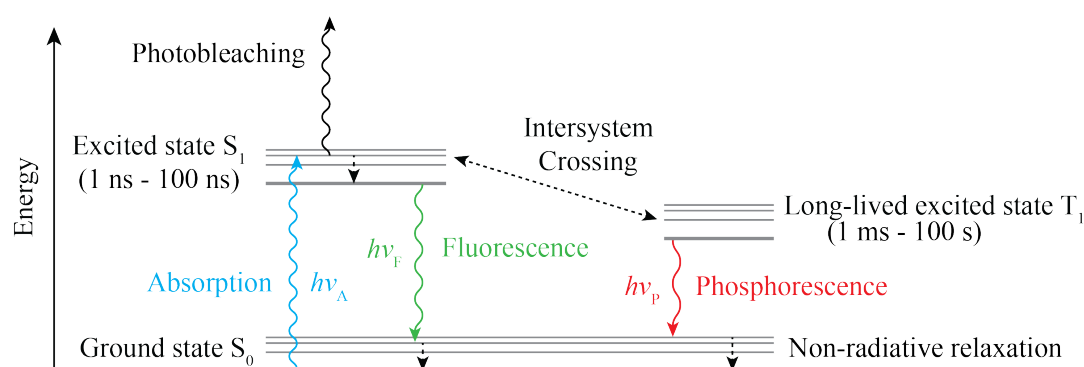


**Figure 5:** Jablonski energy diagram for absorption, fluorescence, photobleaching and phosphorescence. Different quantum states (grey lines) of a fluorescent molecule are depicted. By absorbing a photon (blue), the fluorophore can be excited from the ground state  $S_0$  to a higher energy level. From there, it can relax to lower energy levels of  $S_1$  by converting energy into molecular vibrations or rotations (black dashed arrows) and finally emit a fluorescence photon (green). Additionally, it can either absorb a second photon in the excited state, which may result in irreversible photobleaching (black). Another possible transition is the crossover to a long-lived triplet state  $T_1$  from which it can relax to the ground state by emitting a phosphorescence photon of longer wavelength (red).

## II.2.2 Confocal laser scanning microscopy

For imaging the microscopic processes of life in living cells with high spatial resolution, labeling of cellular components like DNA or proteins with fluorescent dyes is used in combination with confocal laser scanning microscopes (CLSM). CLSMs are optimized for detection of fluorescence light. In commercially available CLSM systems, collimated laser beams are focused into the sample by an objective lens with high numerical aperture (NA) to excite fluorescently labeled molecules in a small diffraction-limited volume (Pawley, 2006). Acousto-optical devices are used to separately modulate the intensities of spectrally different illumination laser beams. The emitted fluorescence light is collected from the

detection volumes in the sample by the same objective lens that was used for illumination. Subsequently, the light is detected by photomultiplier tubes (PMT) or photodiodes through a pinhole that allows for optical sectioning and an enhanced spatial resolution. Fluorescence light that is not emitted near the focus point is blocked by the pinhole in conjugate or confocal position to the focus point. The principal of confocal microscopy is illustrated in Figure 6.

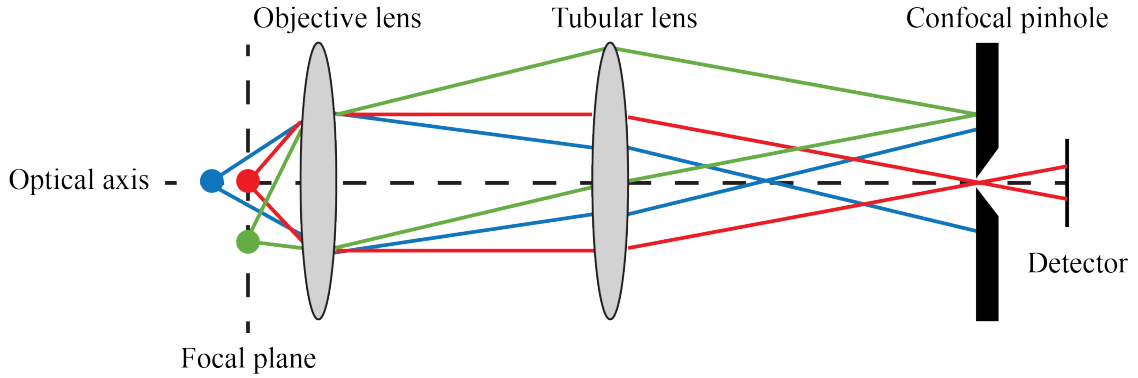


**Figure 6:** The principal of contrast and resolution enhancement in confocal microscopy. Fluorescence light is collected by an objective lens from the sample and focused on a pinhole in confocal position. Fluorescence light emitted near the focus can pass unaffectedly through the confocal pinhole (red rays). Only a small fraction of fluorescence photons emitted near the optical axis but farther above or below the focal plane (blue rays) can pass through the pinhole to the detector. Fluorescence light emitted farther apart from the focus but in the focal plane (green rays) is mostly blocked by the confocal pinhole.

The optical resolution of conventional widefield (WF) microscopes, defined as the full width at half maximum (FWHM) of the microscope's point spread function, is given by (Wilhelm et al., 2003)

$$\text{FWHM}_{\text{lateral,WF}} = \frac{0.51\lambda_{\text{det}}}{NA} \quad (\text{Eq. 28})$$

in lateral direction and

$$\text{FWHM}_{\text{axial,WF}} = \frac{n\lambda_{\text{det}}}{NA^2} \quad (\text{Eq. 29})$$

in direction of the optical axis. In Eq. 28 and 29, the wavelength of the detected light is denoted by  $\lambda_{\text{det}}$ , the numerical aperture of the objective lens is  $NA$  and the refractive

index of the immersion medium is  $n$ . For a water objective with  $NA=1.2$ , the refractive index of water  $n=1.33$  and a fluorescence wavelength of  $\lambda_{\text{det}}=525$  nm, a lateral resolution of  $\text{FWHM}_{\text{lateral, WF}}=220$  nm and an axial resolution of  $\text{FWHM}_{\text{axial, WF}}=485$  nm was calculated.

For CLSMs with small pinholes, the resolution can be calculated as (Wilhelm et al., 2003)

$$\text{FWHM}_{\text{lateral, CLSM}} = \frac{0.37 \bar{\lambda}}{NA} \quad (\text{Eq. 30})$$

for the lateral direction and

$$\text{FWHM}_{\text{axial, CLSM}} = \frac{0.64 \bar{\lambda}}{\left(n - \sqrt{n^2 - NA^2}\right)} \quad (\text{Eq. 31})$$

for the axial direction. Because of the difference between illumination and detection wavelength, a mean wavelength defined by Eq. 32 is used

$$\bar{\lambda} \approx \sqrt{2} \frac{\lambda_{\text{det}} \lambda_{\text{ill}}}{\sqrt{\lambda_{\text{det}}^2 + \lambda_{\text{ill}}^2}}. \quad (\text{Eq. 32})$$

Accordingly, the improved resolution of CLSMs due to illumination of a single point with laser light of wavelength  $\lambda_{\text{ill}}=488$  nm and enhanced contrast due to a confocal pinhole was caculated as  $\text{FWHM}_{\text{lateral, CLSM}}=160$  nm and  $\text{FWHM}_{\text{axial, CLSM}}=430$  nm.

For three-dimensional imaging of living cells, mirror galvanometers are used to sequentially scan a plane in the sample point by point in lateral direction, and a galvanometer driven stage is used to position the focus in axial direction. Finally, a three-dimensional image stack can be reconstructed with a computer.

### II.2.3 Molecule detection efficiency of confocal microscopes

The imaging properties of fluorescence CLSMs are described by their molecule detection efficiency (MDE), which is the diffraction limited three-dimensional image of an infinitesimally small fluorescent point light source acquired by the optical system. It has to be determined for quantitative analysis of fluorescence fluctuation microscopy (FFM)

measurements and for increasing the contrast and resolution of fluorescence images by deconvolution algorithms. For CLSMs, the MDE  $\Psi$  is given by the product of their illumination point spread function (PSF) and detection PSF (Stelzer and Lindek, 1994):

$$\Psi(\vec{r}) = \text{PSF}_{\text{ill}}(\vec{r}) \cdot \text{PSF}_{\text{det}}(\vec{r}). \quad (\text{Eq. 33})$$

The illumination and detection PSF can be calculated near the focus according to the Debye diffraction theory (Born, 1999; Hecht, 1989). An empirical model function for the detection probability that accounts for the double cone shaped beam profile in axial direction was proposed by Dertinger et al. (Dertinger et al., 2007).

### II.2.3.1 MDE near the focus described by Debye diffraction theory

According to Debye diffraction theory, the illumination amplitude  $h_{\text{ill}}$  of the electromagnetic field near the focus point can be described as superposition of plane waves integrated over the aperture of a circular lens. The illumination PSF is given by the absolute square of the illumination amplitude  $h_{\text{ill}}$ :

$$\text{PSF}_{\text{ill}} = |h_{\text{ill}}(\vec{r})|^2 = \left( \frac{\sin u_{\text{ill}}}{u_{\text{ill}}} \right)^2 \left( \frac{2J_1(v_{\text{ill}})}{v_{\text{ill}}} \right)^2 \text{ with} \quad (\text{Eq. 34})$$

$$u_{\text{ill}} = n \frac{2\pi}{\lambda_{\text{ill}}} z \sin^2(\alpha/2) \text{ and } v_{\text{ill}} = n \frac{2\pi}{\lambda_{\text{ill}}} \sqrt{x^2 + y^2} \sin \alpha. \quad (\text{Eq. 35})$$

Here,  $J_1$  is the Bessel function of the first kind and order. Furthermore,  $\lambda_{\text{ill}}$  is the wavelength of illumination light,  $n$  is the refractive index of the optical medium and  $\alpha$  the half-angle of the maximum cone of light that is collected from the lens. The NA of the objective lens is defined by:

$$\text{NA} = n \sin \alpha. \quad (\text{Eq. 36})$$

The detection PSF for high NA objective lenses can be approximated by Debye diffraction theory. According to that the detection PSF can be described by

$$\text{PSF}_{\text{det}} = |h_{\text{det}}(\vec{r})|^2 = \left( \frac{\sin u_{\text{det}}}{u_{\text{det}}} \right)^2 \left( \frac{2J_1(v_{\text{det}})}{v_{\text{det}}} \right)^2 \text{ with} \quad (\text{Eq. 37})$$

$$u_{\text{det}} = n \frac{2\pi}{\lambda_{\text{det}}} z \sin^2(\alpha/2) \text{ and } v_{\text{det}} = n \frac{2\pi}{\lambda_{\text{det}}} \sqrt{x^2 + y^2} \sin \alpha. \quad (\text{Eq. 38})$$

The wavelength of the emitted fluorescence light is represented in Eq. 38 by  $\lambda_{\text{det}}$ . The resulting molecule detection efficiency (MDE) function is illustrated in Figure 7.

A central maximum (Airy disk) and first order diffraction ring (Airy ring) of the lateral MDE can be observed in logarithmic representation. In lateral direction, the diffraction pattern is that of a circular aperture and in axial direction that of a slit diaphragm (Guenther, 1990; Sheppard and Matthews, 1987).

By neglecting the low amplitude Airy rings, the MDE of CLSMs with high numerical apertures is often approximated by a three-dimensional Gaussian function with beam waists given by the  $1/e^2$  radii  $w_0$  and  $z_0$  in lateral and axial direction, respectively (Qian and Elson, 1991):

$$\Psi(\vec{r}) = \exp\left(-2\frac{x^2 + y^2}{w_0^2} - 2\frac{z^2}{z_0^2}\right). \quad (\text{Eq. 39})$$

This approximation of the MDE is only valid near the focal plane.

### II.2.3.2 Empirical model for the double cone shape of the MDE

An empirical model for confocal fluorescence microscope's MDE that describes the double cone shape of focused and diverging light beams was introduced and validated with experimental data by Dertinger et al. (Dertinger et al., 2007). However, diffraction patterns are completely neglected in this model. The double cone MDE function  $\Psi$  is given by:

$$\Psi(\vec{r}) = \frac{\kappa(z)}{w^2(z)} \exp\left(-2\frac{x^2 + y^2}{w^2(z)}\right). \quad (\text{Eq. 40})$$

Each plane along the optical axis  $z$  is approximated by a two-dimensional Gaussian function with  $1/e^2$  radius  $w(z)$ .



The lateral beam waist as a function of the axial position  $z$  is described by

$$w(z) = w_0 \sqrt{1 + \left( \frac{\lambda_{\text{ill}} z}{\pi w_0^2 n} \right)^2}. \quad (\text{Eq. 41})$$

Here,  $w_0$  gives the beam waist in the focal plane,  $\lambda_{\text{ill}}$  is the wavelength of the illumination light and  $n$  the refractive index of the corresponding immersion medium.

The function  $\kappa(z)$  accounts for blocking of fluorescence light that is emitted in out-of-focus regions by a pinhole with an aperture radius projected into the focal plane of  $a$ :

$$\kappa(z) = 2 \int_0^a \frac{\rho d\rho}{R^2(z)} \exp\left(-2 \frac{\rho^2}{R^2(z)}\right) = 1 - \exp\left(-2 \frac{a^2}{R^2(z)}\right). \quad (\text{Eq. 42})$$

In Eq. 42, the function  $R(z)$  is defined similarly to Eq. 41:

$$R(z) = R_0 \sqrt{1 + \left( \frac{\lambda_{\text{det}} z}{\pi R_0^2 n} \right)^2}. \quad (\text{Eq. 43})$$

The parameter  $\lambda_{\text{det}}$  in Eq. 43 is the wavelength of the emitted fluorescence light and  $R_0$  is a (generally unknown) model parameter that is determined experimentally.

This double cone shaped model of the MDE is depicted in Figure 7. Notably, it is consistent with the three-dimensional Gaussian model approximation of the MDE in the focal plane but diverges farther apart from the focus. The double cone MDE model function reflects more realistically the experimental situation since it describes the double cone shaped profile of focused light beams, as previously measured by Dertinger et al. (Dertinger et al., 2007). A comparison of the MDE model function derived by Debye theory that is only valid near the focal plane and the double cone MDE model is shown in Figure 7.

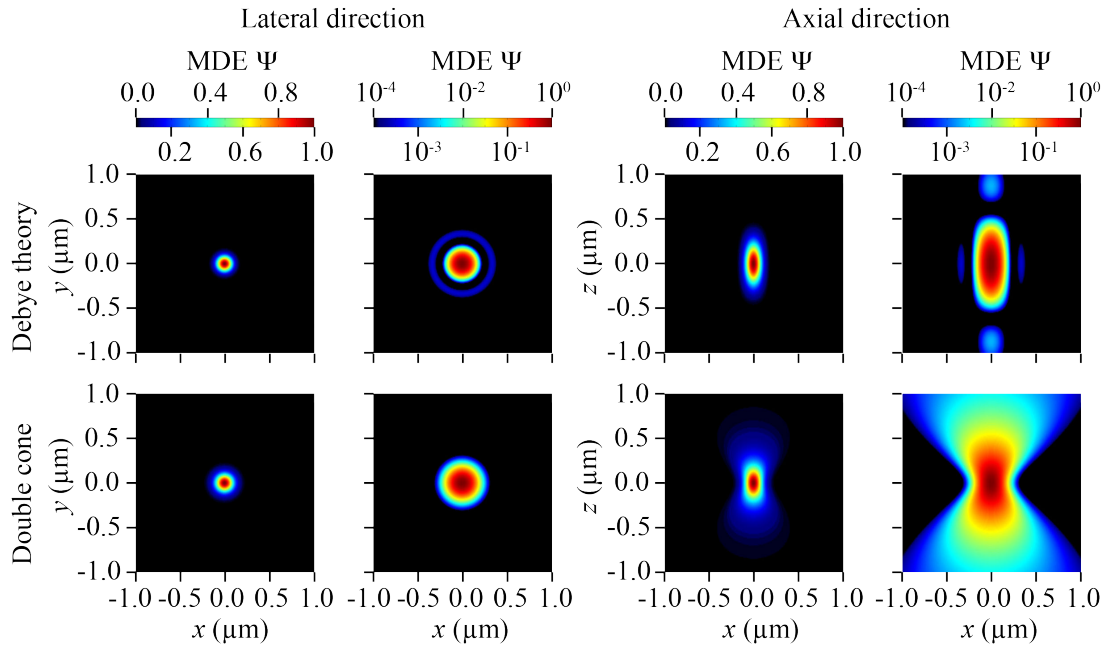


**Figure 7:** Model functions for the molecule detection efficiency (MDE) derived by Debye diffraction theory (only valid near the focus plane) and by empirically modeling the double cone shaped profile of a focused light beam in lateral and axial direction. The functions are plotted for an illumination wavelength  $\lambda_{\text{ill}} = 488$  nm, a detection wavelength of  $\lambda_{\text{det}} = 525$  nm, the refractive index of water as immersion medium  $n = 1.33$ , a half angle of the focused light cone  $\alpha = 68^\circ$  and the double cone model parameters  $w_0 = 150$  nm,  $R_0 = 130$  nm as well as the radius of the confocal pinhole projected into the focal plane  $a = 250$  nm. All functions were shown in linear (left) and logarithmic (right) representation

### II.3 Fluorescence fluctuation microscopy techniques

The mobility and interactions of fluorescently labeled molecules can be non-invasively measured in living cells by fluorescence fluctuation microscopy techniques. One approach is to acquire the fluctuating fluorescence signals of diffusing molecules emitted in diffraction-limited illumination volumes followed by a correlation analysis (Elson and Magde, 1974; Magde et al., 1972; Magde et al., 1974). This approach is called fluorescence correlation spectroscopy (FCS). Different modifications of FCS were developed over recent years, e.g. fluorescence cross-correlation spectroscopy of signals from different spectral detection channels (dual-color FCCS) (Rarbach et al., 2001; Schwille et al., 1997; Weidemann et al., 2002) or fluorescence cross-correlation spectroscopy of signals from spatially separated detection volumes in the sample (dual-focus FCCS) (Brinkmeier et al., 1999; Dertinger et al., 2007). A complementary approach is bleaching of fluorescent molecules in a region of interest and acquiring the recovering

fluorescence signals due to exchange of bleached and unbleached molecules by diffusion (Axelrod et al., 1976; Reits and Neefjes, 2001). This methodology is called fluorescence recovery after photobleaching (FRAP).

### II.3.1 Fluorescence recovery after photobleaching

Mobility, kinetic binding parameters and fractions of immobilized fluorescent molecules arising from trapping or strong binding can be measured in living cells by bleaching the fluorophores in a region of interest (ROI) with high laser illumination directly followed by imaging the equilibration or recovery of the fluorescence intensity over time (Figure 8). Bleaching and imaging is generally done with confocal laser scanning microscopes (CLSM) so that the ROI cannot be bleached instantaneously, as assumed for most theoretical FRAP models. Rather, the ROI is bleached sequentially point by point in a raster scan process. Fluorescent and bleached molecules redistribute during the bleach phase and before the acquisition of the first post-bleach image frame. Furthermore, a quantitative description of the evolution of fluorescence profiles during the scan process is pixel-wise photobleaching profile evolution analysis (3PEA) developed by Erdel and Rippe (Erdel and Rippe, 2012).

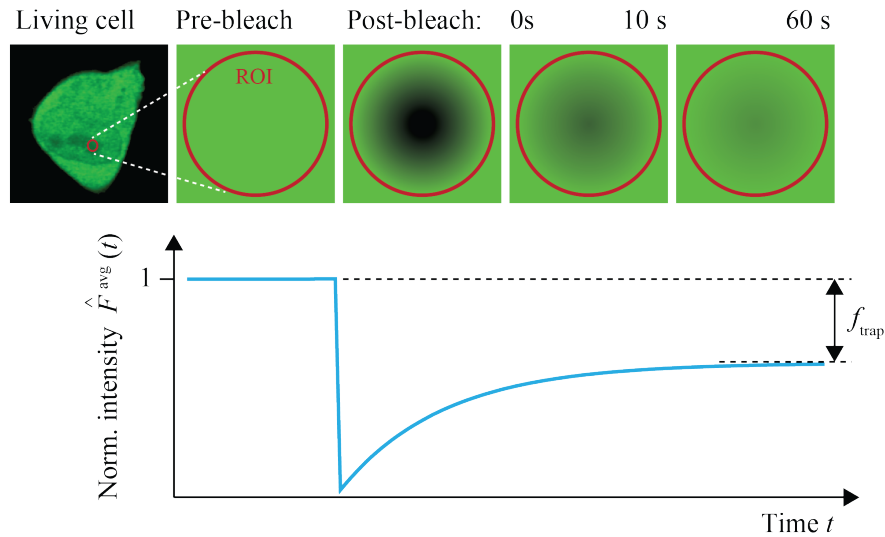


**Figure 8:** Principle of fluorescence recovery after photobleaching experiments. Fluorescent molecules are bleached in a region of interest (ROI), here a circular area, followed by recording of the fluorescence recovery as a function of time. From the recovery time, the mobility of fluorescent molecules can be determined. Furthermore, incomplete recovery of the fluorescence intensity  $F^{\text{avg}}(t)$  shows a fraction  $f_{\text{trap}}$  of molecules that is immobilized by trapping for longer period of times (Braga et al., 2004).

Here, a simple diffusion FRAP model function (Braga et al., 2004) was used that accounts for partial recovery of the fluorescence during the bleach process by both analyzing the radial profile of the first post-bleach image frame and the time evolution of the recovery. Notably, this model function can only be used for inert molecules since binding reaction are not included.

The temporal evolution of the fluorescence intensity distribution  $F(\vec{r}, t)$  due to diffusion of mobile fluorescently labeled molecules with diffusion coefficient  $D$  can be described by the diffusion equation

$$\frac{\partial}{\partial t} F(\vec{r}, t) = D \Delta F(\vec{r}, t). \quad (\text{Eq. 44})$$

According to Braga et al. (Braga et al., 2004), a good approximation of the three-dimensional bleach volume in the sample as observed in the first post-bleach frame ( $t = 0$ ) is given for mobile fluorescent molecules by

$$F_M(\vec{r}, t = 0) = F_0 \exp \left( -K_M \exp \left( -2 \frac{x^2 + y^2}{w_M^2} - 2 \frac{z^2}{z_M^2} \right) \right). \quad (\text{Eq. 45})$$

In Eq. 45,  $w_M$  and  $z_M$  are the profile width in lateral and axial direction, respectively. The bleach efficiency of the mobile fluorescent molecules is given by  $K_M$ .

The partial differential equation given by Eq. 44 was solved by (Blonk et al., 1993) using the approximation suggested by Eq. 45 as initial condition and the boundary condition for a much larger sample volume than the bleach volume

$$F_M(x = \infty, y = \infty, z = \infty, t) = F_0. \quad (\text{Eq. 46})$$

A solution of Eq. 44 is given by

$$F_M(\vec{r}, t) = F_0 z_M w_M^2 \sum_{n=0}^{\infty} \frac{(-K_M)^n \exp \left( \frac{-2nz^2}{z_M^2 + 8nDt} \right) \exp \left( \frac{-2n(x^2 + y^2)}{w_M^2 + 8nDt} \right)}{n! \sqrt{z_M^2 + 8nDt} (w_M^2 + 8nDt)}. \quad (\text{Eq. 47})$$

For analysis of the recovery curve of the fluorescence intensity  $F(t)$ , the fluorescence distribution that is theoretically described by Eq. 47 is averaged over a circular area of radius  $w_s$  to improve the signal to noise ration (Braeckmans et al., 2003; Klonis et al., 2002). The fluorescence intensity averaged over a circular area in the focal plane ( $z = 0$ ) can be calculated by

$$\hat{F}_M^{\text{avg}}(\vec{r}, t) = \frac{1}{\pi w_s^2 F_0} \int_{x^2 + y^2 \leq w_s^2} F_M(x, y, z = 0, t) dx dy. \quad (\text{Eq. 48})$$

Inserting of Eq. 47 into Eq. 48 finally yields

$$\hat{F}_M^{\text{avg}}(\vec{r}, t) = \frac{1}{2} \left[ \frac{w_M^2}{w_s^2} \left( \sum_{n=1}^{\infty} \frac{(-K_M)^n}{n! n} \frac{z_M}{\sqrt{z_M^2 + 8nDt}} \left( 1 - \exp\left( \frac{-2nw_s^2}{w_M^2 + 8nDt} \right) \right) \right) + 2 \right]. \quad (\text{Eq. 49})$$

A two-dimensional approximation of the system holds if the laser beam bleaches completely through the sample in axial direction ( $z_M \rightarrow \infty$ ):

$$\hat{F}_M^{2D}(\vec{r}, t) = \frac{1}{2} \left[ \frac{w_M^2}{w_s^2} \left( \sum_{n=1}^{\infty} \frac{(-K_M)^n}{n! n} \left[ 1 - \exp\left( \frac{-2nw_s^2}{w_M^2 + 8nDt} \right) \right] \right) + 2 \right]. \quad (\text{Eq. 50})$$

If a fraction  $f_{\text{trap}}$  of molecules is immobilized due to trapping, the normalized recovery of the fluorescence signal  $\hat{F}^{\text{avg}}(t)$ , averaged over a circular area, reads

$$\hat{F}^{\text{avg}}(t) = (1 - f_{\text{trap}}) \hat{F}_M^{\text{avg}}(t) + f_{\text{trap}} \hat{F}_{\text{IM}}^{\text{avg}}. \quad (\text{Eq. 51})$$

The normalized fluorescence of the immobile molecules is represented in Eq. 51 by  $\hat{F}_{\text{IM}}^{\text{avg}}$ . Since the radius  $w_M$  of the first post-bleach profile depends on the mobility of the fluorescent molecules, partial recovery of the fluorescence during the raster-scan process is roughly accounted for.

### II.3.2 Fluorescence correlation spectroscopy

Conventional laser-scanning confocal microscopes (CLSMs) with high detection sensitivity are ideal instruments for fluorescence correlation spectroscopy (FCS) measurements in living cells (Politz et al., 1998; Schwille et al., 1999a; Schwille et al., 1999b; Wachsmuth et al., 2000; Weiss et al., 2003). After acquisition of an overview image, the laser beam can be positioned to a location of interest from which fluorescence photons emitted by fluorescently labeled molecules in the illumination volume are detected. The acquired fluorescence intensity  $I(t)$  can be theoretically described by integration of the fluorophore distribution  $C(\vec{r}, t)$  over the observation volume defined by the MDE function  $\Psi(\vec{r})$  in the sample volume  $V$  (Lakowicz, 2006):

$$I(t) = B \int_V \Psi(\vec{r}) C(\vec{r}, t) d^3r. \quad (\text{Eq. 52})$$

In Eq. 52, the brightness  $B$  of the fluorophores depends on the quantum efficiency  $q$  for detection of fluorescence photons, the absorption cross-section  $\sigma$  and the quantum yield  $Q$  for emission of fluorescence photons:

$$B = q\sigma Q. \quad (\text{Eq. 53})$$

The distribution of  $N$  fluorophores at time  $t$  can be expressed by

$$C(\vec{r}, t) = \sum_{i=1}^N \delta(|\vec{r}_i(t) - \vec{r}|). \quad (\text{Eq. 54})$$

The mobility of molecules in living cells can be extracted from relative intensity fluctuations

$$\delta I(t) = I(t) - \langle I(t) \rangle \quad (\text{Eq. 55})$$

of the fluorescence signal  $I(t)$  due to diffusion of fluorescent molecules into and out of the diffraction-limited focus volume. In Eq. 55, the angular brackets  $\langle \dots \rangle$  denote the time

integral  $\int \dots dt$ . The probability for molecules to be still detected in the focus volume after a time lag  $\tau$  is proportional to the value of the so-called normalized autocorrelation (AC) function:

$$G(\tau) = \frac{\langle \delta I(t) \delta I(t + \tau) \rangle}{\langle I(t) \rangle^2} = \frac{\langle (I(t) - \langle I(t) \rangle)(I(t + \tau) - \langle I(t) \rangle) \rangle}{\langle I(t) \rangle^2} = \frac{\langle I(t) I(t + \tau) \rangle}{\langle I(t) \rangle^2} - 1. \quad (\text{Eq. 56})$$

Accordingly, the autocorrelation function for the fluorescence intensity fluctuations due to fluorophore concentration fluctuations in the observation volume reads

$$G(\tau) = \frac{B^2 \iint \Psi(\vec{r}_1) \langle \delta C(\vec{r}_1, t) \delta C(\vec{r}_2, t + \tau) \rangle \Psi(\vec{r}_2) d^3 r_1 d^3 r_2}{\left( B \bar{C} \int \Psi(\vec{r}) d^3 r \right)^2}. \quad (\text{Eq. 57})$$

Remarkably, the correlation function in Eq. 57 is independent of the fluorophores brightness. The concentration of molecules at time  $t$  and position  $\vec{r}_1$  is correlated with that at position  $\vec{r}_2$  and time  $t + \tau$  due to diffusion (Lakowicz, 2006):

$$\langle \delta C(\vec{r}_1, t) \delta C(\vec{r}_2, t + \tau) \rangle = \bar{C} (4\pi D \tau)^{-3/2} \exp\left(-\frac{(\vec{r}_1 - \vec{r}_2)^2}{4D\tau}\right). \quad (\text{Eq. 58})$$

Inserting of Eq. 58 and the double-cone shaped MDE function given by Eq. 40 into Eq. 57 yields

$$G(\tau) = \frac{1}{\bar{C}} \frac{1}{\sqrt{4\pi D \tau}} \frac{\iint \frac{\kappa(z_1) \kappa(z_2)}{8D\tau + w^2(z_1) + w^2(z_2)} \exp\left(-\frac{(z_1 - z_2)^2}{4D\tau}\right) dz_1 dz_2}{\frac{\pi}{2} \left( \int \kappa(z) dz \right)^2}. \quad (\text{Eq. 59})$$

The integrals in Eq. 59 can only be solved numerically.

By correlation analysis of the recorded fluorescence signal, a so-called auto-correlation curve can be calculated that can be fitted by an appropriate model function (Figure 9). The

width of the calculated correlation curves is proportional to the mean residence time of the molecules in the focus volume. If the focus geometry is known, the molecules diffusion coefficient can be determined. Furthermore, the correlation curves' amplitude is proportional to the average number of molecules in the focus volume. The molecules' concentration can be calculated if the volume of the focus was determined before, or according to a reference measurement. FCS is ideally suited to measure the diffusion coefficient of fast molecules at moderate to low concentrations, since high concentrations result in low molecule number fluctuations in the focus volume and thus low correlation amplitudes. The shape of calculated correlation curves is dependent on photophysical effects, mobility and interactions of the fluorophore and the MDE volume geometry.

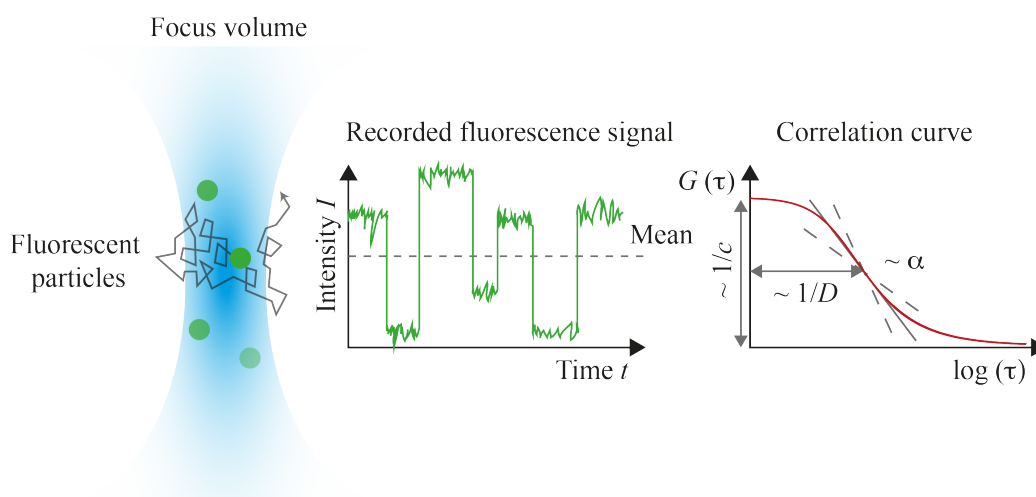


**Figure 9:** Fluorescent molecules diffuse into and out of a diffraction-limited illuminated focus volume. The fluctuating number of molecules in the focal volume results in a fluctuating fluorescence signal as a function of time recorded by a detector. This fluorescence signal can be correlated with a copy of itself to obtain a so-called auto-correlation function  $G(\tau)$ . From the amplitude of  $G(\tau)$ , the molecules' concentration can be determined and its width is proportional to the mean residence time and thus inversely proportional to the molecules' diffusion coefficient. The slope at the inflection point of  $G(\tau)$  is related to the anomaly parameter of fractal diffusion models.

### II.3.3 Dual-color fluorescence cross-correlation spectroscopy

The binding reaction of two interacting molecules of similar molecular weight cannot be measured by conventional FCS experiments, due to an only slightly slower component in the auto-correlation curve. For this purpose, the interacting molecules are labeled with fluorophores of spectrally separated emission maxima, e.g. with a red and a green



fluorescent dye (Rarbach et al., 2001; Rippe, 2000; Schwille et al., 1997; Weidemann et al., 2002). Two laser beams for excitation of the red and green dyes are focused to the same position in the sample and the emitted fluorescence light is collected by an objective lens. The red and green signals are separated on the detection light path of the microscope by a dichroic mirror.

In the sample, three species of molecules can be distinguished: Only green labeled molecules (G), only red labeled molecules (R) and complexes of interacting red and green labeled molecules (GR). By correlating the green fluorescence signal, molecules G and complexes GR contribute to the calculated auto-correlation curve. The auto-correlation curve of the red fluorescence signals consists of contributions of both R and GR, accordingly. To solely measure diffusion of complexes GR, the green fluorescence signal can be cross-correlated (CC) with the signal of the red detection channel. Only molecules that have a red and a green label contribute to the CC curve. The fluorescence intensity  $I_{\text{green}}$  that is detected in the green channel is emitted by molecules G and complexes GR as given by Eq. 52, if the quantum yield of green dye is not changed in the complex:

$$I_{\text{green}}(t) = I_{\text{green,G}}(t) + I_{\text{green,GR}}(t) = B_{\text{green}} \int_V \Psi_{\text{green}}(\vec{r}) (C_{\text{green,G}}(\vec{r}, t) + C_{\text{green,GR}}(\vec{r}, t)) d^3r. \quad (\text{Eq. 60})$$

Accordingly, the fluorescence intensity  $I_{\text{red}}$  in the red detection channel is given by

$$I_{\text{red}}(t) = I_{\text{red,R}}(t) + I_{\text{red,GR}}(t) = B_{\text{red}} \int_V \Psi_{\text{red}}(\vec{r}) (C_{\text{red,R}}(\vec{r}, t) + C_{\text{red,GR}}(\vec{r}, t)) d^3r. \quad (\text{Eq. 61})$$

Therefore, the auto-correlation function  $G_{\text{green}}$  of the green detection channel without spectral cross-talk between both detection channels reads

$$\begin{aligned} G_{\text{green}}(\tau) &= \frac{\langle \delta I_{\text{green}}(t) \delta I_{\text{green}}(t + \tau) \rangle}{\langle I_{\text{green}}(t) \rangle^2} \\ &= \frac{\langle \delta I_{\text{green,G}}(t) \delta I_{\text{green,G}}(t + \tau) \rangle + \langle \delta I_{\text{green,GR}}(t) \delta I_{\text{green,GR}}(t + \tau) \rangle}{\left( \langle I_{\text{green,G}}(t) \rangle + \langle I_{\text{green,GR}}(t) \rangle \right)^2}. \end{aligned} \quad (\text{Eq. 62})$$

By inserting the auto-correlation function of a single component given by Eq. 59 into Eq. 62, it can be expressed by

$$G_{\text{green}}(\tau) = \frac{\overline{C}_G^2}{(\overline{C}_G + \overline{C}_R)} G_{\text{green,G}}(\tau) + \frac{\overline{C}_{\text{GR}}^2}{(\overline{C}_G + \overline{C}_R)} G_{\text{green,GR}}(\tau). \quad (\text{Eq. 63})$$

Accordingly, the auto-correlation function  $G_{\text{red}}$  of the red detection channels is

$$G_{\text{red}}(\tau) = \frac{\overline{C}_R^2}{(\overline{C}_G + \overline{C}_R)} G_{\text{red,R}}(\tau) + \frac{\overline{C}_{\text{GR}}^2}{(\overline{C}_G + \overline{C}_R)} G_{\text{red,GR}}(\tau). \quad (\text{Eq. 64})$$

To obtain the fraction of complexes RG, the cross-correlation function of the green and red fluorescence signals can be calculated by

$$G_{\text{cross}}(\tau) = \frac{\langle \delta I_{\text{green}}(t) \delta I_{\text{red}}(t + \tau) \rangle}{\langle I_{\text{green}}(t) \rangle \langle I_{\text{red}}(t) \rangle} = \frac{\langle \delta I_{\text{green,GR}}(t) \delta I_{\text{red,GR}}(t + \tau) \rangle}{\langle I_{\text{green}}(t) \rangle \langle I_{\text{red}}(t) \rangle}. \quad (\text{Eq. 65})$$

By inserting Eq. 60 and Eq. 61 into Eq. 65, the following expression can be derived for the cross-correlation function:

$$G_{\text{cross}}(\tau) = \frac{B_{\text{green}} B_{\text{red}} \iint \Psi_{\text{green}}(\vec{r}_1) \langle \delta C_{\text{GR}}(\vec{r}_1, t) \delta C_{\text{GR}}(\vec{r}_2, t + \tau) \rangle \Psi_{\text{red}}(\vec{r}_2) d^3 r_1 d^3 r_2}{B_{\text{green}} B_{\text{red}} (\overline{C}_G + \overline{C}_{\text{GR}})(\overline{C}_R + \overline{C}_{\text{GR}}) \int \Psi_{\text{green}}(\vec{r}_1) d^3 r_1 \int \Psi_{\text{red}}(\vec{r}_2) d^3 r_2}. \quad (\text{Eq. 66})$$

If the complex concentration  $C_{\text{GR}}$  at time  $t$  and position  $\vec{r}_1$  is correlated with that at time  $t + \tau$  and position  $\vec{r}_2$  due to diffusion, Eq. 66 can be converted to

$$G_{\text{cross}}(\tau) = \frac{\overline{C}_{\text{GR}}}{(\overline{C}_G + \overline{C}_{\text{GR}})(\overline{C}_R + \overline{C}_{\text{GR}})} \frac{1}{\sqrt{4\pi D_{\text{GR}} \tau}} \cdot \frac{\iint \frac{\kappa_{\text{green}}(z_1) \kappa_{\text{red}}(z_2)}{8D_{\text{GR}} \tau + w_{\text{green}}^2(z_1) + w_{\text{red}}^2(z_2)} \exp\left(\frac{-(z_1 - z_2)^2}{4D_{\text{GR}} \tau}\right) dz_1 dz_2}{\frac{\pi}{2} \int \kappa_{\text{green}}(z_1) dz_1 \int \kappa_{\text{red}}(z_2) dz_2}. \quad (\text{Eq. 67})$$

Because spectral crosstalk of the green fluorophores into the red detection channel cannot be avoided experimentally, measured AC and CC curves have to be corrected. A correction approach was proposed by Erdel (Erdel, 2012). According to this approach, crosstalk corrected curves can be calculated from the measured curves (Eq. 68) if the bleed through-factor  $\kappa$  of green fluorescent light into the red detection channel is determined. It has to be measured for each combination of fluorophores and optical filter sets.

$$\begin{pmatrix} G_{\text{green}}^i(\tau) \\ G_{\text{cross}}^i(\tau) \\ G_{\text{red}}^i(\tau) \end{pmatrix} = \begin{pmatrix} 1 & 0 & 0 \\ -\gamma(1-\gamma)^{-1} & (1-\gamma)^{-1} & 0 \\ \gamma^2(1-\gamma)^{-2} & -2\gamma(1-\gamma)^{-2} & (1-\gamma)^{-2} \end{pmatrix} \begin{pmatrix} G_{\text{green}}(\tau) \\ G_{\text{cross}}(\tau) \\ G_{\text{red}}(\tau) \end{pmatrix}. \quad (\text{Eq. 68})$$

In Eq. 68,  $G_{\text{green}}^i(\tau)$ ,  $G_{\text{cross}}^i(\tau)$  and  $G_{\text{red}}^i(\tau)$  are the ideal or crosstalk free correlation curves that can be calculated from the measured curves  $G_{\text{green}}(\tau)$ ,  $G_{\text{cross}}(\tau)$  and  $G_{\text{red}}(\tau)$ . The parameter  $\gamma$  is calculated from the averages of the fluorescence intensities  $I_{\text{green}}$  and  $I_{\text{red}}$  measured in the green and red detection channel, respectively:

$$\gamma = \kappa \langle I_{\text{green}} \rangle \langle I_{\text{red}} \rangle^{-1}. \quad (\text{Eq. 69})$$

### II.3.4 Dual-focus fluorescence cross-correlation spectroscopy

Anisotropic transport phenomena like flow or diffusive flux can be measured based on FCS by creating a second illumination and detection volume in the sample that is spatially separated from the first one (Brinkmeier et al., 1999). This approach is called dual-focus fluorescence cross-correlation spectroscopy (dual-focus FCCS). If the distance between both detection volumes is known, diffusion coefficients can be measured with high precision (Dertinger et al., 2007). Dual-color FCCS is robust against experimental artifacts due to optical factors like cover slide thickness variations, refractive index changes of the sample, laser beam geometry and optical saturation of the fluorophores (Dertinger et al., 2008). If the distance between both focus volumes is large in comparison to the focus size, the shape of calculated cross-correlation curves gets independent of the actual detection volume geometry. Two spatially separated focus volumes can be created in the sample by using a Normarski prism in the illumination beam path and two orthogonally linear-

polarized laser beams (Brinkmeier et al., 1999). A Normarski prism has two principal axes that are aligned with the orthogonal polarizations of the laser pulses. For this alignment, the prism deflects the laser beams into two different directions according to their polarization. By focusing this light through the objective lens into the sample, two spatially shifted illumination volumes are generated (Figure 10). Fluorescence photons that are emitted in the excitation volumes are acquired with two detectors, each corresponding to a detection volume. The signal of each detection volume can be either auto-correlated with a copy of itself or additionally cross-correlated with the signal of the other detection volume. Cross-correlation analysis allows for determining the probability of a molecule to be detected at time  $t$  in the first volume and after a time lag  $\tau$  in the second volume.

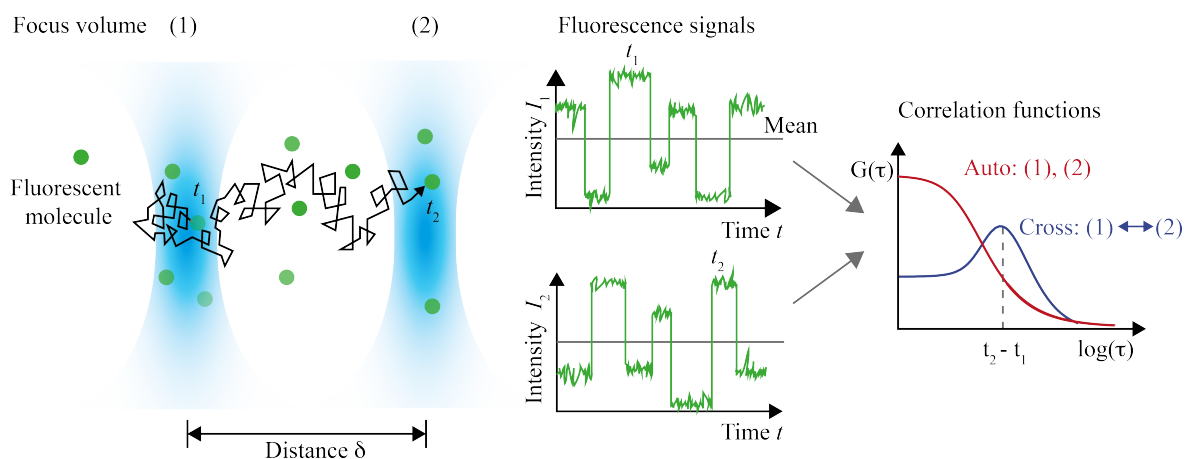


**Figure 10:** Two laser beams are focused into the sample. The created focus volumes are a distance  $\delta$  apart from each other. Fluorescent molecules enter and leave the illuminated focus volumes by transport processes like diffusion or flow. The fluorescence signal emitted in each focus volume is acquired with a detector. They can be either auto-correlated with a copy of themselves or cross-correlated with the signal of the other detection volume. Molecule detection at time  $t_1$  in the first focus volume and at time  $t_2$  in the second focus volume are correlated events due to the underlying transport process. For large distances, cross-correlation curves have a distinct peak at the molecules' most probable translocation time.

By reverse cross-correlation, anisotropy of molecules' transport process can be determined: For molecule exchange between two focus volumes by directed motion, the two acquired fluorescence signals are correlated in one, but not in the other direction. If molecules cannot be exchanged between the detection volumes due to an impermeable diffusion barrier, the amplitude of the cross-correlation curve is zero.

The cross-correlation between the fluorescence signals of detection volume  $\Psi_1$  at the origin  $\vec{r} = \vec{0}$  and  $\Psi_2$  at position  $\vec{r} = (0, \delta, 0)$  due to three-dimensional diffusion calculates as

$$G_{\text{cross}}(\tau) = \frac{\iint \Psi_1(\vec{r}_1) \langle \delta C(\vec{r}_1, t) \delta C(\vec{r}_2, t + \tau) \rangle \Psi_2(\vec{r}_2) d^3 r_1 d^3 r_2}{\bar{C}^2 \int \Psi_1(\vec{r}_1) d^3 r \int \Psi_2(\vec{r}_2) d^3 r_2}. \quad (\text{Eq. 70})$$

Remarkably, the cross-correlation function given by Eq. 70 is independent of the brightness  $B_1$  and  $B_2$  that are influenced by the quantum efficiency for detection of fluorescence photons of the detectors corresponding to detection volume 1 and 2, respectively. The MDE functions  $\Psi_1$  and  $\Psi_2$  are given by Eq. 71 and Eq. 72:

$$\Psi_1(\vec{r}_1) = \kappa_1(z_1) \frac{w_{0,1}^2}{w_1^2(z_1)} \exp\left(-2 \frac{x_1^2 + y_1^2}{w_1^2(z_1)}\right) \quad (\text{Eq. 71})$$

$$\Psi_2(\vec{r}_2) = \kappa_2(z_2) \frac{w_{0,2}^2}{w_2^2(z_2)} \exp\left(-2 \frac{x_2^2 + (y_2 - \delta)^2}{w_2^2(z_2)}\right). \quad (\text{Eq. 72})$$

By inserting the MDE functions Eq. 71, Eq. 72 and the diffusion propagator Eq. 58 into Eq. 70, the cross-correlation function can be written as

$$G_{\text{cross}}(\tau) = \frac{1}{\bar{C}} \frac{1}{\sqrt{4\pi D\tau}} \frac{\iint \frac{\kappa_1(z_1) \kappa_2(z_2)}{f(z_1, z_2, \tau)} \exp\left(-\frac{(z_1 - z_2)^2}{4D\tau} - 2 \frac{\delta^2}{f(z_1, z_2, \tau)}\right) dz_1 dz_2}{\frac{\pi}{2} \int \kappa_1(z_1) dz_1 \int \kappa_2(z_2) dz_2}. \quad (\text{Eq. 73})$$

The function  $f(z_1, z_2, \tau)$  is defined by

$$f(z_1, z_2, \tau) = 8D\tau + w_1^2(z_1) + w_2^2(z_2). \quad (\text{Eq. 74})$$

If the cross-correlation amplitudes are smaller than expected for free diffusion in aqueous solutions, molecules might get trapped or bound in crowded media like the interior of living cells.

### II.3.5 Scanning FCS and pair-correlation analysis

Instead of acquiring fluorescence signals for FCS analysis from a single position in a cell, confocal laser scanning microscopes (CLSMs) can be used to sequentially acquire FCS signals from multiple positions by either repeatedly scanning a line or circle in the sample with a laser beam (Petrasek and Schille, 2008) as depicted in Figure 11 a and c for a line scan measurement.

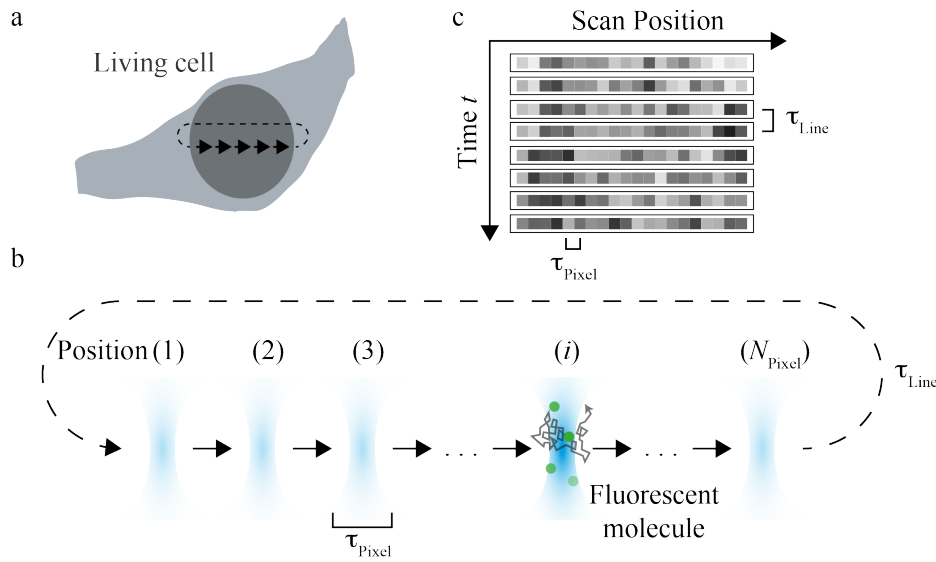


**Figure 11:** Line-scanning FCS data acquisition with confocal laser-scanning microscopes (CLSMs). **(a)** A line is repeatedly scanned in living cells to acquire fluorescence signals for scanning FCS analysis. **(b)**  $N_{\text{Pixel}}$  detection positions along a line in the sample are repeatedly scanned with a laser beam. The time period of the line scan process  $\tau_{\text{Line}}$  is the temporal resolution of fluorescence signals recorded from single positions. The dwell time of the laser beam at each position  $\tau_{\text{Pixel}}$  determines the number of recorded fluorescence photons. **(c)** Fluorescence signals acquired by CLSMs. The time lag between subsequent line-scans is  $\tau_{\text{Line}}$  and between subsequent detection positions  $\tau_{\text{Pixel}}$ . Sequentially acquired fluorescence signals of the same scan cycle are depicted in a horizontal line.

Scanning FCS allows for precise measurements of the diffusion coefficient in solution since it is less dependent on the microscope's MDE volume geometry and size. The inherent time information of the scan process allows for auto-correlation of signals from each position and for cross-correlation of signals from different positions along the scan trajectory. Correlation curves of several detection positions are commonly averaged to

compensate for limited dwell time of the illumination and detection beam at a certain position. Cross-correlation, or also called pair-correlation, analysis can be used to measure particle transport between different detection positions along the scan trajectory. It was used for imaging barriers for diffusing molecules (Digman and Gratton, 2009) and molecular flow (Hinde et al., 2010; Hinde et al., 2012) in living cells. For this purpose, correlation curves are plotted in columns of so-called correlation carpets. Each column of these carpets represents a position along the scan trajectory. Diffusion barriers are visible as gaps in the correlation carpets.

### **II.3.6 Multi-focus fluorescence (cross-) correlation spectroscopy**

The principle of FCS measurements at a single position (point-FCS) or with two focus volumes (2f-FCS) can be further extended by illuminating a several microns long line in the sample and detecting the emitted fluorescence signals with an electron multiplying charge-coupled device (EM-CCD) camera (Figure 12a). With this line-confocal microscopy setup (Heuvelman et al., 2009), hundreds of FCS measurements can be simultaneously conducted along a line (1D-FCS) to efficiently map molecules' mobility, concentration and interactions with high spatial and temporal resolution in living cells (Erdel et al., 2011). Besides the advantage for mobility mapping, a special feature of multi-focal setups is that the simultaneously acquired data of a single measurement contain information about molecules' mobility on multiple time and length scales. This information can be retrieved by spatially cross-correlating fluorescence signals acquired from different detection volumes in the sample for multiple separation distances. Calculated cross-correlation curves are proportional to probability distributions for the time  $\tau$  molecules need to diffuse the distance between two detection volumes (Figure 12b). A peak in the spatial cross-correlation curves marks the most probable translocation time. With recently developed single plane illumination microscopes (SPIM), parallel FCS measurement can be performed in a plane, which is referred to as 2D-FCS or SPIM-FCS (Capoulade et al., 2011; Singh et al., 2013; Wohland et al., 2010). Due to simultaneous illumination of a line or a plane in the sample and simultaneous detection of emitted fluorescence signals with high spatial resolution, detection crosstalk between neighboring detection volumes cannot be avoided. This auto-correlation type contribution to cross-correlation curves has to be described by accurately determining the microscope's MDE. The approaches for theoretically describing and for measuring microscopes' MDE

developed in this thesis can be easily adapted to analyze data that were acquired by SPIM setups.

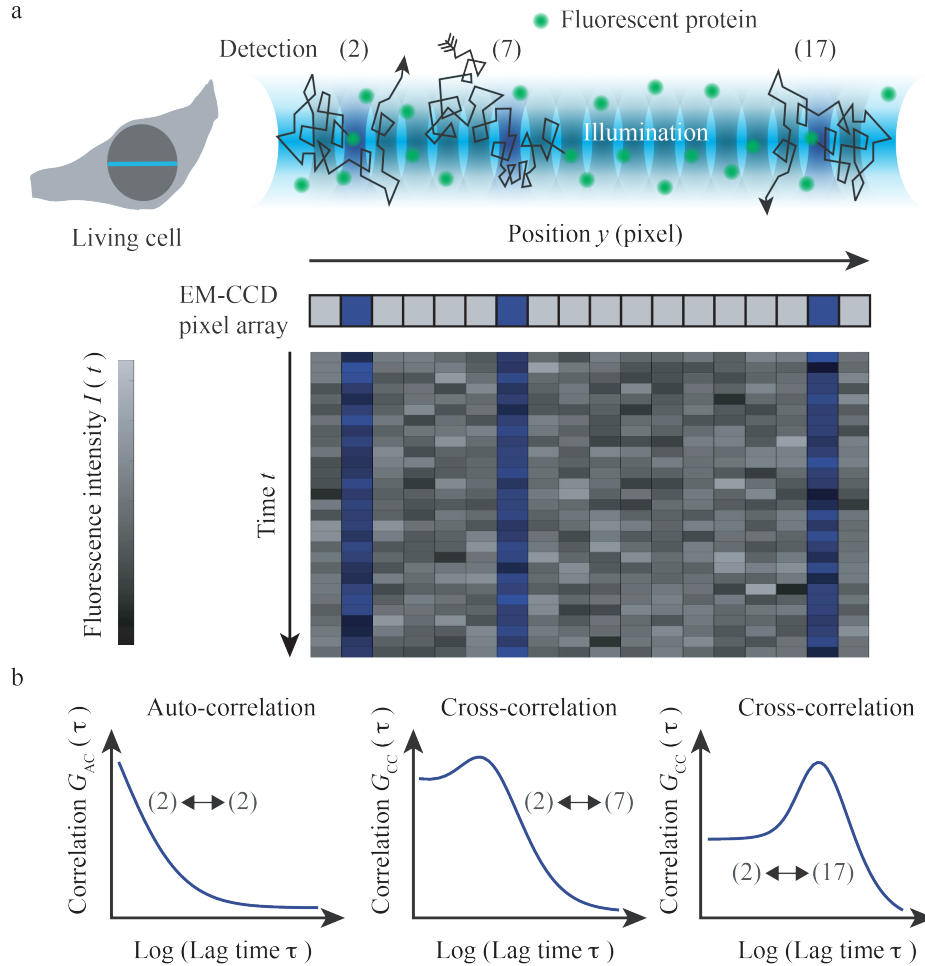


**Figure 12:** Data acquisition and analysis with a line illuminating and detecting microscope. **(a)** The line shaped laser beam profile is positioned to a region of interest in cells. Fluorescently labeled molecules diffuse into and out of the line illumination volume and emit fluorescence light that is detected by an EM-CCD camera – each pixel corresponds to a detection volume in the sample. The acquired fluorescence signals fluctuate due to fluctuating numbers of fluorescent molecules in the detection volumes. These intensity fluctuations can be analyzed by signal correlation to determine the molecules' diffusion coefficient and concentration. **(b)** The correlation analysis can be done in two different modes: Signals can either be auto-correlated with copies of themselves, e.g. signal of pixel 2 with itself, or cross-correlated with signals of other detection pixels for different separation distances, e.g. signal of pixel 2 with that of pixel 7 or 17. The width of auto-correlation (AC) curves is proportional to the mean residence time of molecules and the amplitude is inversely proportional to the mean molecule number in the detection volume. Cross-correlation (CC) curves show a peak at the time most molecules need to diffuse the distance between the corresponding detection volumes. The shape of short-distance CC curves depends on the detection crosstalk between detection volumes.



### **III Biological background**

Cells are the basic building units of all living organisms. In complex multicellular organisms like humans they have to fulfill a variety of different tasks. For example, in bones specialized cells give stability as structural building elements. Furthermore, electrical signals are transmitted over long distances by nerve cells, so-called neurons. For this purpose, they have to differentiate from the same pluripotent stem cell type to very specialized cell types. Despite this divergence between cells of the same organism, they have all the same inherited genetic information – but different functional programs are executed. The genome of eukaryotic cells is preserved in the nucleus, which is a cellular compartment enclosed by a lipid bilayer. It is surrounded by the cytoplasm, which consists of intracellular fluid, membrane-enclosed organelles and cytoskeletal filaments. To be viable, organisms have to react on stimuli from their environment, which are transmitted by complex signaling cascades to the different destination cells.

#### **III.1 *Cytoplasm***

In the cytoplasm, most of the cellular machinery, e.g. enzymes, is produced. It contains a scaffold structure of different protein filaments (cytoskeleton) and membrane-enclosed cytoplasmic organelles embedded by a viscous and crowded solution of various macromolecules (cytosol) (Alberts et al., 2002).

##### **III.1.1 Cytoskeleton**

Cytoskeletal filaments are polymers that are built of monomeric protein subunits. The cytoskeleton structure has different functions. (i) The cytoskeleton forms a scaffold structure that stabilizes and dynamically regulates the cellular shape as response to mechanical forces (Fletcher and Mullins, 2010). (ii) Parts of it are the driving force for cell division (Alberts et al., 2002), forming the mitotic spindle apparatus. (iii) It serves as rail system for active transport of small cellular organelles and vesicles by motor proteins like kinesin and dynein (Kamal and Goldstein, 2000; Vale and Milligan, 2000). (iv) The cytoskeleton allows for cell motility.

Three different classes of cytoskeletal protein filaments are known: microfilaments, intermediate filaments and microtubules. Microfilaments are flexible structures that are built of actin protein subunits. They have diameters of 5 - 9 nm (Alberts et al., 2002).

Intermediate filaments are ropelike fibers that have diameters of ~10 nm and are composed of a heterogeneous group of proteins, e.g. vimentin, keratin or lamin proteins (Alberts et al., 2002). The largest cytoskeletal fibers are the microtubules, which are hollow cylinders with an outer diameter of ~25 nm made of  $\alpha$ -tubulin and  $\beta$ -tubulin protein subunits. Microtubules form the mitotic spindle during cell division (Alberts et al., 2002). All three cytoskeletal filaments are dynamically assembled from subunits in the cytosol and disassembled.

### **III.1.2 Cytoplasmic organelles and vesicle traffic**

Besides cytoskeletal elements, several membrane-enclosed reaction volumes with defined pH values and ion concentration are found in the cytoplasm. One of these compartments is the endoplasmatic reticulum (ER) (Ellgaard and Helenius, 2001), which consists of multiple membrane stacks. It serves as a packaging center for sorting proteins that were previously produced in the cytosol or on the ER surface. Other cytoplasmic compartments are the mitochondria, the power stations of the cell, in which the cell's energy storage molecules, adenosine triphosphates (ATP), are synthesized (Alberts et al., 2002). Cell waste and messenger molecules are transported in vesicles through the cytoplasm to the cell surface where they fuse with the membrane to release their content into the extracellular space. On the contrary route, nutrients are imported in vesicles into the cytoplasm (Alberts et al., 2002).

### **III.1.3 Cytosol**

The cytosol is a viscous and crowded solution of highly concentrated macromolecules like nucleic acids, lipids and proteins. A total concentration of macromolecules in the range of 50 - 400 g/l, which corresponds to an occupied volume fraction of 5 – 40 % for the cell, was reported (Ellis and Minton, 2003). It embeds the cytoskeleton and cytoplasmic organelles. The viscous and elastic properties of the cytoplasm were described as homogeneous viscoelastic medium (Guigas et al., 2007). On the macroscale, the viscoelastic properties may be determined by the cytoskeleton whereas the nanoscale viscoelasticity may be determined by macromolecular crowding of the cytosol. Further, the cytoplasm is described by a coarse-grained model as biphasic system of a porous elastic solid meshwork bathed in interstitial fluid (Moeendarbary et al., 2013).

## **III.2 Nucleus**

The cell nucleus is surrounded by the cytoplasm. It is a hollow sphere with a diameter of 10 – 20  $\mu\text{m}$  (Wachsmuth et al., 2008) that is delimited by the nuclear envelope, which is formed by two concentric lipid bilayer membranes, and occupies  $\sim 10\%$  of the cellular volume (Alberts et al., 2002). The interior of the nucleus is packed with proteins, ribonucleic acids (RNA) and long polymers, so-called desoxyribonucleic acids (DNA) that encode the inherited genetic information of the organism (Rippe, 2007). DNA molecules form a highly compacted complex with proteins, so-called chromatin, which is heterogeneously distributed in the nucleus: Compartments of high chromatin density are surrounded by lacunae of less compacted chromatin (Cremer and Cremer, 2001). Many nuclear activities are concentrated in nuclear subcompartments or organelles (Handwerger and Gall, 2006) like the nucleolus (Boisvert et al., 2007), Cajal bodies (Cioce and Lamond, 2005) or PML nuclear bodies (Bernardi and Pandolfi, 2007; Chung et al., 2012). Furthermore, the nucleus is the principal site of RNA and DNA synthesis in cells (Alberts et al., 2002).

Small pores perforate the nuclear membrane to connect cytoplasm and nucleus. These pores are called the nuclear pore complexes (NPC). They allow small particles like ions or water molecules to freely exchange between both compartments. However, the exchange of larger molecules is actively controlled by the NPC, which results in different compositions and concentrations of cytoplasmic and nucleoplasmic ingredients. Therefore, different reaction environments are established.

The nucleus of healthy human cells contains 23 pairs of double-stranded DNA molecules, the so-called chromosomes that have double helical structure. Each double-strand DNA unit is highly compacted during cell division to a structure that is called metaphase chromosome. Condensed chromosomes are visible structures in conventional widefield microscopy images.

### **III.2.1 Desoxyribonucleic acid**

Single-stranded DNA molecules are linear polymers that are built of nucleotides as subunits and have a diameter of about 2 nm (Alberts et al., 2002). Each nucleotide consists of a five-carbon sugar (deoxyribose), a phosphate group and one of the four bases guanine (G), adenine (A), thymine (T) or cytosine (C). The bases A and T as well as the bases C

and G interact by forming non-covalent hydrogen bonds between them. Therefore, the pairs A-T and C-G are called complementary base pairs (bp). Two single-stranded DNA molecules are connected via hydrogen bonds between complementary base pairs to a double-stranded DNA unit. Therefore, double-stranded DNA contains twice the identical information, which can be valuable for repair of DNA damage. The actual sequence of base pairs along the DNA encodes the genetic information: A combination of three nucleotides encodes one amino acid. The assignment of nucleotide triplets to amino acids is called genetic code. A unit of genetic information that is required to build a protein consisting of a sequence of amino acids is called gene.

### **III.2.2 Chromatin fibers**

The total contour length of the double-stranded DNA in a human cell is about 2 m. Thus, DNA has to be highly compacted to fit into the relatively small cell nucleus with typical diameters of 10-20  $\mu\text{m}$ . This is accomplished by wrapping 147 bp of negatively charged DNA around a positively charged core of eight proteins, the so-called histone proteins. The complex of 147 bp DNA with the octamer of histone proteins is called nucleosome. Two of each of the histone proteins H2A, H2B, H3 and H4 form the octameric nucleosome core particle.

The nucleosomes along double stranded DNA appear as “beads on a string” and the resulting chromatin fiber has a diameter of about 10 nm (Woodcock and Ghosh, 2010). Nucleosomes are stabilized by linker histone protein H1. Each of the histone proteins has a tail that can be modified by covalently attaching or removing molecule groups like acetyl groups or methyl groups – so-called epigenetic modifications.

### **III.2.3 Higher order chromatin structures**

The cell nucleus is not homogeneously packed with chromatin: In fluorescence microscopy images of stained DNA, differently compacted regions are clearly visible (Cremer and Cremer, 2001). The following chromatin structures can be clearly observed by diffraction-limited fluorescence microscopy.

#### **III.2.3.1 Heterochromatin foci**

Different combinations of histone tail modifications are an additional opportunity for cells to store information on top of the genome. Therefore, this information is called epigenetic information. Epigenetic modifications like di- or trimethylation and hypoacetylation of

histone protein tails contribute to the formation of spherical spots of high chromatin density that are called heterochromatin foci (Grewal and Jia, 2007; Müller et al., 2009). These foci are surrounded by more loosely packed chromatin, so called euchromatin. Heterochromatin foci contain repeated sequences of non-coding DNA that are transcriptionally silenced. Euchromatic chromatin, however, is more permeable for transcription factors and RNA polymerase. Therefore, a higher transcription activity is observed in euchromatin.

### III.2.3.2 Chromosome territories and interchromosomal space model

A modulation of the chromatin density on a larger length scale occurs because different chromosomes are not intermingled in the cell nucleus. Instead, chromosomes segregate during interphase to discrete chromosome territories (CT) (Cremer and Cremer, 2001) that can be colored by fluorescence *in situ* hybridization (FISH) and visualized by confocal fluorescence microscopy (Figure 13).

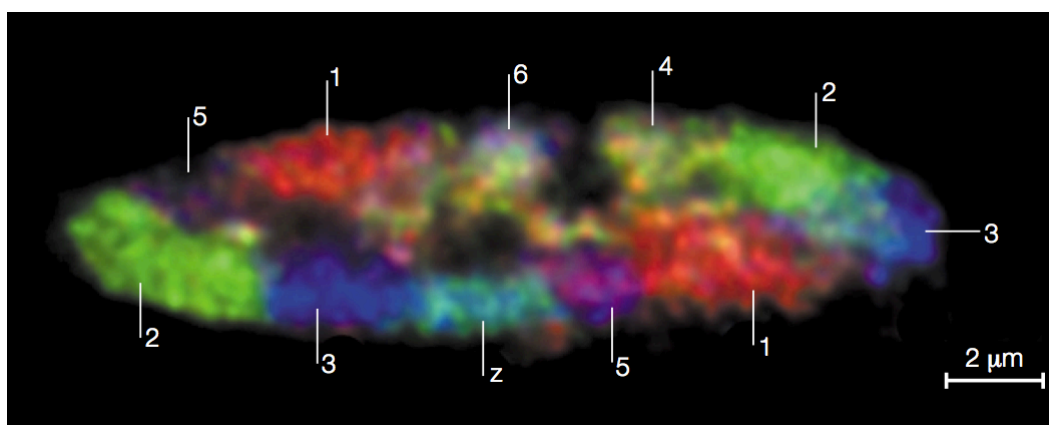


**Figure 13:** Cross-section through a chicken cell's nucleus. Different chromosomes (1-6) are stained by different fluorescent dyes via fluorescence in situ hybridization (FISH). Separation of the chromosomes into distinct territories is clearly visible. For chromosomes 4 and 6, only one territory is visible in this section. Image from Cremer and Cremer (Cremer and Cremer, 2001).

CT surround more open space that is called interchromosomal space (IC). The IC can form lacunas with diameters up to several micrometers (Figure 14) and small channels of several nanometers width (Cremer and Cremer, 2001). It permeates the CT with highly branched, interconnected channel networks and is enriched with protein complexes required for DNA transcription, replication and damage repair (Cremer and Cremer, 2010).

The IC is a highly transcriptional active compartment with a higher accessibility of genes at the surface of CT for chromatin binding proteins like transcription factors or polymerases. Each CT has a variable chromatin density. Denser chromatin regions are positioned near the CT centers, whereas loose chromatin loops expand to the IC, where they can interact with chromatin loops of other chromosomes. Dynamic modulation of the chromatin structure is proposed to be a mechanism for gene expression regulation by orchestrated gene activity and silencing. Overall, chromatin in the cell nucleus was described as a sponge like structure.

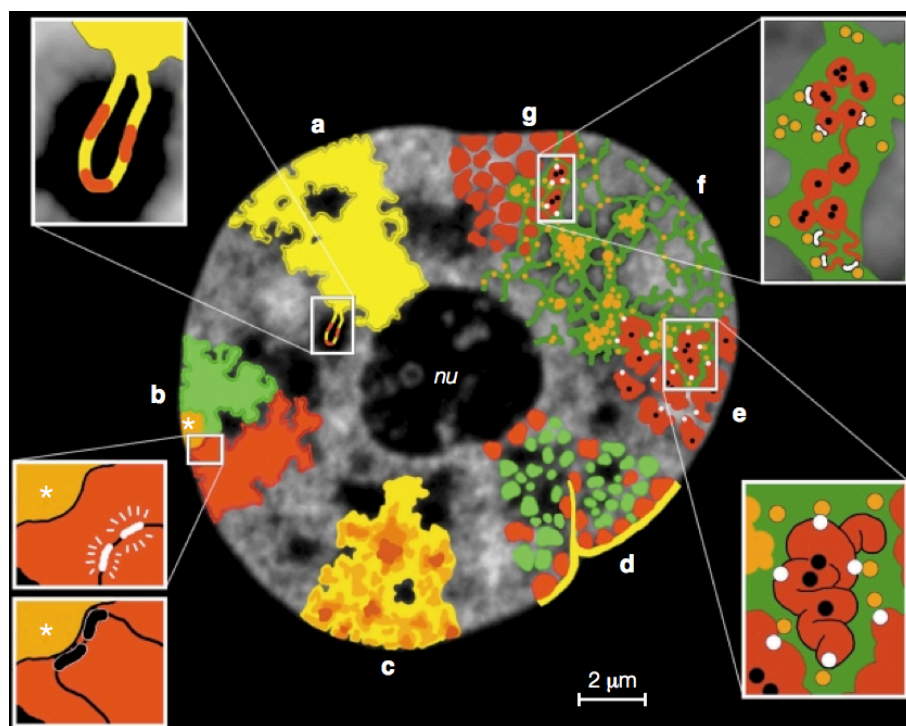


**Figure 14:** Illustration of the CT and IC model. **(a)** A large chromatin loop extends from a CT into the IC space where active genes are more accessible for transcription factors and polymerases. **(b)** Genes that are recruited to centromeric heterochromatin (asterisks) are silenced. **(c)** Heterogeneous chromatin density in CT (dark brown: high density, light yellow: low density). Loosely packed chromatin extends into IC space and densely packed chromatin with silenced genes is inside CT. **(d)** Gene rich chromatin domains (green) and gene poor domains around the nucleus (nuc) and near the nuclear lamina (yellow). **(e)** Active genes (white dots) at the surface of densely packed chromatin fibers and silenced genes (black dots) hidden inside chromatin structures. **(f)** The IC may contain large protein complexes (orange dots) for transcription, splicing, DNA replication and repair. **(g)** CT with domains (red) and IC (green) surrounding these domains. IC can be highly branched and form small channels. Image from Cremer and Cremer (Cremer and Cremer, 2001).

### III.3 *STAT signalling to chromatin as response to viral infections*

As a response to viral infections or virus-associated tumors, cells can react by releasing interferon (IFN) proteins into the extracellular fluid (Platanias, 2005; Stark and Darnell, 2012). These IFN proteins bind to IFN-receptors on the plasma membrane of other cells and activate receptor-associated JAK (Janus activated kinase) enzymes inside the cell. These enzymes phosphorylate STAT (signal transducer and activator of transcription) proteins (Figure 15). Several types of STAT proteins are known (Platanias, 2005), of which STAT1 and STAT2 were studied in this thesis. Phosphorylated STAT1 proteins can either form homodimers or heterodimers with phosphorylated STAT2 proteins. These dimers are imported into the nucleus, where they act as transcription activating factors upon binding to chromatin. As a result, the activated genes are transcribed. Finally, proteins are produced in response to the extracellular stimulation by interferons that are used for the defense of a viral infection of the cell.

The JAK/STAT signaling pathway is a typical example for transduction of extracellular stimuli into the nucleus and subsequent activation of gene transcription.

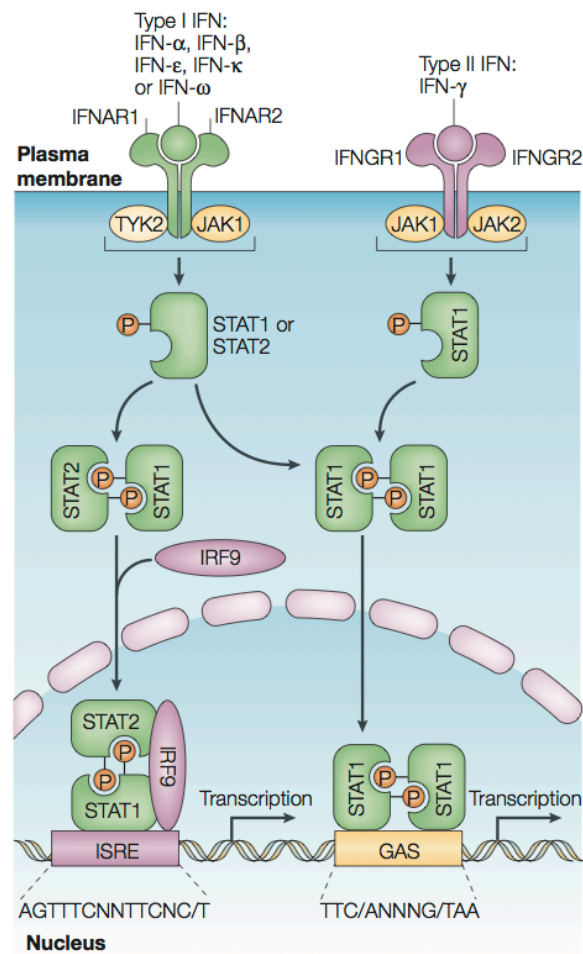


**Figure 15:** Interferon-mediated signaling by STAT proteins to chromatin. In response to viral infections, interferon (IFN) proteins are released that bind to receptors on the plasma membrane. Further, receptor-associated JAK enzymes are activated in the cell and phosphorylate STAT1 proteins. These activated STAT1 proteins form homodimers and heterodimers with STAT2 proteins that are imported into the nucleus, where they activate IFN-stimulated genes. As a result, proteins are expressed that are associated with virus defense. Image from Platanias (Platanias, 2005).

## IV Results

### IV.1 *Instrument characterization and reference measurements*

The microscope setup and data analysis workflow for spatial FCCS were characterized by *in vitro* measurement before protein transport and interactions could be reliably and quantitatively measured in living cells. For this purpose, an offset present in experimental correlation curves had to be corrected. Further, the impact of the laser illumination intensity on mobility measurements was tested. The precision of mobility mapping by EM-CCD camera based FCS with the line confocal microscope was determined. Finally, the accuracy of the derived correlation model function for diffusion was characterized.

#### IV.1.1 Correction of correlation curves' offset

Spatial cross-correlation functions for pixels with very large spatial separation ( $>5\ \mu\text{m}$ ) are expected to equal zero since there should be no significant particle transport between them. Instead, experimental cross-correlation curves for those separation distances converged to a constant correlation offset that is shown in Figure 16a. This offset within the correlation curves persisted even if the acquired fluorescence signals were corrected for slow signal trends. The average offset curve of a 1D-FCS measurement in a 20 nM aqueous solution of quantum dots (QDots) is depicted in Figure 16a. QDots are semiconductor nanocrystals that are extremely robust with regard to photobleaching of the fluorescence (Medintz et al., 2005). Most probable, this correlation offset originated from slow temporal fluctuations of the illumination intensity due to laser power instabilities that were not easily to correct. The resulting low-amplitude correlation was negligible for auto-correlation analysis at moderate molecule concentration. However, these offset correlation were more pronounced for long-distance cross-correlation curves that have much lower amplitudes. By increasing the stringency of the developed signal trend correction filter, this low-amplitude correlation offset could be removed. However, it had to be assured that low-amplitude correlations in long-distance cross-correlation curves that arise from transport of fluorescent molecules were not affected. Therefore, the average of about 30 long-distance cross-correlation curves that did not show diffusion peaks was subtracted from each single correlation curve, as shown by Figure 16b.



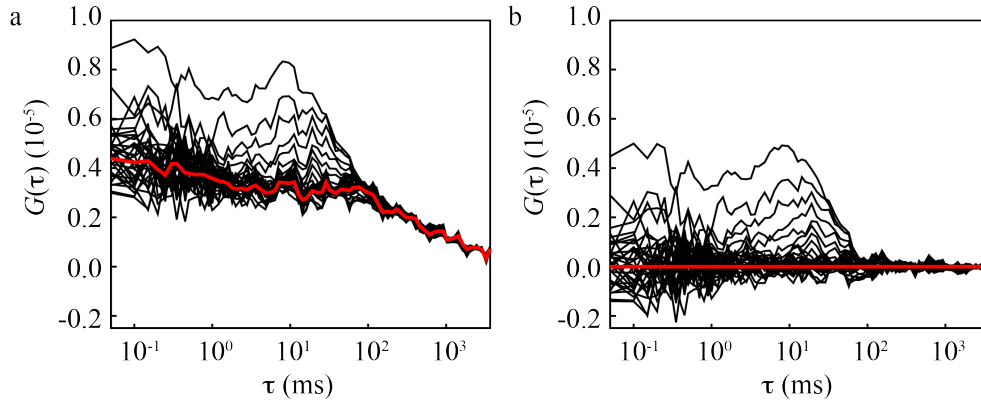


**Figure 16:** Correction of artificial offset in correlation curves. Cross-correlation curves were acquired in 20 nM aqueous solutions of QDots. **(a)** Cross-correlation curves (black) for separation distances in the range from 1.4  $\mu\text{m}$  to 8.0  $\mu\text{m}$ . The correlation curves converge for large distances to a correlation offset (red). **(b)** This offset can be corrected by subtracting the average of long-distance cross-correlation curves from each single curve. After correction, the values of long-distance cross-correlation curves fluctuate around zero.

#### IV.1.2 Impact of laser illumination intensity on measured mobility

It was shown that FCS measurements depend on the laser illumination intensity due to optical saturation effects that impact on the shape of the MDE volume and thus on the measured diffusion coefficients and concentrations (Enderlein et al., 2005; Gregor et al., 2005). To check the influence of the line-confocal microscope's illumination intensity on the shape of acquired correlation curves, the fluorescence intensity of GFP was measured in a mixture of glycerol ( $\phi = 25\%$ ) and phosphate buffered saline (PBS) solution as a function of the laser illumination intensity (Figure 17a). Optical saturation of fluorescence signal emitted by GFP was not achieved with the maximum laser power of 200 mW, because only a small fraction of the initial laser output intensity was transmitted through an optical fiber, a beam profile cropping rectangular aperture and the objective lens into the sample. Furthermore, the remaining illumination intensity was distributed in the focal plane over an about 50  $\mu\text{m}$  long and 200 nm wide area. Currently, only half of the emitted fluorescence signal could be detected since the longest commercially available confocal slit allowed for transmission of fluorescence light from only half of the illuminated area in the focal plane. The highest illumination intensity in the focal plane of the line-confocal microscope was 6.5  $\text{kW}/\text{cm}^2$ , which is well below the saturation intensity of  $\sim 33 \text{ kW}/\text{cm}^2$  for a typical fluorophore (Enderlein et al., 2005).

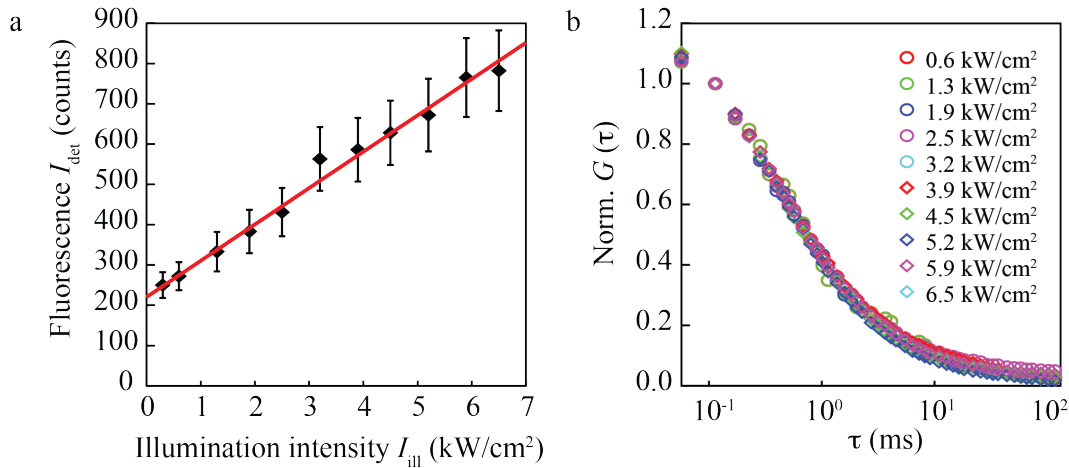


**Figure 17: (a)** Fluorescence saturation measurement of GFP in PBS buffer (black diamonds) including a linear fit of the data points (red line) that yields a background signal of 220 counts. Saturation of fluorescent dyes could not be achieved for the maximum available laser power. **(b)** Dependence of correlation curves on the laser illumination intensity. The correlation curves were normalized for a better comparison of their width at half maximum. No significant deviations between the diffusion times (width) from calculated correlation curves due to photobleaching of fluorophores was observed for illumination intensities in the range from 0.6 kW/cm<sup>2</sup> to 6.5 kW/cm<sup>2</sup>.

A potential problem for diffusion coefficient measurements is photobleaching of fluorescent molecules during their movement through the illumination PSF volume, which results in an apparently reduced residence time of the molecules in the focus volume. Glycerol was used to reduce the mobility of GFP molecules by increasing the solutions viscosity to mimic cellular conditions. Lower mobility of the fluorophore results in an increased amount of bleached fluorophores due to a longer excitation time. Even for the maximum available illumination intensity in the focal plane of the line-confocal microscope, no significant distortions of the correlation curves' shape (Figure 17b) and measured diffusion coefficients compared to low illumination intensities were observed.

### IV.1.3 *In vitro* characterization and reference measurements

#### IV.1.3.1 Precision of 1D-FCS mobility mapping

The precision of mobility mapping by 1D-FCS with the line-confocal microscope was assessed *in vitro* as a reference for mobility measurements in the spatially heterogeneous and crowded environment of living cells. For this purpose, the variation between the measured diffusion coefficients within a 1D-FCS measurement in a 20 nM aqueous solution of QDots was determined. Fluorescence signals recorded by the detector pixels of

the EM-CCD camera were auto-correlated and fitted with a model function (Eq. 92). The resulting auto-correlation curves calculated from fluorescence signals recorded by 40 neighboring pixels of the EM-CCD camera chip and their average are shown in Figure 18a. Profiles of the measured diffusion coefficients and concentrations along the detection line are depicted in Figure 18b. The relative standard deviation of both profiles is less than 4 % and the mean diffusion coefficient is  $D_{\text{mean}} = (31 \pm 1) \mu\text{m}^2\text{s}^{-1}$ . As quality criterion, auto-correlation curves that were acquired by neighboring pixels of the line-confocal microscope's EM-CCD camera should be scattered over a narrow range so that the measured diffusion coefficients have a small enough relative standard deviation ( $< 5\%$ ). If this criterion is fulfilled, the spatial heterogeneity of 1D-FCS mobility measurements in living cells can be meaningfully interpreted. Homogeneous 1D-FCS measurement results for diffusion coefficients and concentration can be achieved by correct alignment of the line-confocal microscope so that the resulting MDE volumes are comparable along the illuminated line. The confocal slit in the fluorescence detection light path should be aligned if the results of *in vitro* mobility measurements are heterogeneous since it has a major influence on the MDE volume geometry.

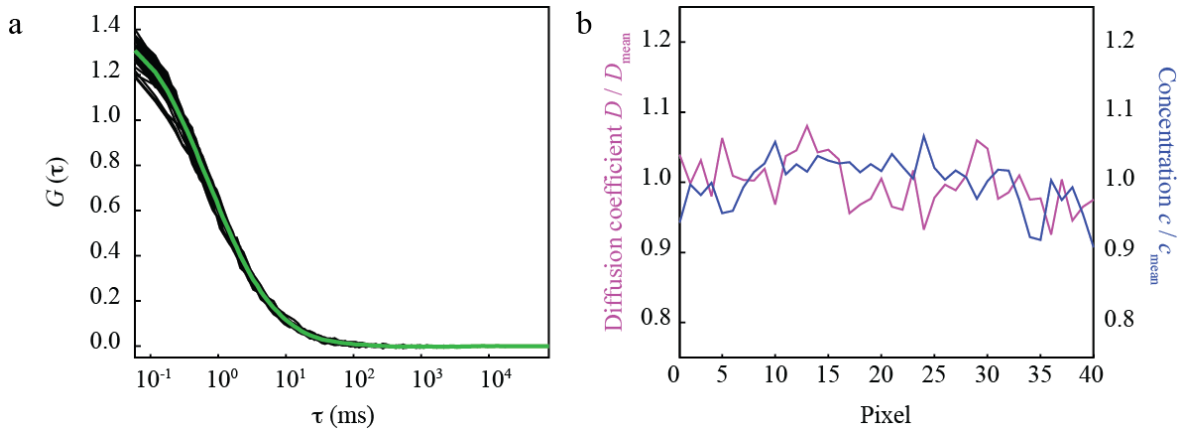


**Figure 18:** (a) Individual auto-correlation curves (black) and their average (green) from a 1D-FCS measurement in 20 nM concentrated aqueous solution of QDots. Correlation curves were calculated from the acquired signals of 40 neighboring detector pixels. The curves are scattered over a narrow range. (b) Diffusion coefficient and concentration profile along the detection line determined by fitting a model function to each calculated correlation curve. Both profiles have a relative standard deviation of about 4 %.

#### IV.1.3.2 Precision of 1D-FCS multi-scale mobility measurements

In addition to a small variance between mobility measurement results from different detector pixels, the diffusion coefficients of *in vitro* measurements for normal diffusion in aqueous solution have to be independent on the observation time and length scale, which is given for spatial FCCS measurements by the separation distance between corresponding detection volumes of cross-correlated fluorescence signals. It has to be validated, that the MSD of diffusing fluorescent dyes in aqueous solution is a linear function of the diffusion time. As shown in Figure 19a, a linear diffusion law was measured for QDots in aqueous solution. Additionally, the corresponding diffusion coefficients were plotted as a function of time in a double logarithmic representation (Figure 19b). This representation is more suitable for studying different scaling behaviors of the diffusion coefficient than MSD plots. As shown in Figure 19b, only minor differences were obtained for different cross-correlation distances. The results of spatial FCCS measurements depend strongly on the MDE's structural parameters assumed for the correlation model function (Eq. 92), especially for cross-correlation functions with short and medium separation distances ( $< 3 \mu\text{m}$ ). For larger separation distances, the measured diffusion coefficients become independent on the actual MDE geometry.

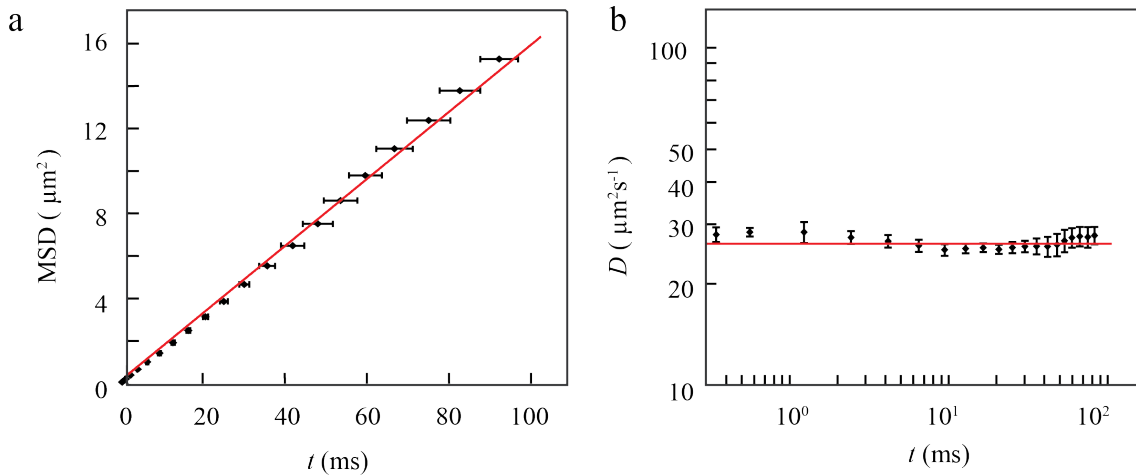


**Figure 19:** (a) MSD as a function of time for QDots diffusing in aqueous solution. The MSD grows linearly with time, as expected for normal diffusion. (b) Time dependence of the measured diffusion coefficient as a function of the diffusion time that is related to the spatial cross-correlation distance. In aqueous solution, the diffusion is independent on time and length scale of the applied mobility measurement technique.

*In vitro*, diffusion coefficients and concentrations measured by spatial FCCS should be independent of separation distances between detection volumes from. If these values change with different time and length scales, the structural parameters of the MDE function have to be measured again and adjusted correspondingly in the correlation model function (Eq. 92) by least squares fitting. A scale-independent mobility of reference dye molecules measured *in vitro* by spatial FCCS is essential for determining anomalous diffusion laws of molecules in the complex environment of living cells.

#### **IV.1.3.3 Accuracy of the diffusion correlation model function**

Another important criterion for quantitative analysis of spatial FCCS measurement is that experimental cross-correlation curves for different separation distances are equally well described by the same correlation model function. For this purpose, an accurate determination of the microscope's MDE's structural parameters is essential. Cross-correlation curves of QDots diffusing in aqueous solution and the corresponding fitted model functions for distances up to 3.8  $\mu\text{m}$  are depicted in Figure 20 for an optimized set of the line-confocal microscope's MDE structural parameters. As shown in Figure 20, the auto-correlation type contribution to cross-correlation curves arising from spatially overlapping MDE volumes and the resulting detection crosstalk was correctly described for all correlation distances. Poor fitting quality of the model function (Eq. 92) would lead to incorrect results for the measured diffusion coefficients and concentrations. If significant deviations between experimental correlation data and the correlation model function are observed, the assumed structural parameters for the microscope's MDE function have to be checked. Only when these quality criteria are met in *in vitro* 1D-FCS measurements with the line-confocal microscope, reliable mobility mapping and spatial FCCS measurements on multiple scales can be conducted in living cells.

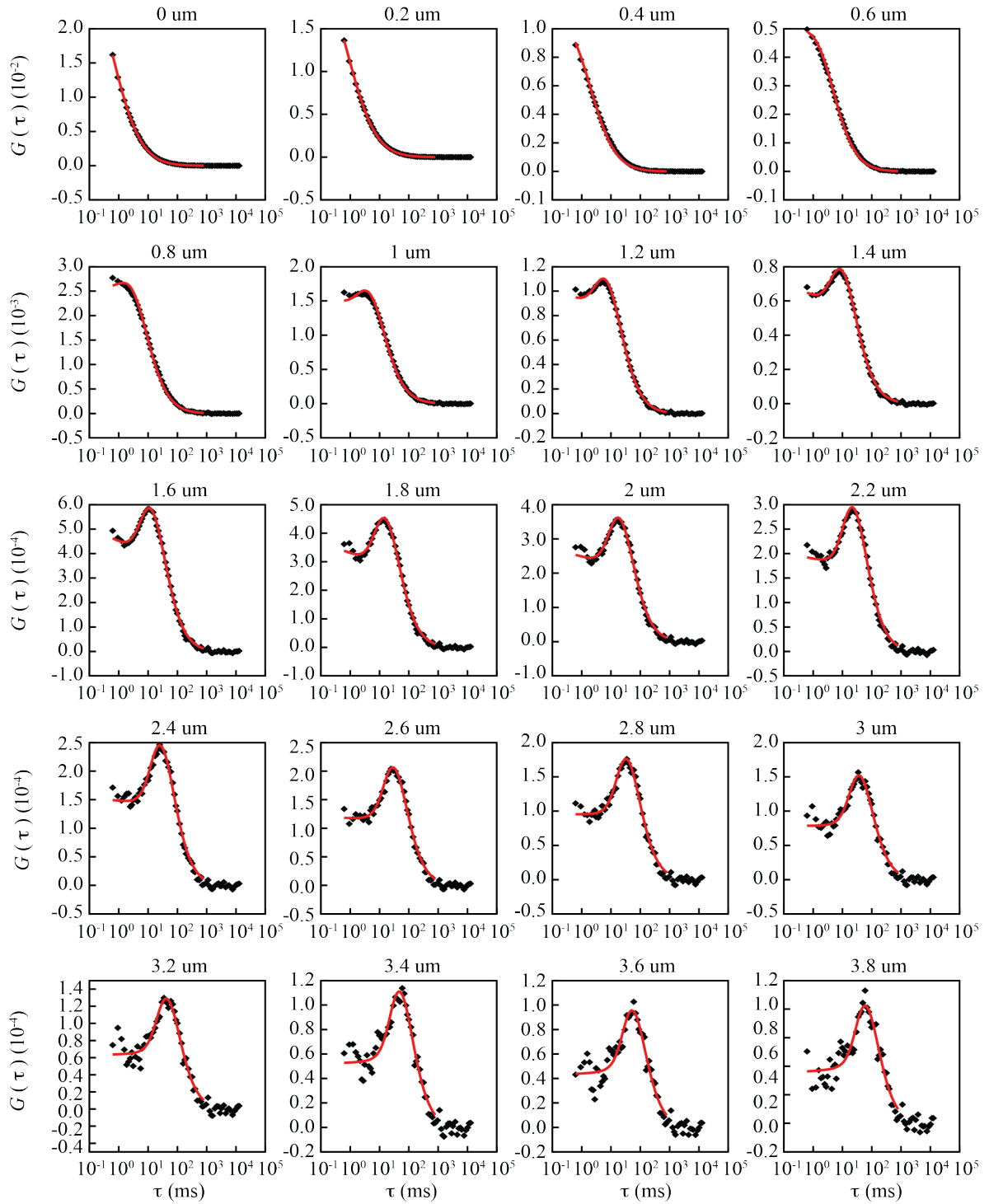


**Figure 20:** Auto- and cross-correlation curves of a 1D-FCS measurement in a 20 nM concentrated aqueous solution of QDots for distances up to 3.8  $\mu\text{m}$  (black diamonds). Additionally, the fitted model functions are depicted (red lines). For quantitative spatial cross-correlation analysis in living cells, cross-correlation curves for different distances have to be correctly described by the same correlation model function that depends for medium separation distances on the MDE function of the microscope. Detection crosstalk between neighboring detection volumes results in auto-correlation type contributions to cross-correlation curves that was observed for correlation distances up to 3.8  $\mu\text{m}$ .

## IV.2 Signal correction in Fourier space

Fluorescence signals that were acquired with line-confocal microscopes in the nucleus of living cells were usually exponentially decaying as a function of time due to photobleaching of fluorescent molecules in the illumination volume. 1D-FCS measurements are comparable to parallelized conventional FCS measurements at several hundred positions. This results in significant bleaching of the limited pool of fluorescent dyes in the nucleus in mostly out-of-focus regions, which does not affect the measured diffusion times but deforms the calculated correlation curve. Exponentially decaying fluorescence signals due to photobleaching (Figure 21a) are temporarily correlated as calculated and shown in Figure 21b.

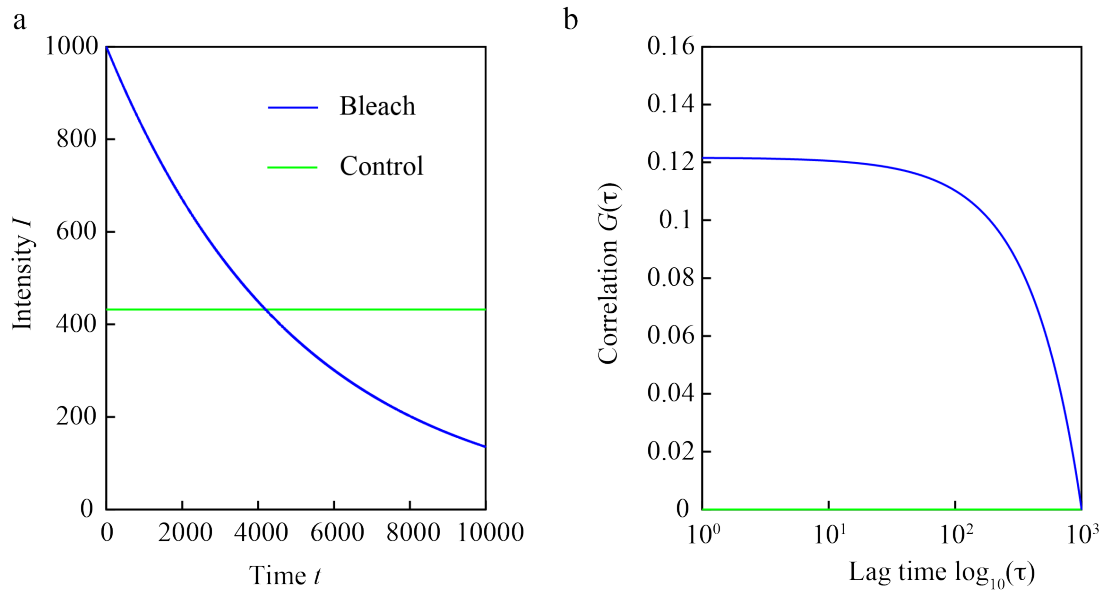


**Figure 21:** Correlation resulting from a trend in the fluorescence signal, for example due to bleaching of fluorescent dyes. **(a)** A constant signal (green) and an exponentially decaying signal (blue) with equal mean values. The decaying signal is similar to that of a recorded fluorescence signals with photobleaching of the fluorescent dyes. **(b)** Correlation curves of the constant signal and the bleach signal. The exponentially decaying signal is temporarily correlated, whereas the constant signal shows zero correlation. Real FCS signals have additional signal fluctuations due to diffusion of fluorescent molecules that are correlated.

For a quantitative analysis of FCS experiments, this trend of fluorescence signals has to be corrected properly. For this purpose, different strategies were compared, including correction by a moving average approach or by fitting an exponentially decaying function. Both strategies work fine for constant or smoothly decaying signals. However, fluorescence signals from measurements in living cells are commonly shaky, e.g. due to

movements of large non-fluorescent cellular components through the detection volumes. These signals can only be incompletely corrected by the previously introduced strategies. The resulting correlation artifacts are particularly pronounced in cross-correlation curves for large separation distances, whereas auto-correlation curves are only moderately affected. Therefore, a new approach was developed in this thesis that allows quantitative analysis of spatial FCCS measurements - even in the heterogeneous environment of living cells. This new approach is based on transforming the fluorescence signals  $I(t)$  to frequency space

$$\tilde{I}(\nu) = \text{FT}(I(t)) \quad (\text{Eq. 75})$$

and correcting the low frequency components of the Fourier spectra  $\tilde{I}(\nu)$  to remove slow intensity fluctuations in the time domain:

$$I_{\text{corrected}}(t) = \text{FT}^{-1}(\tilde{I}_{\text{corrected}}(\nu)). \quad (\text{Eq. 76})$$

For correction of the Fourier spectra, the spectra of signals of measurements in homogenous aqueous solutions were used as references. For the theoretical description of Fourier spectra an envelope function was calculated for each spectrum. The envelope function values  $e_i$  was based on the mean value  $\mu_i$  and the standard deviation  $\sigma_i$  calculated within a moving window  $i$  of twenty data points along the frequency axis. The envelope function  $e_i$  was defined as

$$e_i = \mu_i + 3\sigma_i. \quad (\text{Eq. 77})$$

The envelope of the Fourier spectrum of GFP in aqueous glycerol solution ( $\phi = 25\%$ ) was fitted by an empirical model function given by

$$f_{\text{water}}(\nu) = a_1 \exp(-k_1 \nu) + a_2 \exp(-k_2 \nu) + a_3 \exp(-k_3 \nu). \quad (\text{Eq. 78})$$

In this manner, the water envelope parameters  $a_1$ ,  $a_2$ ,  $a_3$ ,  $k_1$ ,  $k_2$  and  $k_3$  were determined as reference. For comparison, an aqueous glycerol solution was used to match the diffusion



coefficient to that in cell measurements. For the correction of trend-containing Fourier spectra of GFP in living cells, an envelope function  $f(v)$  was proportional to the water envelope function  $f_{\text{water}}(v)$  with the parameters determined above was fitted to the Fourier spectra obtained in living cells. The envelope model function with a fit parameter  $C$  is defined by Eq. 79:

$$f(v) = C \cdot f_{\text{water}}(v). \quad (\text{Eq. 79})$$

By cropping the high amplitude values at low frequencies of trend-containing Fourier spectra according to the fitted water envelope function and subsequent back transformation into the time domain, fluorescence signals were trend-corrected prior to correlation analysis.

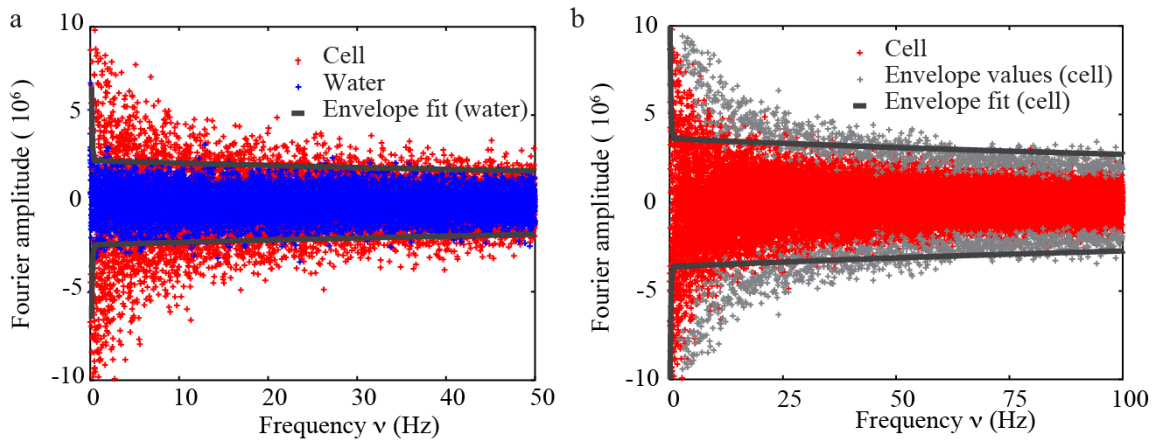


**Figure 22:** (a) Fourier spectra of fluorescence signals obtained from GFP in aqueous glycerol solution (blue) and from GFP in the nucleus of a living cell (red). The Fourier spectrum obtained in cells shows higher amplitude values at lower frequencies compared to a Fourier spectrum obtained from a water measurement. The envelope of the water spectrum, defined by Eq. 77, was fitted by an envelope function (dark grey) given by Eq. 78. (b) The water envelope function (dark grey) was fitted to the envelope values  $e_i$  (light grey) of the cell measurement Fourier spectrum (red) for subsequent trend correction.

The Fourier transformation based approach for signal trend correction was validated by artificially adding a signal function to data obtained from 20 nM QDots in aqueous solution and subsequent correction (Figure 23).

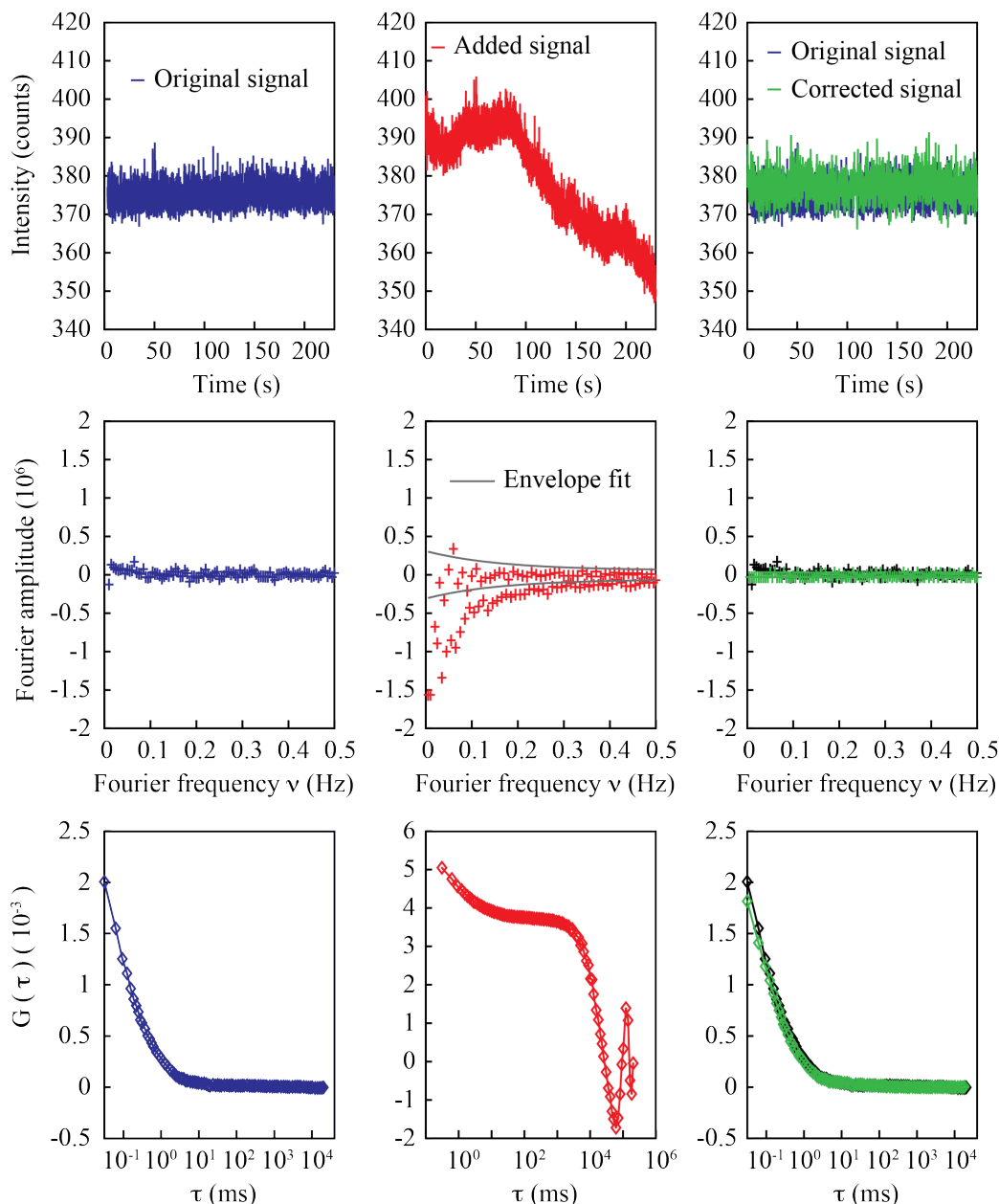


**Figure 23:** Validation of the Fourier transformation based approach for signal trend correction. An artificial signal function (middle) was added to a fluorescence signal of diffusing QDots in aqueous solution (left). The auto-correlation curve of the trend-containing fluorescence signal is distorted, whereas after correction of the Fourier spectrum (middle), the original auto-correlation curve could be recovered (right).

After correction in frequency space by fitting a reference envelope function and cropping the high amplitude values at low frequencies accordingly, the original auto-correlation curves could be reconstructed without deformations.

The approach was further validated by correcting the signals of larger and therefore slower TetraSpeck beads with a diffusion coefficient of  $\sim 4.4 \mu\text{m}^2\text{s}^{-1}$  (Muller et al., 2008).

Furthermore, the approach was tested by correcting the shaky decaying signals of the chromatin-interacting heterochromatin proteins 1 (HP1) labeled with green fluorescent protein (GFP) in the nucleus of living cells. A comparison between the moving average approach and the developed Fourier transformation based approach is shown in Figure 24.

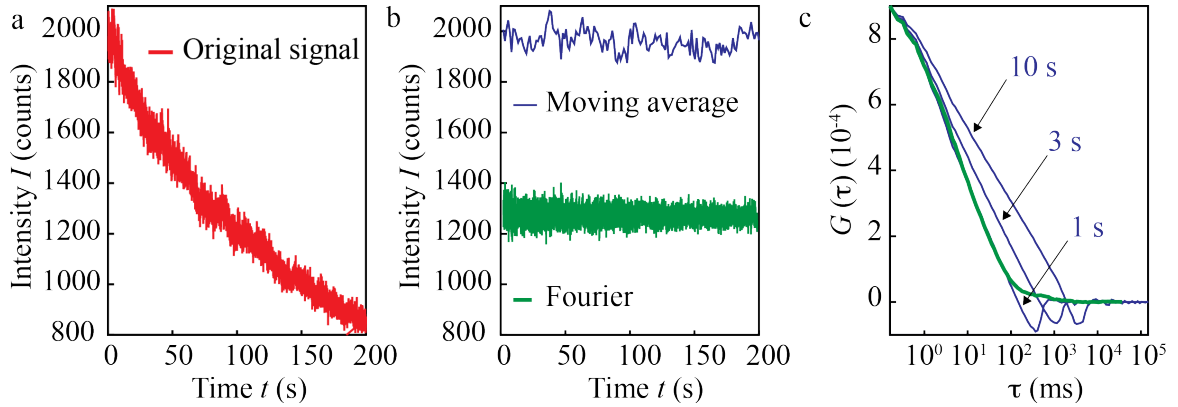


**Figure 24:** Comparison between moving average and Fourier transformation based signal trend correction approaches. **(a)** Decaying fluorescence signal of a 1D-FCS measurement of HP1-GFP fusion protein in the nucleus of a living cell. **(b)** Fluorescence signals corrected by the moving average approach with a correction window size of 1 s (blue) and by the Fourier transformation approach (green). **(c)** Calculated auto-correlation curves of moving average trend corrected fluorescence signals with 10 s, 3 s, and 1 s (blue) window size as well as a Fourier spectrum corrected signal (green). The shape of auto-correlation curves that were calculated based on signals corrected with the moving average strategy (blue) depends on the used trend correction window size. Furthermore, these curves (blue) show a dip at the time of the half window size, whereas the correlation curve of Fourier trend corrected signal is smooth. For moving average corrected signals, all correlations above time lags larger than half of the correction window size are removed.

As shown in Figure 24c, correlation curves that were calculated based on fluorescence signals corrected with the moving average approach show a dip at the time of the half window size and correlations above a longer time period are removed. For these reasons, the Fourier transformation based correction is better suited for spatial FCCS analysis since the measured diffusion times are longer and the relevant information is shifted to larger time scales in cross-correlation curves compared to auto-correlation curves.

### IV.3 Improved MDE model for line-confocal microscopes

#### IV.3.1 Derivation of an MDE model function for line-confocal microscopes

For quantitative auto- and cross-correlation analysis of 1D-FCS measurements with line-confocal microscopes, the microscope's MDE function has to be theoretically described with high accuracy since spatially overlapping detection volumes result in detection crosstalk. For this purpose, a theoretical model function for line-confocal microscopes' MDE function with improved accuracy was derived to correctly account for autocorrelation (AC)-type contributions due to spatially overlapping detection volumes. The MDE function  $\Psi$  of confocal microscopes in general can be calculated as the product of the microscope's illumination and detection PSF

$$\Psi(\vec{r}) = \text{PSF}_{\text{ill}}(\vec{r}) \cdot \text{PSF}_{\text{det}}(\vec{r}). \quad (\text{Eq. 80})$$

For fluorescence correlation spectroscopy (FCS) with conventional point illumination and detection confocal microscopy setups with high numerical aperture (NA) objective lenses, the MDE is approximated with sufficient accuracy by rotationally symmetric two-dimensional Gaussian functions in the focal plane, since diffraction rings of the illumination PSF and the detection PSF interfere destructively. However, the diffraction pattern surrounding the central main lobe cannot be neglected if the illumination PSF is constant in one direction (Figure 25). The MDE function of the microscope used here is theoretically described by a non-paraxial MDE model function (Dusch et al., 2007) that is only valid near the focal plane ( $z = 0$ ). It is given by

$$\begin{aligned} \Psi_{\text{NP}}(x, y, z) = & \left| \int_{-\alpha}^{\alpha} \sqrt{\cos(\Theta)} \exp(-ik_{\text{ex}} x \sin(\Theta)) \exp(-ik_{\text{ex}} z \cos(\Theta)) k_{\text{ex}} \cos(\Theta) d\Theta \right|^2 \\ & \times \int_{-s}^s \left| \int_0^{\alpha} \sqrt{\cos(\Theta)} J_0 \left( k_{\text{em}} \sin(\Theta) \sqrt{y^2 + (x - x_s)^2} \right) \exp(-ik_{\text{em}} z \cos(\Theta)) k_{\text{em}} \sin(\Theta) d\Theta \right|^2 dx_s. \end{aligned} \quad (\text{Eq. 81})$$

In Eq. 81,  $x$  and  $y$  are the axes perpendicular to and along the illumination line, respectively, and  $k_{\text{ex}}$  and  $k_{\text{em}}$  are the excitation and emission wave numbers, respectively. This MDE model function in the focal plane ( $z = 0$ ) is illustrated in Figure 25.

The model function Eq. 81 was approximated in the focal plane by a central asymmetric two-dimensional Gaussian function and four asymmetric two-dimensional Gaussian functions of lower amplitudes on each side of the main lobe in direction of the illumination line. The central main lobe is elongated in  $y$ -direction along the line, whereas the side lobes are elongated in  $x$ -direction perpendicular to the line (Figure 25). Diffraction rings perpendicular to the  $x$ -direction could be neglected due to their low amplitude for the description of the detection crosstalk along the illuminated line ( $x$ -direction).

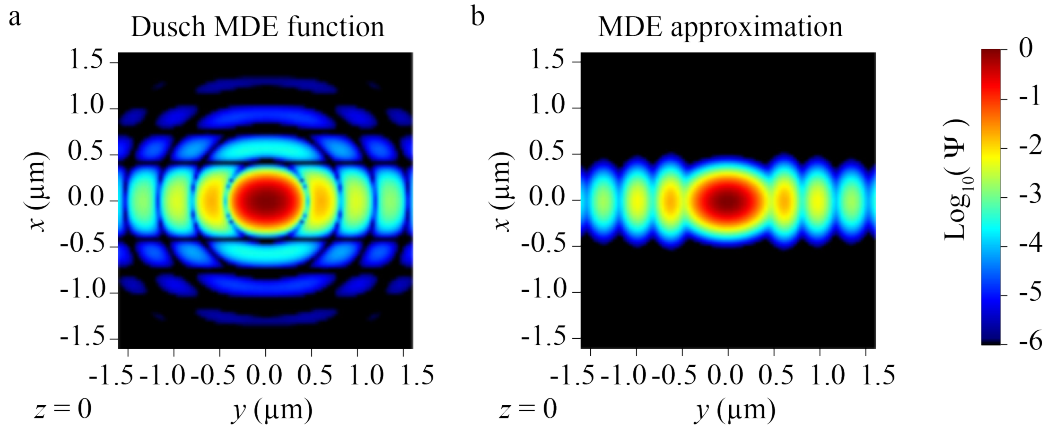


**Figure 25:** (a) Complex diffraction pattern of the MDE function according to (Dusch et al., 2007) for a line-confocal microscope in the focal plane ( $z = 0$ ). Only the first three side lobe orders are depicted. (b) Approximation of the diffraction pattern's main and side lobes by multiple asymmetric two-dimensional Gaussian functions. The diffraction rings perpendicular to the illumination line ( $x$ -direction) were neglected.

Because the model above derived by Dusch et al. (Dusch et al., 2007) is only valid near the focal plane, the MDE function is modeled in axial direction by a double cone shaped function motivated by Dertinger et al. (Dertinger et al., 2007). Accordingly, the complete three-dimensional MDE function with four side lobes on the left and on the right side of the central main lobe is approximated by Eq. 82

$$\Psi(\vec{r}) = \sum_{n=-4}^4 \psi_n(\vec{r}). \quad (\text{Eq. 82})$$

Each lobe  $\psi_n$  of the line-confocal microscope's MDE function is described by Eq. 83

$$\psi_n(\vec{r}) = A_n \kappa(z) \frac{w_{x,n}(0)}{w_{x,n}(z)} \frac{w_{y,n}(0)}{w_{y,n}(z)} \exp \left( -2 \frac{x^2}{w_{x,n}^2(z)} - 2 \frac{(y - y_n(z))^2}{w_{y,n}^2(z)} \right). \quad (\text{Eq. 83})$$

The functions  $w_{x,n}(z)$  and  $w_{y,n}(z)$  in Eq. 83 describe the width of the  $n^{\text{th}}$  MDE function lobe at axial position  $z$  in  $x$ - and  $y$ -direction, respectively:

$$w_{x,n}(z) = w_{x,n}(0) \cdot \left( 1 + (k_x z)^2 \right)^{\alpha_x}, \quad (\text{Eq. 84})$$

$$w_{y,n}(z) = w_{y,n}(0) \cdot \left( 1 + (k_y z)^2 \right)^{\alpha_y}. \quad (\text{Eq. 85})$$

Further, the parameter  $A_n$  gives the amplitude and  $y_n(z)$  the center position of the two-dimensional Gaussian function describing the  $n^{\text{th}}$  MDE lobe in a cross section through the MDE at a distance  $z$  from the focal plane:

$$y_n(z) = y_n(0) \cdot \left( 1 + (k_y z)^2 \right)^{\alpha_y}. \quad (\text{Eq. 86})$$

The structural parameters  $k_x$ ,  $k_y$ ,  $\alpha_x$  and  $\alpha_y$  can be determined by fitting the model functions to experimentally acquired three-dimensional image stacks of fluorescent beads that reveal the microscope's MDE. Out-of-focus light is blocked by a slit of width  $a$  in confocal position and by detection on a quadratic pixel of the EM-CCD camera detection array with side length  $b$ . Thus, the microscope's resolution in axial direction is improved by reducing the MDE extension, and the contrast is enhanced. The reduction of the MDE in axial direction can be calculated as follows: Without a confocal slit, the line-confocal microscopes MDE is described by Eq. 87

$$\tilde{\Psi}(\vec{r}) = \sum_{n=-4}^4 \tilde{\psi}_n(\vec{r}) \quad (\text{Eq. 87})$$

with the lobe functions given by Eq. 88

$$\tilde{\psi}_n(\vec{r}) = \frac{\psi_n(\vec{r})}{\kappa(z)} = A_n \frac{w_{x,n}(0) w_{y,n}(0)}{w_{x,n}(z) w_{y,n}(z)} \exp\left(-2 \frac{x^2}{w_{x,n}^2(z)} - 2 \frac{(y - y_n(z))^2}{w_{y,n}^2(z)}\right). \quad (\text{Eq. 88})$$

The fraction of fluorescence light from an axial position  $z$  that can pass through the confocal slit aperture can be described as being cropped by a rectangular aperture, which is expressed by Eq. 89

$$\kappa(z) = \frac{\int_{-a/2}^{a/2} \int_{-b/2}^{b/2} \tilde{\Psi}(\vec{r}) dx dy}{\int_{-\infty}^{\infty} \int_{-\infty}^{\infty} \tilde{\Psi}(\vec{r}) dx dy}. \quad (\text{Eq. 89})$$

The MDE side lobes in Eq. 89 can be neglected, because in this approximation the MDE is cropped by the confocal slit and thus only the main lobe contribution is remaining. Thus, the maximum value of the MDE at a distance  $z$  from the focal plane is given by Eq. 90

$$\kappa(z) = \frac{\int_{-a/2}^{a/2} \int_{-b/2}^{b/2} \psi_{0,0}(\vec{r}) dx dy}{\int_{-\infty}^{\infty} \int_{-\infty}^{\infty} \psi_{0,0}(\vec{r}) dx dy} = \text{erf}\left(\frac{a}{\sqrt{2} w_{x,0}(z)}\right) \text{erf}\left(\frac{b}{\sqrt{2} w_{y,0}(z)}\right). \quad (\text{Eq. 90})$$

The resulting MDE model function for line-confocal microscopes is depicted in Figure 26.

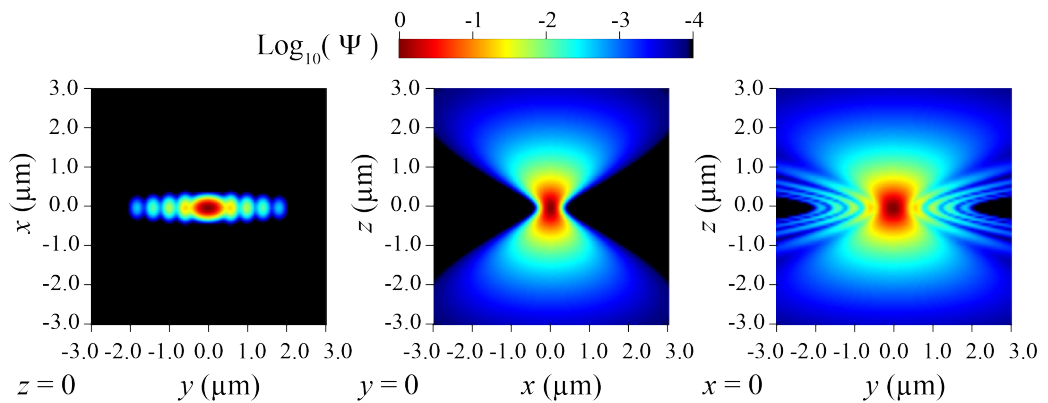


**Figure 26:** Illustration of the MDE model function expressed by Eq. 82. In the  $xy$ -cross-section ( $z = 0$ ), the central main lobe and four side lobes on its left and right side can be seen (left panel). The  $xz$ -cross-section ( $y = 0$ ) of the MDE function is similar to that of a conventional point-confocal microscope with a pinhole instead of a slit aperture. It shows the double-cone shape of a focused beam in axial direction (middle panel).

### IV.3.2 Derivation of a spatial cross-correlation function for double cone MDE

The shape of auto-correlation and medium-distance cross-correlation curves is determined by the microscope's MDE, photophysical properties of the fluorescent dyes and transport processes like diffusion or directed flow that are detected as intensity fluctuations of the fluorescence signal. To account for the properties of the crowded interior of living cells an anomalous diffusion propagator with a power law relation between the molecules' mean squared displacement (MSD) and time was used. However, the final results were essentially model-independent by calculating the effective diffusion time  $t_{\text{eff}}$  for the translocation of molecules from detection volume  $k$  to detection volume  $l$ . The anomalous diffusion propagator used here reads as follows

$$P_D(\vec{r}_2, \tau | \vec{r}_1, 0) = \frac{1}{(4\pi\Gamma\tau^\alpha)^{3/2}} \exp\left(-\frac{(\vec{r}_2 - \vec{r}_1)^2}{4\Gamma\tau^\alpha}\right). \quad (\text{Eq. 91})$$

With the improved MDE model function (Eq. 82) and the anomalous diffusion propagator (Eq. 91) a correlation model function  $G_{kl}(\tau)$  for diffusion was derived according to Eq. 70 that is given by Eq. 92. It can be applied for quantitative description of correlation curves obtained by correlating fluorescence signals acquired from MDE volumes  $\Psi_k$  and  $\Psi_l$ :

$$G_{kl}(\tau) = \frac{\int_V \int_V \Psi_k(\vec{r}_1) P_D(\vec{r}_2, \tau | \vec{r}_1, 0) \Psi_l(\vec{r}_2) d^3r_1 d^3r_2}{\int_V \Psi_k(\vec{r}_1) d^3r_1 \int_V \Psi_l(\vec{r}_2) d^3r_2} = \frac{1}{cV_{\text{eff}}} \sum_{m=-4}^4 \sum_{n=-4}^4 H_{klmn}(\tau). \quad (\text{Eq. 92})$$

For  $k=l$ , an auto-correlation (AC) curve is obtained, while  $k \neq l$  yields a cross-correlation (XC) curve. The mean number of particles in the focus volume is given by  $N = cV_{\text{eff}}$ . An effective volume is obtained by Eq. 93

$$V_{\text{eff}} = \int_V \Psi(\vec{r}) d^3r = \frac{\pi}{2} \sum_{n=-4}^4 A_n w_{x,n}(0) w_{y,n}(0) \int_{-\infty}^{\infty} \kappa(z) dz. \quad (\text{Eq. 93})$$

The function  $H_{klmn}(\tau)$  in Eq. 92 is defined by Eq. 94 and gives the probability that a particle is detected at time  $t=0$  in lobe  $m$  of detection volume  $k$  and after a time  $t=\tau$  in lobe  $n$  of detection volume  $l$ .



$$H_{klmn}(\tau) = \frac{A_m A_n}{2V_{\text{eff}}} w_{x,m}(0) w_{y,m}(0) w_{x,n}(0) w_{y,n}(0) h_{klmn}(\tau). \quad (\text{Eq. 94})$$

The function  $h_{klmn}(\tau)$  in Eq. 94 is given by Eq. 95:

$$h_{klmn}(\tau) = \sqrt{\frac{\pi}{4\Gamma\tau^\alpha}} \int_{-\infty}^{\infty} \int_{-\infty}^{\infty} \zeta_{klmn}(z_1, z_2, \tau) dz_1 dz_2. \quad (\text{Eq. 95})$$

The expression  $\zeta_{klmn}(z_1, z_2, \tau) dz_1 dz_2$  in Eq. 95 yields the probability for molecules to be detected at time  $t = 0$  in a  $dz_1$  thick cross-section through lobe  $m$  around the axial position  $z_1$  and after a time  $t = \tau$  in a  $dz_2$  thick cross-section through lobe  $n$  at position  $z_2$  and vice versa. The function  $\zeta_{klmn}(z_1, z_2, \tau)$  is given by Eq. 96

$$\zeta_{klmn}(z_1, z_2, \tau) = \frac{\kappa(z_1)\kappa(z_2)}{\sqrt{f_{mn,x}(z_1, z_2, \tau)}\sqrt{f_{mn,y}(z_1, z_2, \tau)}} \exp\left(-\frac{(z_2 - z_1)^2}{4\Gamma\tau^\alpha} - 2\frac{\Delta_{klmn}(z_1, z_2)}{f_{mn,y}(z_1, z_2, \tau)}\right). \quad (\text{Eq. 96})$$

Here, the functions  $\Delta_{klmn}(z_1, z_2)$  and  $f_{mn,i}(z_1, z_2, \tau)$  with  $i = x$  or  $i = y$  are given by Eq. 97 and 98, respectively:

$$\Delta_{klmn}(z_1, z_2) = y_m(z_1) - (d_{kl} + y_n(z_2)), \quad (\text{Eq. 97})$$

$$f_{mn,i}(z_1, z_2, \tau) = w_{i,m}^2(z_1) + w_{i,n}^2(z_2) + 8\Gamma\tau^\alpha. \quad (\text{Eq. 98})$$

Since the correlation model function given by Eq. 92 contains two integrals that can only be solved numerically, all auto- and cross-correlation curves were fitted by a least squares fitting routine of the GNU Scientific Library (GSL) (Galassi et al., 2003).

### IV.3.3 Measurement of the MDE structural parameters

The shape of experimental auto- and medium-distance cross-correlation curves depends strongly on the observed transport processes and the microscope's MDE function. In contrast, the particle transport process solely determines long-distance cross-correlation

curves' shape. For quantitative analysis of spatial FCCS measurements, our microscope's MDE function was determined with enhanced accuracy. For this purpose, the structural parameters for the previously derived double cone MDE model function (Eq. 92) were determined by a three-step approach: First, the structural parameters for the double cone geometry of the MDE were measured by three-dimensional imaging of fluorescent beads with a diameter of 0.1  $\mu\text{m}$ . Second, a self-developed highly sensitive method that is based on FCS was used to determine the amplitudes, widths and positions of the low-amplitude MDE side lobes. Third, fine-tuning of the measured MDE function's structural parameters was achieved by a computer routine that makes use of the fact that the MSD of diffusing fluorescent beads in aqueous solution grows linearly with time.

#### **IV.3.3.1 Double cone structural parameters**

Fluorescent beads with a diameter of 0.1  $\mu\text{m}$  were fixed on an object slide and used as fluorescent point light sources to determine the structural parameters that describe the double cone shaped MDE in axial direction. In the derived MDE model function (Eq. 92), the double cone geometry is determined by the cone angles in x- and y-direction that are related to the parameters  $k_x$  and  $k_y$  as well as by the curvatures of the cone envelope that are represented by parameters  $\alpha_x$  and  $\alpha_y$ . These parameters were measured by acquiring three-dimensional image stacks of fixed fluorescent beads (Figure 27).

As can be seen, the acquired image stack of a fluorescent bead was not symmetrical in axial direction due to deformation of the MDE at the object slide surface. Furthermore, a diffraction pattern similar to that in Figure 25a was observed. However, it was asymmetrical perpendicular to the illumination line. Probably, the line shaped profile of the fluorescence light beam was not exactly aligned to the center of the confocal slit.

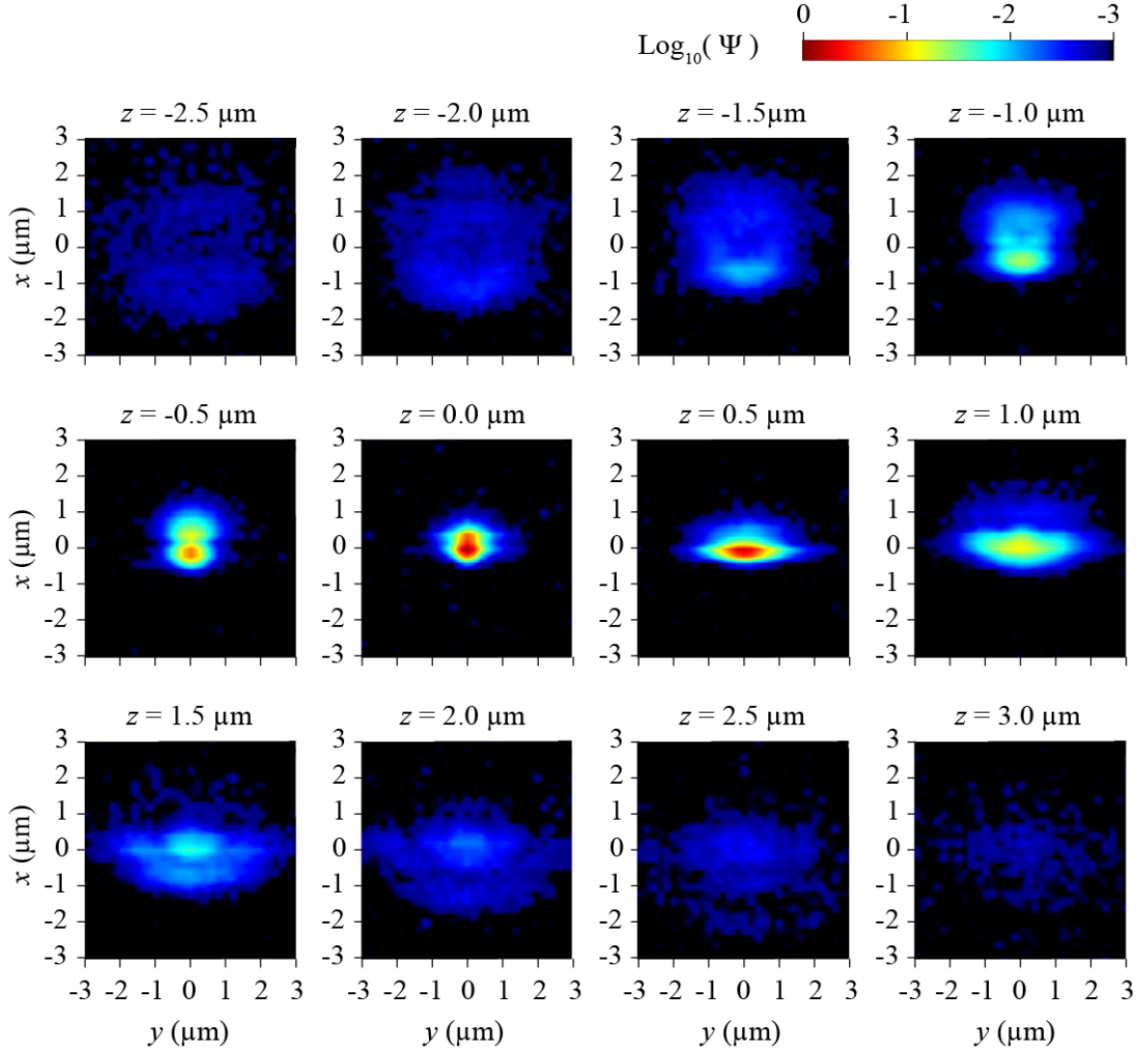


**Figure 27:** Images of a fluorescent bead's diffraction pattern at different axial position in the range from  $-2.5 \mu\text{m}$  to  $3.0 \mu\text{m}$  with a step size of  $0.5 \mu\text{m}$ . At position  $z = 0 \mu\text{m}$ , the fluorescent bead that was fixed on an object slide is in the microscope's focal plane. Above and below this plane, the images of the fluorescent bead were blurred and the width of the lateral intensity distribution increased. For  $z = 1.5 \mu\text{m}$ ,  $z = 2.0 \mu\text{m}$  and  $z = 2.5 \mu\text{m}$ , the first airy ring of the MDE function can be observed. Furthermore, the images above and below  $z = 0.0 \mu\text{m}$  were not symmetrical, i.e. they did not show the same intensity distribution. The mean intensity of the images decreased for  $z > 0.0 \mu\text{m}$  and  $z < 0.0 \mu\text{m}$  due to cropping effect of the confocal slit.

The lateral intensity distribution of each layer of the fluorescent bead image stacks was roughly approximated by a two-dimensional Gaussian function.

Because of the disturbing object slide surface on which the beads were fixed, a symmetrized axial cross-section ( $yz$ -plane) through the experimental MDE of a fluorescent bead and the fitted 3D-Gaussian and double cone model functions is shown in Figure 28.

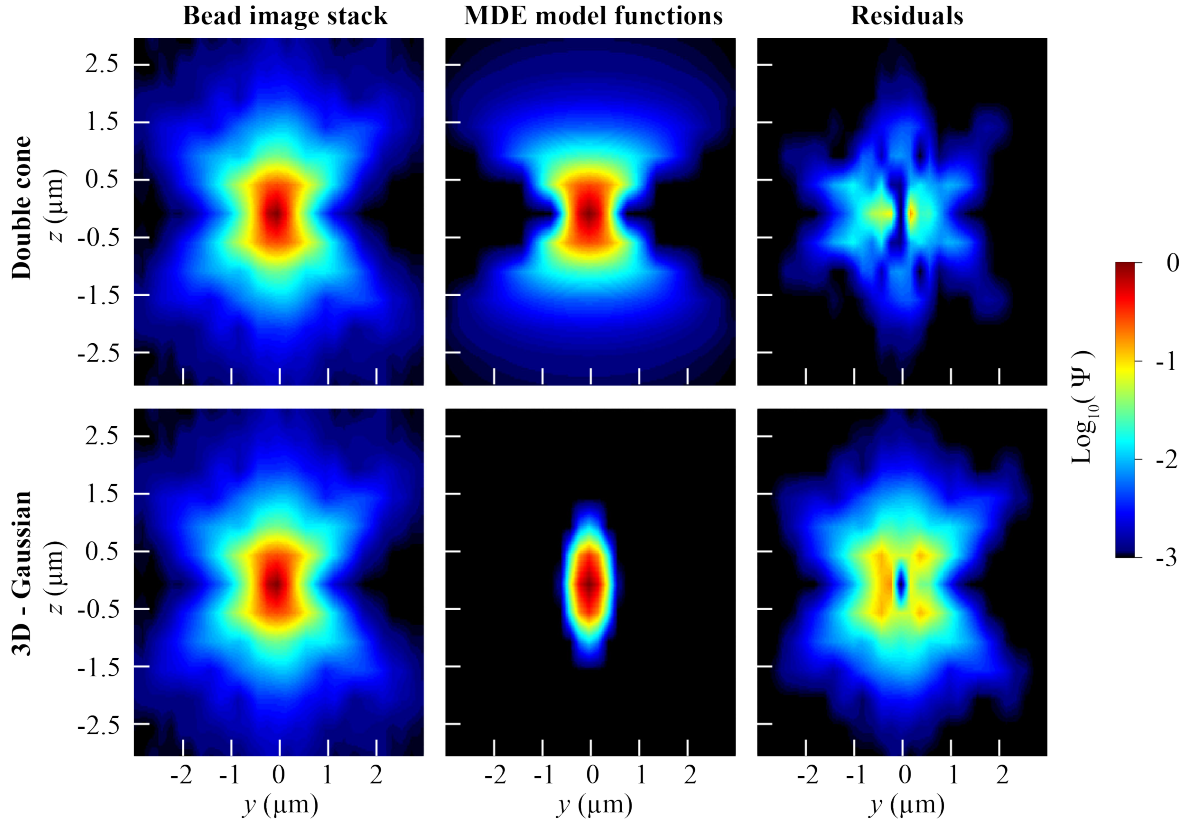


**Figure 28:** Axially symmetrical view of a cross-section through an acquired bead image stack, the fitted double cone and 3D-Gaussian model functions and the resulting residuals. Obviously, the double cone model describes the actual MDE of the microscope with a significantly higher accuracy.

The maximum intensity of the background corrected images expressed by  $\kappa(z)/\kappa(0)$  as well as the width  $w_x(z)$  and  $w_y(z)$  in  $x$ - and  $y$ -direction, respectively, of the 2D-Gaussian fits are plotted as a function of the axial position  $z$  in Figure 29. By fitting Eq. 89, Eq. 84 and Eq. 85 to these data, the double cone parameters  $k_x$ ,  $k_y$ ,  $\alpha_x$  and  $\alpha_y$  were determined.

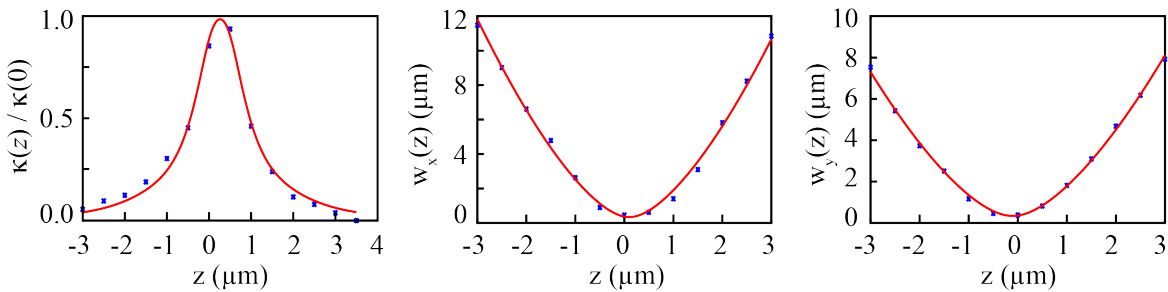


**Figure 29:** Maximum intensities  $\kappa(z)/\kappa(0)$  of the background corrected bead image stack layers (left panel) as well as the widths  $w_x(z)$  (middle panel) and  $w_y(z)$  (right panel) of the 2D-Gaussian approximation in  $x$ - and  $y$ -direction, respectively, as a function of the axial position  $z$ .

The integrated intensity of images at different axial positions was not equal due to the cropping effect of the confocal slit and the limited detection sensitivity. The determined structural parameters for the geometry of the line-confocal microscope's MDE function's double cone shape are summarized in Table 1.

<b>Cone curvature</b>	$\alpha_x$	$0.60 \pm 0.03$
	$\alpha_y$	$0.64 \pm 0.02$
<b>Cone angle parameters</b>	$k_x$	$4.3 \pm 0.4$
	$k_y$	$3.2 \pm 0.1$
<b>Rectangular aperture size (<math>\mu\text{m}</math>)</b>	$a$	$5.7 \pm 2.4$
	$b$	$0.6 \pm 0.1$

**Table 1:** Summary of experimentally determined structural parameters for the double cone shape of the line-confocal microscope's MDE function.

#### IV.3.3.2 MDE main lobe and side lobe structural parameters

For determining the amplitudes, widths and positions of the theoretically expected MDE side lobes, a highly sensitive approach was developed that is based on spatial FCCS measurements. When determining the MDE from image stacks of fluorescent beads, as described in the section above, the background signal consisting of camera readout noise and scattered light has to be accounted for. This is especially relevant for accurately measuring the low-amplitude MDE side lobes of line-confocal microscopes. In this thesis, an approach was developed that intrinsically separates the fluorescence signal from uncorrelated background noise. It allows for measuring the relevant MDE geometry for FCS model functions, since factors that affect imaging and correlation analysis differently are properly captured. The experimental setup of this approach is depicted in Figure 30. Fluorescent beads were immobilized with a sufficient low areal density for single particle experiments on an object slide. Single QDots, which are semiconductor nanocrystals, were used as fluctuating point light sources. Emission from single fluorescing QDots turns on and off intermittently with a characteristic timescale of about 0.5 s (Nirmal et al., 1996). Their emitted fluorescence signals were recorded until the QDots switched to a long-lasting non-fluorescent state. Fluorescence signals were analyzed by cross-correlating signals of spatially separated detection volumes. Each curve reflects the QDots' blinking spectrum (Figure 30b).

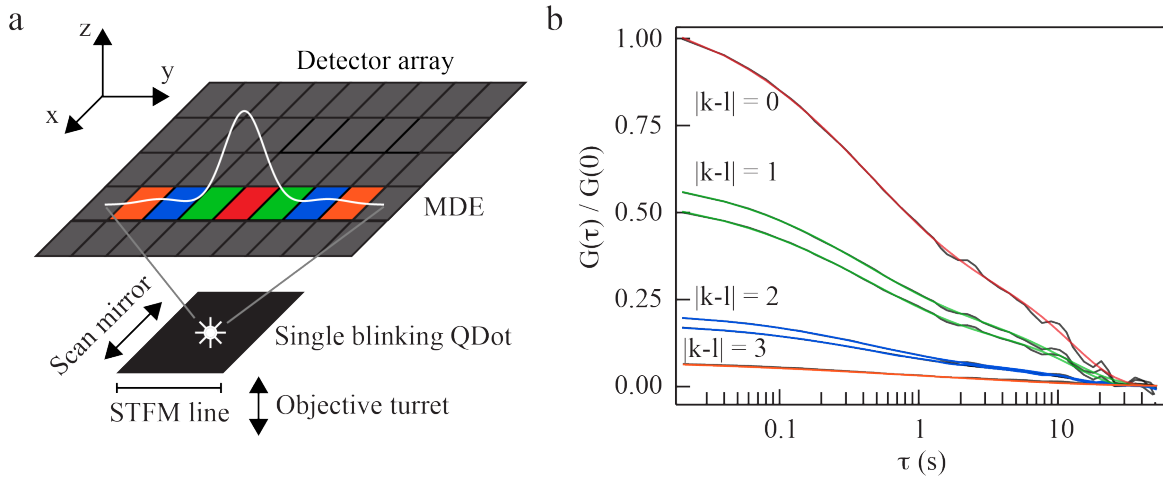


**Figure 30:** Determination of the structural parameters of the MDE's main and side lobes with high precision by spatial cross-correlation analysis. **(a)** Microscope setup for acquiring images and blink spectra of immobilized QDots. **(b)** Blink spectra of QDots for different cross-correlation distances  $d = |k-l|$ . To obtain the MDE's structural parameters in the focal plane ( $z = 0$ ) in direction of the illuminated line ( $x = 0$ ), we evaluated the fluorescence data as follows: The recorded signal  $S_n(t)$  of detection volume  $n$  is assumed to contain uncorrelated background noise  $N_n(t)$  and fluctuating fluorescence signal  $F_n(t)$  emitted by a single blinking QDot as given by Eq. 99.

To obtain the MDE's structural parameters in the focal plane, the fluorescence data were evaluated as follows: The recorded signal  $S_n(t)$  of detection volume  $n$  was assumed to contain uncorrelated background noise  $N_n(t)$  and fluctuating fluorescence signal  $F_n(t)$  emitted by a single blinking QDot as given by Eq. 99

$$S_n(t) = N_n(t) + F_n(t). \quad (\text{Eq. 99})$$

Accordingly, the corresponding relative signal fluctuations  $\delta S_n(t)$  consist of fluorescence fluctuations  $\delta F_n(t)$  and fluctuations due to noise  $\delta N_n(t)$  as given by Eq. 100

$$\delta S_n(t) = \delta N_n(t) + \delta F_n(t). \quad (\text{Eq. 100})$$

The noise fluctuations  $\delta N_n(t)$  are temporarily uncorrelated, whereas the fluorescence fluctuations  $\delta F_n(t)$  are correlated according to QDot blinking dynamics. Thus, background noise  $\delta N_n(t)$  was removed by correlation of the relative signal fluctuations  $\delta S_n(t)$  as shown in Eq. 101:

$$\begin{aligned}\langle \delta S(t) \delta S(t + \tau) \rangle &= \langle \delta F(t) \delta F(t + \tau) \rangle + \langle \delta F(t) \delta N(t + \tau) \rangle + \langle \delta N(t) \delta F(t + \tau) \rangle + \langle \delta N(t) \delta N(t + \tau) \rangle \\ &= \langle \delta F(t) \delta F(t + \tau) \rangle\end{aligned}\quad (\text{Eq. 101})$$

Fluorescence signals  $F_n = \alpha_n F_0$  recorded by each detector pixel  $n$  were proportional to the signal emitted by a single QDot with a proportionality coefficient  $\alpha_n$ , which was used to determine the MDE at the corresponding distance  $d_n$  from the Qdot position. The intensity parameter  $\alpha_n$  was extracted by cross-correlation of relative signal fluctuations of spatially separated detection volumes according to Eq. 102.

$$\langle \delta S_0(t) \delta S_i(t + \tau) \rangle = \alpha_i \langle \delta S_0(t) \delta S_0(t + \tau) \rangle \Rightarrow \alpha_i = \frac{\langle \delta S_0(t) \delta S_i(t + \tau) \rangle}{\langle \delta S_0(t) \delta S_0(t + \tau) \rangle} = \frac{\langle \delta F_0(t) \delta F_i(t + \tau) \rangle}{\langle \delta F_0(t) \delta F_0(t + \tau) \rangle}\quad (\text{Eq. 102})$$

The correlation analysis eliminated uncorrelated background noise  $N_n(t)$  and thus provided a robust approach for measuring the MDE's main lobe. Significant MDE amplitudes were measured even for distances larger than 2  $\mu\text{m}$  but positions and widths of the side lobes were difficult to resolve (Figure 31). For determining the side lobe structural parameters and positions, a theoretical model function (Dusch et al., 2007), which is valid near the focal plane for  $x = z = 0$ , was fitted to the measured MDE data.

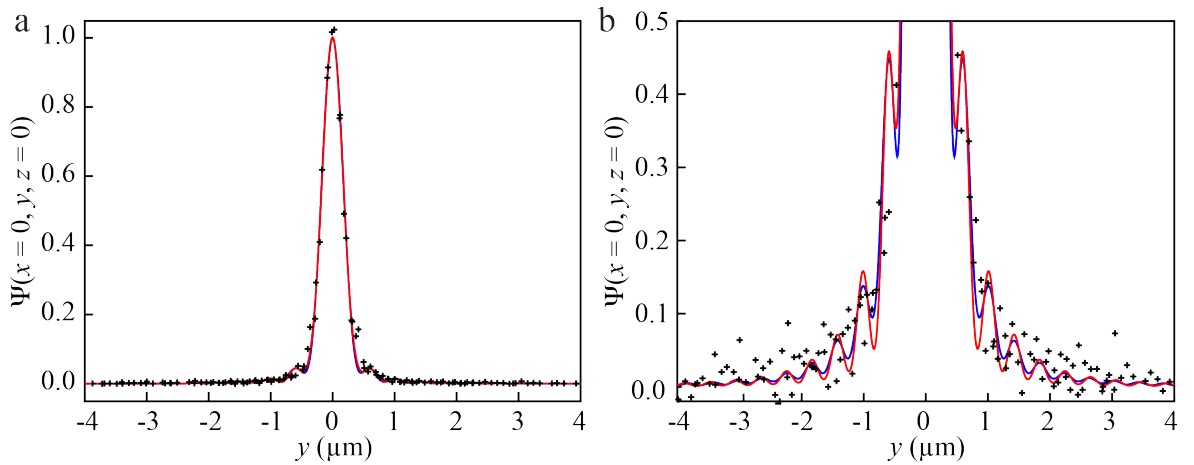


**Figure 31:** (a) Measured MDE function in the focal plane in direction of the illumination line (y-direction). MDE data (black crosses) from the spatial cross-correlation analysis were fitted with Eq. 81 (red line). (b) Each lobe of the model function (red line) was approximated by a Gaussian function (blue line).

Furthermore, MDE side lobes of the derived model function were approximated in the focal plane by asymmetric two-dimensional Gaussian functions (Figure 25). The structural parameters for the MDE function's main lobe and side lobes are summarized in Table 2.

Lobe number	$n$	0	1	2	3	4
Amplitudes	$A_n$	1.000	0.044	0.016	0.007	0.002
Width	$w_{x,n}$ ( $\mu\text{m}$ )	0.19	1.25 $w_{x,0}(0)$			
	$w_{y,n}$ ( $\mu\text{m}$ )	0.32	0.53 $w_{y,0}(0)$			
Position	$\delta_n(0)$ ( $\mu\text{m}$ )	0	0.58	$\delta_l(0) + 0.41 (n-1)$		

**Table 2:** Summary of the determined structural parameters of the line-confocal microscope's main lobe and side lobes.

#### IV.3.3.3 Fine-tuning of the measured MDE structural parameter set

The geometry of the MDE main and side double cones in  $yz$ -direction, given by cone angle, curvature of the cone and decrease of the mean intensity in axial direction, strongly influenced the shape of spatial cross-correlation curves due to spatially overlapping neighboring detection volumes. To enhance the accuracy of the cross-correlation model functions, the previously measured MDE structural parameter set was further improved by a computer optimization routine (Figure 32). The optimization was based on the invariance of the measured diffusion coefficients and concentrations with respect to the correlation distance for photo-stable fluorescent particles in pure distilled water. An additional condition was that experimental correlation curves are adequately described by the model functions with good fit quality. Thus, cross-correlation curves were fitted for 0  $\mu\text{m}$ , 1  $\mu\text{m}$ , 2  $\mu\text{m}$ , 3  $\mu\text{m}$  and 4  $\mu\text{m}$  correlation distance of QDots diffusing in aqueous solution with the improved double cone model function and checked for the scale-invariance of the resulting diffusion coefficients and concentrations. The same procedure was repeated for different MDE structural parameter sets. Finally, the MDE structural parameter set was selected for which the experimental correlation curves were well described by the model functions and additionally the best scale-invariance of the fit results was observed.



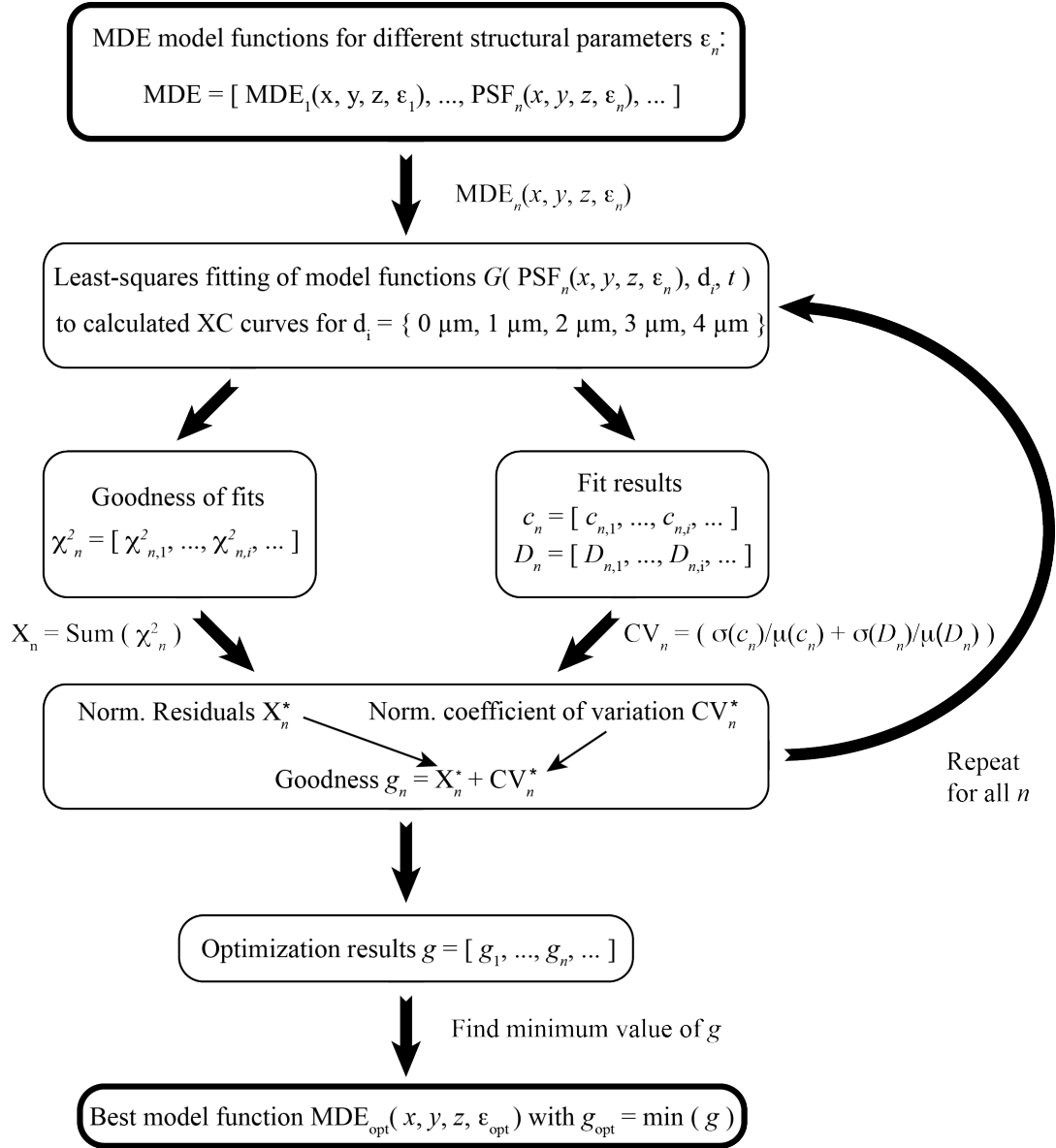


**Figure 32:** MDE optimization according to reference measurements of QDots in aqueous solution. The correlation model functions  $G( \text{MDE}(x, y, z, \epsilon_n), d_i, \tau )$  for different MDE geometries were defined by structural parameters  $\epsilon_n$  that matched the experimentally determined MDE structural parameters. The correlation model functions  $G( \text{MDE}(x, y, z, \epsilon_n), d_i, \tau )$  were fitted to experimental correlation curves for different correlation distances  $d_i$ . In the next step, the goodness of the correlation function fits  $X_n$  and the coefficients of variation  $\text{CV}_n$  of the fit results were combined into a global fit quality parameter  $g_n$ . This procedure was repeated for each structural parameter combination  $\epsilon_n$ . The MDE model function  $\text{MDE}_{\text{opt}}(x, y, z, \epsilon_{\text{opt}})$  yielding the best value of  $g_n$  was selected for least squares fitting of experimental spatial FCCS curves.

#### IV.4 Mobility and diffusion barrier mapping by 1D-FCS

Protein transport in the heterogeneous and crowded environment of living cells was measured by mapping the mobility of inert fluorescent proteins by 1D-FCS with a line-confocal microscope. GFP monomers (GFP<sub>1</sub>), trimers (GFP<sub>3</sub>) and pentamers (GFP<sub>5</sub>) were used as inert tracers to probe the impact of the intracellular structure on protein transport. For this purpose, the mobility of these proteins was measured in the nucleus and cytoplasm of human U2OS cells. As a reference measurement, the mobility of GFP<sub>1</sub> was additionally determined in homogeneous aqueous solutions. Representative fluorescence microscopy images of GFP<sub>1</sub>, GFP<sub>3</sub> and GFP<sub>5</sub> expressing U2OS cells are shown in Figure 33. For increasing size of the fluorescent proteins, they are less efficiently transported from their place of production in the cytoplasm into the nucleus, as can be seen by the distribution of the fluorescence intensities in Figure 33.

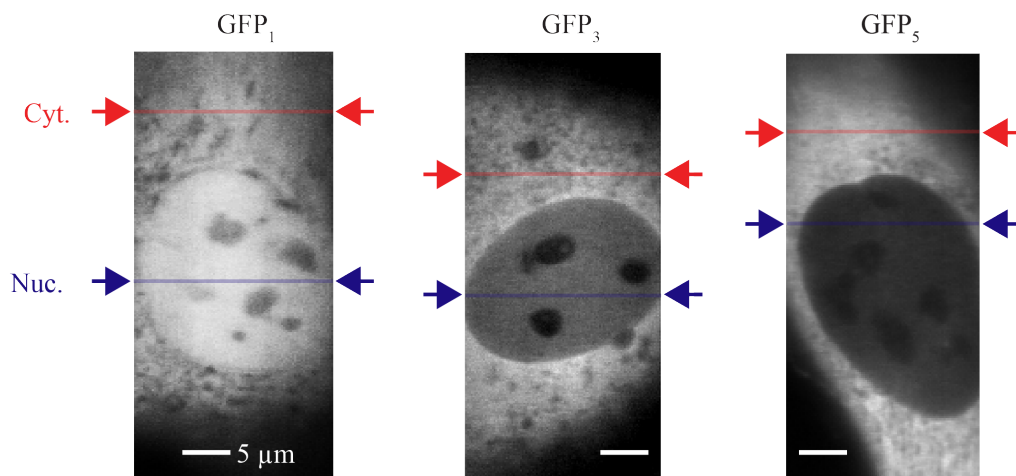


**Figure 33:** Fluorescence microscopy images of GFP monomers (GFP<sub>1</sub>), trimers (GFP<sub>3</sub>) and pentamers (GFP<sub>5</sub>) in cytoplasm and nucleus of living human U2OS cells. GFP<sub>1</sub> molecules were equally distributed between cytoplasm and nucleus, whereas for increasing molecule size the cytoplasm appeared brighter than the nucleus, i.e. the concentration of fluorophores was lower in the nucleus.

Auto- and cross-correlation curves were acquired at about 50 positions that were equally distributed along a line of 10  $\mu\text{m}$  in the cells. The arrows in Figure 33 indicate the positions of the 1D-FCS measurements. Homogeneously appearing regions in the cytoplasm and nucleus were chosen for acquisition of fluorescence signal with the line-confocal microscope.

To map the spatial arrangement of regions with fast and slow protein transport, auto- and cross-correlation carpets for 0.6  $\mu\text{m}$  and 1.2  $\mu\text{m}$  separation distance between detection volumes were plotted for measurements in aqueous solution, in the nucleus and the cytoplasm, as shown in Figure 34.

Each column of the carpets represents a correlation curve at the accordant position in the cell. In the cytoplasm and particularly in the nucleus, the protein mobility was significantly reduced at a subset of positions. These indicate the presence of diffusion barriers created by impermeable regions that hinder molecular transport (Digman and Gratton, 2009; Ellgaard and Helenius, 2001). At the same time, the correlation carpets revealed large domains with high protein mobility in both cytosol and nucleus representing extended accessible subcompartments that are separated by transport barriers. Furthermore, the heterogeneous amplitude values and diffusion times in the correlation carpets of GFP<sub>1</sub> in the nucleus indicate an increased heterogeneity of chromatin on the molecular scale compared to the cytoplasmic environment. This is consistent with previous studies (Dross et al., 2009; Moeendarbary et al., 2013; Pack et al., 2006). To quantify the spatial variance of the protein mobility, all correlation curves were fitted by a correlation model function for anomalous diffusion (Eq. 92). The unit-free retardation of the protein mobility  $R(y)$  was defined as the ratio of the mean value of the auto-correlation diffusion coefficient ensemble  $\langle D_{AC} \rangle$  to the individual diffusion coefficient  $D(y)$  at position  $y$  by

$$R(y) = \frac{\langle D_{AC} \rangle}{D(y)}. \quad (\text{Eq. 103})$$

Accordingly, lower mobility is expressed by higher retardation values. Below the carpets in Figure 34, the fold increases  $\Delta R(y)$  of retardations  $R(y)$  are plotted to visualize clusters of high protein mobility positions and diffusion barriers. Positions with significantly slower protein transport are highlighted as red tips on the retardation bars. Histograms of the measured retardation values are plotted in Figure 35. In aqueous solution, the mean diffusion coefficient of GFP<sub>1</sub> was independent of the translocation distance, which is characteristic for normal diffusion that is not hindered by diffusion barriers. However, the standard deviation increased due to decreasing signal-to-noise ratios for larger separation distances, as can be observed in Figure 35 and Table 3.

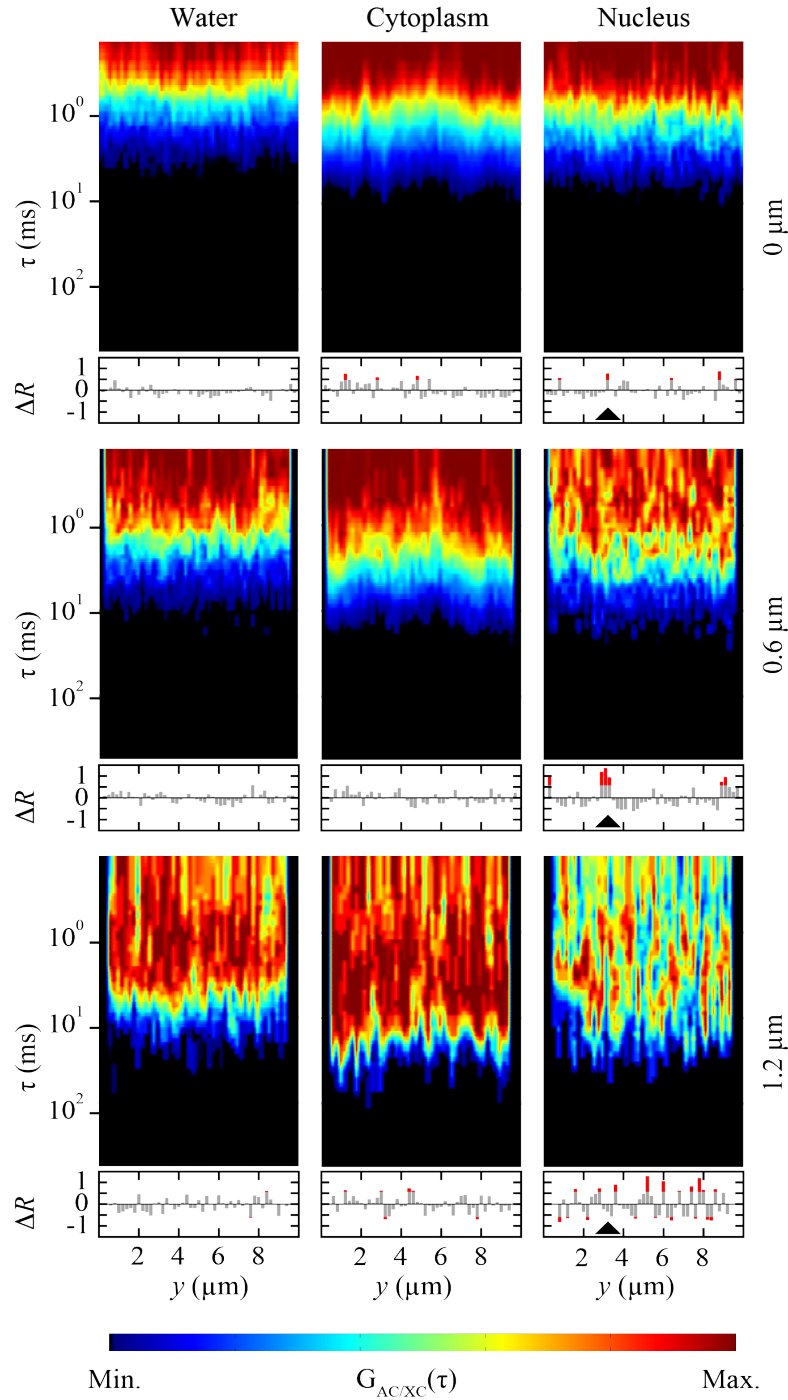


**Figure 34:** Auto- and cross-correlation carpets for 0.0  $\mu\text{m}$ , 0.6  $\mu\text{m}$  and 1.2  $\mu\text{m}$  separation distance of GFP<sub>1</sub> molecules in aqueous solution, the cytoplasm and nucleus of living human U2OS cells. Regions with diffusion barriers can be identified from the fold increase of the retardation  $\Delta R$  plotted below the carpets. Negative  $\Delta R$  values correspond to an increase of the diffusion coefficient. An example for a diffusion barrier that was most pronounced for the 0.6  $\mu\text{m}$  separation distance is marked with a black arrow.

In contrast to the 1D-FCS measurement results of GFP<sub>1</sub> in aqueous solution, the mean diffusion coefficients of GFP<sub>1</sub>, GFP<sub>3</sub> and GFP<sub>5</sub> in cytoplasm and nucleus decreased with

increasing separation distance due to hindered diffusion in the heterogeneous cellular environment (Figure 35 and Table 3).

Thus, in cells protein transport by diffusion processes was significantly slowed down in a length scale-dependent manner and deviated significantly from normal diffusion in aqueous solution. Interestingly, the mobility histograms for larger translocation distances were broader than the reference histograms and showed an increasing fraction of proteins that were significantly slowed down compared to their mobility measured on small scales. Mobility histograms of measurements in the nucleus appeared more asymmetric than those of measurements in the cytoplasm.

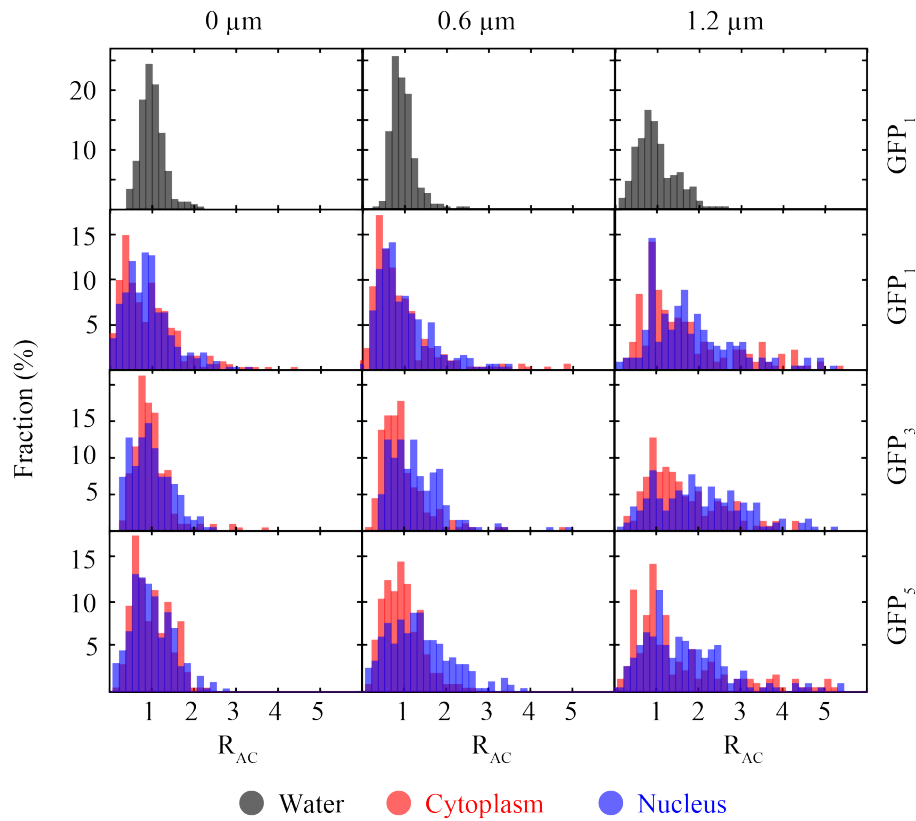


**Figure 35:** Retardation coefficient  $R_{AC} = \langle D_{AC} \rangle / D$  histograms, which corresponds to the translocation time of GFP monomer ( $GFP_1$ ), trimer ( $GFP_3$ ) and pentamer ( $GFP_5$ ) molecules relative to the average value obtained from the autocorrelation analysis. Measurements were conducted at about 50 positions equally distributed on a 10  $\mu m$  long line for separation distances of 0  $\mu m$  (auto-correlation), 0.6  $\mu m$  and 1.2  $\mu m$  (spatial cross-correlation) in aqueous solution, the nucleus and the cytoplasm.

This suggests that the cytoplasm appeared more homogeneously and the nucleoplasm more heterogeneously to diffusing proteins. Altogether, the cellular interior appeared

heterogeneous (Table 3) and some particles became at least transiently trapped. The mean value  $\mu$ , standard deviation  $\sigma$  and skewness  $\gamma$  of the ensembles of measured GFP<sub>1</sub>, GFP<sub>3</sub> and GFP<sub>5</sub> diffusion coefficients are summarized in Table 3.

		0.0 $\mu\text{m}$			0.6 $\mu\text{m}$			1.2 $\mu\text{m}$		
		$\mu$	$\sigma$	$\gamma$	$\mu$	$\sigma$	$\gamma$	$\mu$	$\sigma$	$\gamma$
<b>GFP<sub>1</sub></b>	<b>PBS</b>	1.0	0.3	1.0	1.0	0.3	1.7	1.0	0.6	0.8
	<b>Cyt.</b>	1.0	0.7	1.5	1.0	0.8	2.5	1.7	1.1	1.2
	<b>Nuc.</b>	1.0	0.6	1.1	1.1	0.7	1.4	1.9	1.0	1.1
<b>GFP<sub>3</sub></b>	<b>Cyt.</b>	1.0	0.5	2.4	1.0	0.6	2.5	1.6	0.9	0.9
	<b>Nuc.</b>	1.0	0.5	0.6	1.3	0.7	1.9	2.0	1.0	0.6
<b>GFP<sub>5</sub></b>	<b>Cyt.</b>	1.0	0.4	0.5	1.0	0.5	0.8	1.6	1.2	1.3
	<b>Nuc.</b>	1.0	0.5	0.7	1.4	0.8	0.7	1.7	1.0	1.3

**Table 3:** Summary of statistical parameters of mobility histograms for GFP<sub>1</sub>, GFP<sub>3</sub> and GFP<sub>5</sub>. Measurements were conducted in aqueous solution (phosphate buffered saline, PBS), cytoplasm (Cyt.), and nucleus (Nuc.). Fitting of correlation functions for distances of 0.0  $\mu\text{m}$ , 0.6  $\mu\text{m}$  as well as 1.2  $\mu\text{m}$  yielded histograms with mean value  $\mu$ , standard deviation  $\sigma$  and skewness  $\gamma$  as indicated. Each histogram contains at least  $N > 200$  values.

To quantify the amount of trapped GFP monomers and multimers in dense structures of U2OS cells' cytoplasm and nucleus, complementary fluorescence recovery after photobleaching (FRAP) measurements were conducted. As a reference monomeric red fluorescent protein (RFP<sub>1</sub>, equivalent to GFP<sub>1</sub> with a hydrodynamic radius ( $r_H \approx 2.8$  nm)) was measured simultaneously with GFP<sub>3</sub> ( $r_H \approx 5.5$  nm) or GFP<sub>5</sub> ( $r_H \approx 7.9$  nm).

A model function that was derived for diffusion of particles without binding interactions was used for the analysis of the FRAP experiments (Braga et al., 2004). It was introduced in the theory section of this thesis. Since immobile fluorescent molecules were observed as a “step” in the intensity radial profiles at a radial distance  $w_b = 1.3$   $\mu\text{m}$  from the circular bleached region center in the first post-bleach image frame (Figure 36), the model function given by Eq. 45 was modified accordingly. A term with a Heaviside function that accounts for a trapped fraction  $f_{\text{trap}}(100 \text{ ms})$  of molecules on the 100 ms time-scale (corresponding to the frame acquisition time) was added:

$$F(r) = \exp\left(-K_M \exp\left(-2 \frac{r^2}{w_M^2}\right)\right) - f_{\text{trap}}(1 - \Theta(r - w_b)). \quad \text{Eq. 104}$$

By least squares fitting of Eq. 104 to the measured radial profiles the width  $w_M$  of the bleached region and the trapped molecule fraction  $f_{\text{trap}}(100 \text{ ms})$  was determined as shown in Table 4. The amount of RFP<sub>1</sub> that was trapped for at least 100 ms in the nucleus was negligible (Figure 36 and Table 4). In contrast, significant fractions of about 6 - 8% trapped GFP<sub>3</sub> and GFP<sub>5</sub> were present.

The amounts of molecules that are trapped on the minute time scale was quantified by conventional FRAP analysis of the average fluorescence recovery as a function of time. For this purpose, the model function given by Eq. 105 was fitted to the recovery curves (Figure 36) of the averaged fluorescence intensity with the previously determined radial profile widths  $w_M$ :

$$F(t) = \frac{1 - f_{\text{trap}}}{2} \left( \frac{w_M^2}{w_b^2} \left[ \sum_{n=1}^{\infty} \frac{(-K_M)^n}{n!n} \left( 1 - \exp\left(-2 \frac{w_b^2}{w_M^2} \frac{n}{1 + 2nt/\tau_D}\right) \right) \right] + 2 \right). \quad \text{Eq. 105}$$

The obtained fit results were the bleach depth  $K_M$ , the trapped fraction  $f_{\text{trap}}(1 \text{ min})$  on the minute time-scale and the diffusion coefficient  $D = w_M^2/(4\tau_D)$ .

Hardly any trapped GFP<sub>5</sub> molecules were detected in the cytoplasm, while the immobile fraction of GFP<sub>5</sub> in the nucleus persisted longer than 1 min. The results obtained by FRAP suggest that the throat size of small pores in the chromatin structure that confine the diffusion of GFP<sub>5</sub> in the nucleus was comparable to the effective hydrodynamic diameter of GFP<sub>5</sub> which is about 15 nm. However, in the cytoplasm correspondingly dense regions, probably created by the cytoskeleton network, appeared to open up faster so that trapping was detected there only for shorter time at about 100 ms.

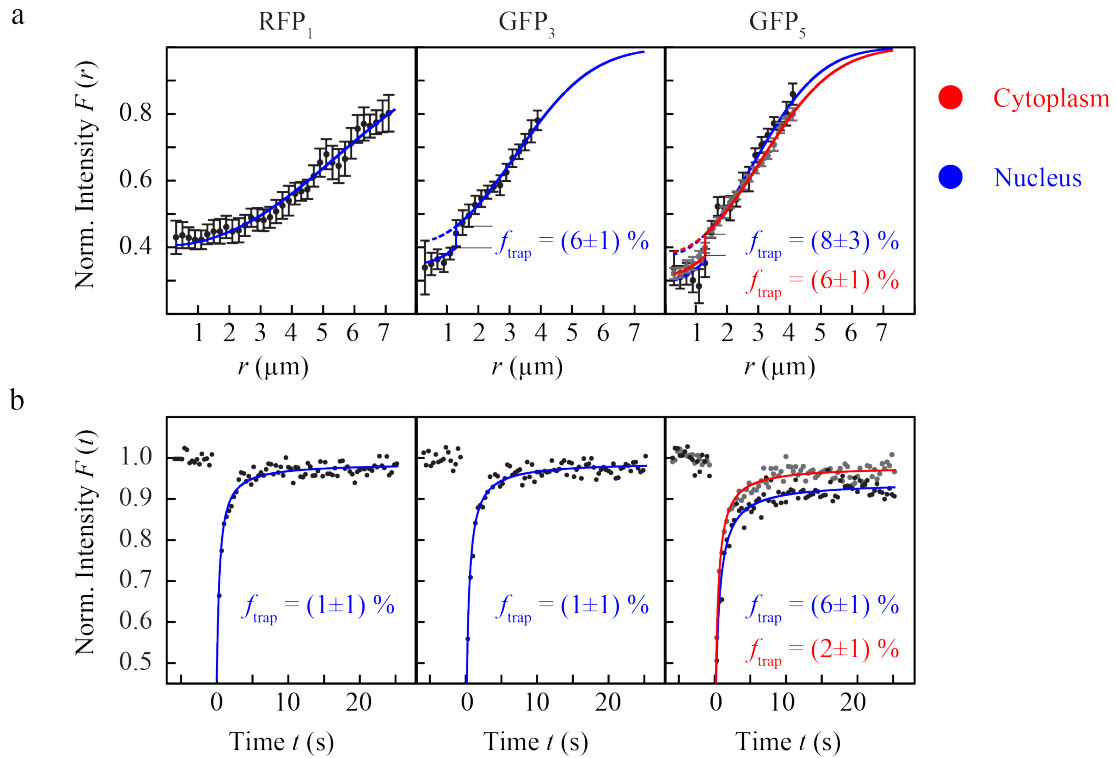


**Figure 36:** FRAP measurements of RFP<sub>1</sub>, GFP<sub>3</sub> and GFP<sub>5</sub>. **(a)** The fraction of trapped protein  $f_{\text{trap}}$  was obtained from the analysis of the post-bleach radial intensity profile after 100 ms. **(b)** The average recovery curve on the minute time scale. Apparent diffusion coefficients were determined by least squares fitting from the average recovery curves.

All results that were obtained by least squares fitting of the radial profiles of the first post-bleach image frames by Eq. 104 and of the recovery curves of the average intensity by Eq. 105 are summarized in Table 4.

Information about the fraction of immobilized fluorescent proteins could be determined 100 ms and 1 min after the bleach process. The diffusion coefficients of RFP<sub>1</sub>, GFP<sub>3</sub> and GFP<sub>5</sub> determined by FRAP using a bleach spot with a radius of 1.3  $\mu\text{m}$  were in good agreement with the values obtained here by spatial FCCS measurements for a separation distance of detection volumes of 1.2  $\mu\text{m}$  and with the values obtained recently by pixel-wise photobleaching profile evolution analysis (3PEA) (Erdel and Rippe, 2012) on the same length scale (Table 9). Therefore, mobility measurements on multiple time and length scales by spatial FCCS measurements allow for comparing results of mobility measurements in living cells that were obtained by techniques operating on different time and length scale ranges.



	Post-bleach radial profile			Average recovery curve	
	$K_M$	$w_M$ ( $\mu\text{m}$ )	$f_{\text{trap}}^a$ (%)	$D_{\text{app}}$ ( $\mu\text{m}^2/\text{s}$ )	$f_{\text{trap}}^b$ (%)
<b>RFP<sub>1</sub>, nuc.</b>	0.90	8.8	0	$31 \pm 7$	$1 \pm 1$
<b>GFP<sub>3</sub>, nuc.</b>	$0.88 \pm 0.02$	$5.0 \pm 0.1$	$6 \pm 1$	$15 \pm 4$	$1 \pm 1$
<b>GFP<sub>5</sub>, nuc.</b>	$0.98 \pm 0.06$	$4.4 \pm 0.2$	$8 \pm 3$	$10 \pm 1$	$6 \pm 1$
<b>GFP<sub>5</sub>, cyt.</b>	$0.83 \pm 0.01$	$4.9 \pm 0.01$	$6 \pm 1$	$14 \pm 4$	$2 \pm 1$

**Table 4:** Results of FRAP measurements according to the analysis of the radial intensity profile 100 ms after the bleach (left) as well as the average recovery curve (right). Values for RFP<sub>1</sub>, GFP<sub>3</sub> and GFP<sub>5</sub> in the cytoplasm and the nucleus of U2OS cells are shown. At least 10 measurements were conducted for each protein and cellular compartment. <sup>a</sup> Immobile fraction due to trapping by the cellular structure observed 100 ms after the bleach process. <sup>b</sup> Immobile fraction observed 1 min after the bleach process.

## IV.5 Mobility measurements on multiple time and length scales

### IV.5.1 Inert GFP monomers and multimers in unperturbed living cells

In the crowded interior of living cells, diffusion of proteins is hindered by collisions with cellular obstacles. These collisions make the diffusion process anomalous, i.e. the MSD is a non-linear function of time (Wachsmuth et al., 2000; Weiss et al., 2004; Weiss et al., 2003). The scale-dependent diffusion laws of inert GFP<sub>1</sub>, GFP<sub>3</sub> and GFP<sub>5</sub> molecules were measured by spatial FCCS with a line-confocal microscope in the cytoplasm and nucleus of human U2OS cells. For this purpose, the illumination and detection volume of the line-confocal microscope was positioned in regions in the cell that appeared homogeneous in confocal fluorescence microscopy images. From the fluorescence signals acquired at about 50 positions along a 10  $\mu\text{m}$  long line, auto- and cross-correlation curves were calculated and ensembles of correlation curves for equal separation distances were averaged. The average curves of the ensembles were fitted by a model function (Eq. 92) that describes anomalous diffusion of particles in fractal media. Representative average correlation curves for separation distances of 0.0  $\mu\text{m}$ , 0.6  $\mu\text{m}$  and 3.0  $\mu\text{m}$  that were acquired in cytoplasm and nucleus as well as the fitted model functions are depicted in Figure 37. Peaks appeared in cross-correlation curves at the time most proteins needed to diffuse the distance between the detection volumes of the correlated fluorescence signals. For increasing molecular weights of the proteins and increasing separation distances, these peaks shifted to longer time lags.

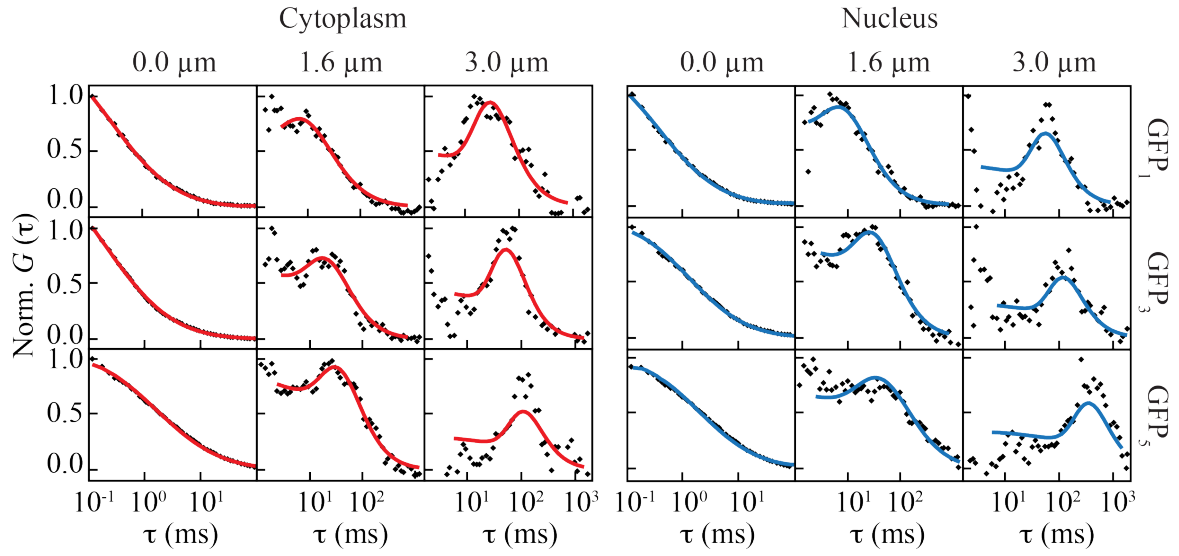


**Figure 37:** Representative average auto- (0.0  $\mu\text{m}$ ) and cross-correlation curves (1.6  $\mu\text{m}$  and 3.0  $\mu\text{m}$ ) acquired for GFP<sub>1</sub>, GFP<sub>3</sub> and GFP<sub>5</sub> in the cytoplasm and nucleus of living U2OS cells. The fitted model functions are depicted as red and blue lines for mobility measurements in cytoplasm and nucleus, respectively. Cross-correlation curves showed a peak at the time most molecules needed for diffusing the corresponding distance. This peak shifted for increasing molecular weight and separation distance to larger time lags.

A model for correlation of fluorescence signals due to anomalous diffusion that is given by Eq. 92 was fitted to the average curves of the correlation curve ensembles. The fit results of the anomalous diffusion model, i.e. transport coefficient  $\Gamma$  and anomaly parameter  $\alpha$ , were only valid on the length scale (or the corresponding time scale) of the spatial cross-correlation measurement. However, they could be used to calculate an effective diffusion time for the distance covered between two detection events. The effective distances molecules diffuse if they are detected in both detection volumes  $\Psi_k$  and  $\Psi_l$ , depend on the line-confocal microscope's MDE volume geometry and the distance between the centers of the detection volumes. For large separation distances, the actual size and geometry of the volumes becomes negligible. The effective diffusion distance between two detection volumes is the typical length scale of the corresponding spatial FCCS analysis. It was calculated as the mean distance between two points in different MDE volumes weighted with the corresponding detection efficiencies at these positions given by the microscope's MDE function. The effective diffusion distance is larger than the distance  $\Delta$  between the MDE volumes' centers due to the spatial extension of the detection volumes. Thus, the mean effective diffusion distance  $\langle d_{kl} \rangle$  was calculated by

$$\langle d_{kl} \rangle = \frac{\int \psi_{0,k}(x_1, y_1, 0) |\vec{r}_2 - \vec{r}_1|_{z=0} \psi_{0,l}(x_2, y_2, 0) dx_1 dy_1 dx_2 dy_2}{\int \psi_{0,k}(x_1, y_1, 0) dx_1 dy_1 \int \psi_{0,l}(x_2, y_2, 0) dx_2 dy_2}. \quad (\text{Eq. 106})$$

For simplicity, only the main lobes of the MDE functions were considered and low amplitude side lobes were neglected.

The effective diffusion time  $\langle t_{kl} \rangle$  for the translocation of molecules between the line-confocal microscope's detection volumes  $k$  and  $l$  were calculated based on the resulting fit parameters, i.e. transport coefficient  $\Gamma$  and anomaly parameter  $\alpha$ . It is given by

$$\langle t_{kl} \rangle = \left( \frac{\langle d_{kl} \rangle^2}{6\Gamma} \right)^{1/\alpha}. \quad (\text{Eq. 107})$$

The effective diffusion time  $\langle t_{kl} \rangle$  is a good measure for characterizing the scaling behavior of transport processes, since it is rather independent of the specific propagator of the transport process used for least squares fitting of the acquired correlation curves. This is due to the fact that the maximum amplitude of the correlation curve determines the effective diffusion time, which is thus robustly obtained even without fitting. With this information on multiple time and length scales, the MSD of the proteins could be reconstructed as a function of time by plotting the squared effective diffusion distance  $\langle d_{kl} \rangle^2$  as a function of the effective diffusion time  $\langle t_{kl} \rangle$  (Figure 38).

An instructive illustration for studying the scaling of diffusion processes in living cells is a double-logarithmic representation of the time-dependent apparent diffusion coefficient  $D_{\text{app}}$  that is defined by

$$D_{\text{app}} = \frac{\langle d_{kl} \rangle^2}{6\langle t_{kl} \rangle}. \quad (\text{Eq. 108})$$

Figure 38 shows the calculated time-dependent diffusion coefficients of GFP<sub>1</sub>, GFP<sub>3</sub> and GFP<sub>5</sub> molecules in the cytoplasm and nucleus of human U2OS cells.

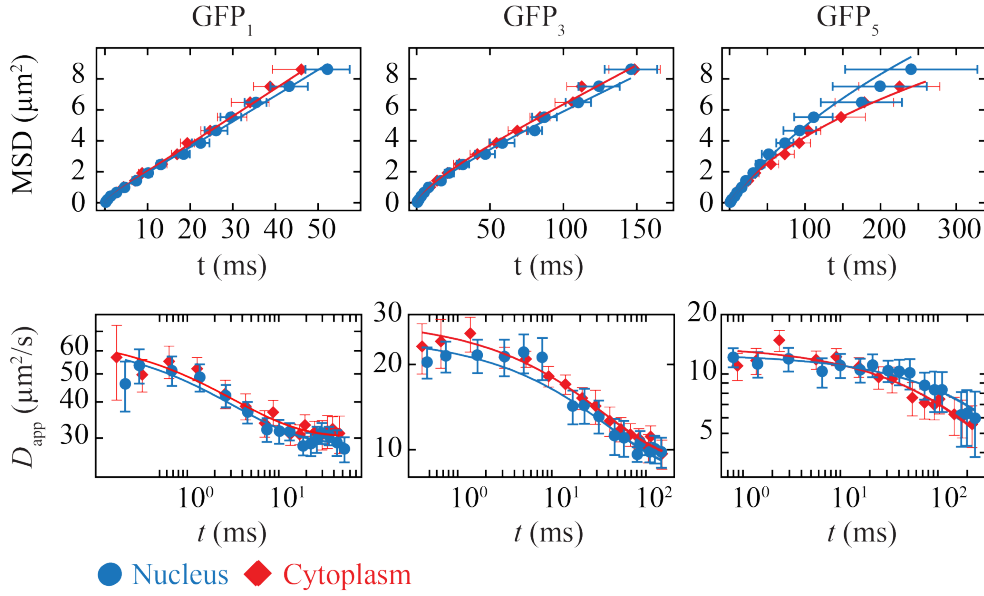


Figure 38: MSD as a function of time for diffusion of GFP<sub>1</sub>, GFP<sub>3</sub> and GFP<sub>5</sub> in the cytoplasm (red diamonds) and nucleus (blue circles) of living human cells (upper row). The fitted model function for diffusion in a porous environment is shown as red (cytoplasm) and blue (nucleus) lines. The time-dependence of the apparent diffusion coefficient  $D_{\text{app}}$  is shown in the row below. Data points followed a sigmoidal shape in a double-logarithmic representation as observed for diffusion in porous media.

By assuming that the trajectories of diffusing proteins in living cells have fractal geometries, the slope of the apparent diffusion coefficient function  $D_{\text{app}}(t)$  at time  $t$  is given by  $(\alpha - 1)$  in this representation, according to the relation

$$\log(D_{\text{app}}(t)) = (\alpha - 1)\log(t) + \log(\Gamma). \quad (\text{Eq. 109})$$

However, the time-dependent apparent diffusion coefficients of GFP<sub>1</sub>, GFP<sub>3</sub> and GFP<sub>5</sub> acquired by spatial FCCS in living cannot be described by fix values for transport coefficient  $\Gamma$  and anomaly parameter  $\alpha$ . Rather, a plateau phase of  $D_{\text{app}}(t)$  on a microscopic time and length scale that represents normal diffusion ( $\alpha = 1$ ) is followed by an anomalous diffusion regime ( $\alpha < 1$ ) that cannot be described by a single anomaly parameter  $\alpha$ . Finally,  $D_{\text{app}}(t)$  reaches a second plateau phase of normal diffusion with a reduced diffusion coefficient on a macroscopic time and length scale. The crossover time from the fast normal diffusion regime on microscopic scales to the slow normal diffusion regime on macroscopic scales is characteristic for each  $D_{\text{app}}(t)$  curve. For inert tracer

molecules, the crossover regime contains information about interactions with the cellular structure. For a quantitative description of the acquired multi-scale mobility data, a simple model function for diffusion in porous media was adapted (Loskutov and Sevriugin, 2013). It was derived to describe the time-dependence of diffusion coefficient measurements of tracers in different materials, e.g. rocks, soils and biological tissues, by nuclear magnetic resonance (NMR) spectroscopy with pulsed gradients of the applied magnetic field (Fordham et al., 1994; Latour et al., 1994). The model function that was derived by Loskutov and Sevriugin to describe tracer diffusion in porous media on multiple scales (Loskutov and Sevriugin, 2013) is given by

$$D_{\text{app}}(t) = (D_0 - D_\infty) \exp\left(-\frac{4\sqrt{D_0 t}}{\sqrt{\pi}\lambda}\right) + D_\infty. \quad (\text{Eq. 110})$$

This equation contains the following components: (i) Unhindered normal diffusion in a fluid without interactions with the embedding structure is described by the microscopic diffusion coefficient  $D_0$ . (ii) A characteristic parameter  $\lambda$  for a medium that has the dimension of a length. It gives the mean diffusive distance between two consecutive collisions with obstacles. (iii) In the limit of long times, the diffusion process is described by the macroscopic diffusion coefficient  $D_\infty$ . In this limit, all particles have collided with the pore wall several times, so that the on a macroscopic scale the structure looks homogenously again.

Previously, the measured time-dependence of liquids' diffusion coefficients in porous media was separately described for the short-time limit (Sen et al., 1994) and the long-time limit (De Sweit and Sen, 1996). The formula for short times reads

$$D_{\text{app}}(t) = D_0 \left(1 - \frac{4}{9\sqrt{\pi}} \frac{S}{V} \sqrt{D_0 t}\right). \quad (\text{Eq. 111})$$

Here, the surface to volume ration  $S/V$  gives the specific surface of the porous medium that was sensed by diffusing tracers. By expanding the exponential function in Eq. 110 into a Taylor series, it was approximated for short times by

$$D_{\text{app}}(t) = \left( D_0 - \frac{D_0}{R} \right) \left( 1 - \frac{4}{\sqrt{\pi}} \frac{\sqrt{D_0 t}}{\lambda} \right) + \frac{D_0}{R}. \quad (\text{Eq. 112})$$

The retardation  $R = D_0/D_\infty$  in Eq. 112 gives the reduction of the microscopic diffusion coefficient  $D_0$  compared to the macroscopic diffusion coefficient  $D_\infty$ . It is a measure for the connectivity of the accessible space for tracers in porous media and also for the amount of long detours that tracers have to diffuse around impermeable regions.

A relation between the mean diffusive distance  $\lambda$  between two consecutive collisions with obstacles and the specific surface  $S/V$  of the porous medium sensed by tracers can be calculated by comparison of Eq. 111 and Eq. 112. The specific surface  $S/V$  is given by

$$\frac{S}{V} = 9 \left( 1 - \frac{1}{R} \right) \frac{1}{\lambda}. \quad (\text{Eq. 113})$$

The model parameters microscopic diffusion coefficient  $D_0$ , macroscopic diffusion coefficient  $D_\infty$  and characteristic length  $\lambda$  as well as the derived parameters retardation  $R$  and specific surface  $S/V$  are depicted in schematic illustration for the time-dependent apparent diffusion coefficient of tracers in porous media in Figure 39.

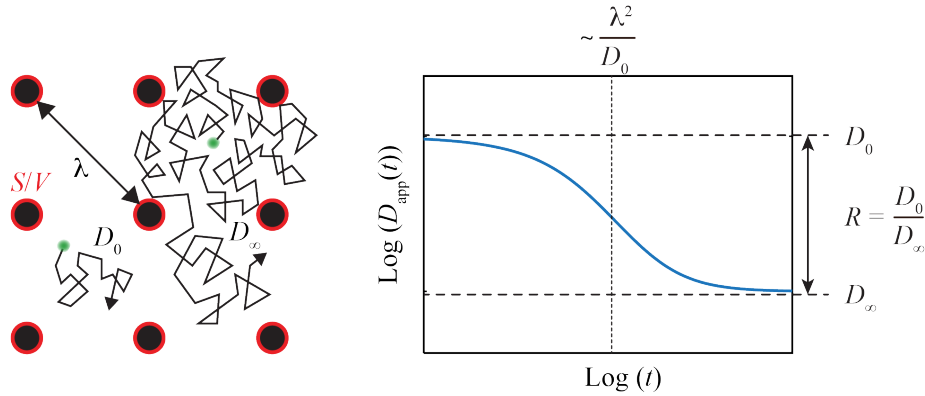


**Figure 39:** Parameters of the model function used for fitting the time-dependence of the apparent diffusion coefficient in porous media (Loskutov and Sevriugin, 2013). The initial slope of the  $D(t)$  curve is related to the surface-to-volume ratio or also called specific surface  $S/V$ . Extrapolation of  $D(t)$  to  $t=0$  yields the microscopic diffusion coefficient  $D_0$  that would be measured in free solution, and extrapolation of  $D(t)$  to  $t=\infty$  yields the macroscopic diffusion coefficient  $D_\infty$  for large translocations. The ratio between both diffusion coefficients is referred to here as retardation  $R$ . The squared mean diffusive displacement  $\lambda$  between two consecutive collisions with obstacles is proportional to the time at the point of inflection of the  $D(t)$ -curve. It is proportional to the length scale above which the medium appears homogeneous.

The model function that is valid for all time scales (Eq. 110) was fitted to the measured time-dependent apparent diffusion coefficients. Fit curves are plotted in Figure 38 as red and blue lines for cytoplasm and nucleus data, respectively.

The obtained fit results, i.e. the microscopic diffusion coefficient  $D_0$ , the macroscopic diffusion coefficient  $D_\infty$  and the correlation length of the porous medium  $\lambda$ , are summarized in Table 5. Furthermore, the retardations  $R = D_0/D_\infty$  and specific surfaces  $S/V$  given by Eq. 113 were calculated.

	GFP <sub>1</sub>		GFP <sub>3</sub>		GFP <sub>5</sub>	
	Cyt	Nuc	Cyt	Nuc	Cyt	Nuc
$D_0$ ( $\mu\text{m}^2/\text{s}$ )	$69 \pm 6$	$66 \pm 6$	$29 \pm 1$	$25 \pm 2$	$14 \pm 1$	$13 \pm 1$
$D_\infty$ ( $\mu\text{m}^2/\text{s}$ )	$30 \pm 4$	$29 \pm 3$	$9 \pm 1$	$8 \pm 1$	$2 \pm 1$	$\sim 1$ *
$R = D_0/D_\infty$	$2.3 \pm 0.2$	$2.3 \pm 0.2$	$3.2 \pm 0.1$	$3.1 \pm 0.3$	$6.6 \pm 0.7$	$\sim 33$ *
$S/V$ ( $\mu\text{m}^{-1}$ )	$6.3 \pm 1.3$	$6.3 \pm 1.4$	$4.0 \pm 0.4$	$3.9 \pm 0.7$	$2.5 \pm 0.7$	$1.6 \pm 0.2$
$\lambda$ ( $\mu\text{m}$ )	$0.8 \pm 0.2$	$0.8 \pm 0.2$	$1.5 \pm 0.2$	$1.6 \pm 0.3$	$3.1 \pm 0.9$	n. d.

**Table 5:** Fit results for the time-dependence of the apparent diffusion coefficient. The parameters were obtained by least squares fitting of the model function for diffusion in porous media (Loskutov and Sevriugin, 2013) to the experimental data. \* Since a significant fraction of GFP<sub>5</sub> is trapped in the nucleus according to the FRAP analysis, these values apply only for the mobile GFP<sub>5</sub> subpopulation.

The viscosity of the cellular fluid that is sensed by diffusing tracers on a microscopic length scale was compared to that in aqueous solution according to the Stokes-Einstein equation and the measured microscopic diffusion coefficients:

$$\frac{\eta_{0,\text{cell}}}{\eta_{0,\text{water}}} = \frac{D_{0,\text{water}}}{D_{0,\text{cell}}}. \quad (\text{Eq. 114})$$

In Figure 40, the relative viscosities  $\eta_{0,\text{cell}}/\eta_{0,\text{water}}$ , specific surfaces  $S/V$  and retardations  $R = D_0/D_\infty$  of GFP monomers and multimers in the cytoplasm and nucleus of living U2OS cells are plotted in bar plots as a function of the molecular weight  $M$ . GFP<sub>1</sub>, GFP<sub>3</sub> and GFP<sub>5</sub> have molecular weights of 27 kDa, 81 kDa 135 kDa, respectively.

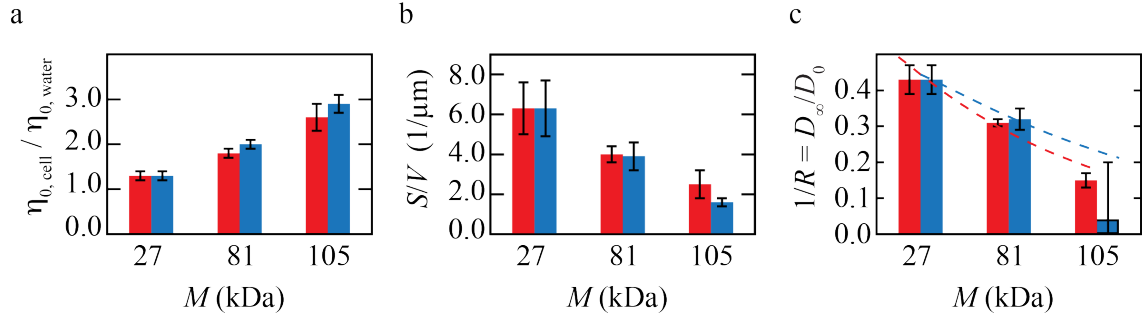


**Figure 40:** Summary of the determined parameters of the fit model function for diffusion in random media. Values for measurements in the cytoplasm are shown as red bars and in the nucleus as blue bars. **(a)** From the microscopic diffusion coefficient  $D_0$  and the diffusion coefficient of the proteins in aqueous solution, the apparent viscosity of the cellular fluid was determined. Remarkably, the apparent viscosity increased for proteins of higher molecular weights. **(b)** The specific surface that was sensed by diffusing proteins. It decreased with increasing protein size due to the lower permeability of the cellular medium for larger particles. **(c)** Inverse values of the retardation  $1/R$  of the microscopic diffusion coefficient  $D_0$  to the macroscopic limit  $D_\infty$ . The retardation  $R$ , a measure for long detours that proteins had to diffuse through around impermeable regions. It is inversely related to the connectivity of proteins' accessible space.

The retardation  $R$  depends on the proteins' size since dense cellular regions are only permeable for smaller proteins. An empirical relation between retardation  $R$  of a diffusing tracer with radius  $r_{\text{tracer}}$  in a random fiber network was proposed previously by Phillips (Phillips, 2000). The occupied volume fraction  $\Phi_0$  by fibrous obstacles and their radius  $r_{\text{fiber}}$  and characterize the random fiber network.  $\lambda_p = r_{\text{fiber}}/r_{\text{tracer}}$  is the ratio of the fiber radius to the tracer radius.

Eq. 115 gives the retardation  $R$  as a function of the tracer radius  $r_{\text{tracer}}$ :

$$\frac{1}{R} = F(\lambda_p, \Phi_0) S(\lambda_p, \Phi_0). \quad (\text{Eq. 115})$$

The term  $F(\lambda_p, \Phi_0)$  in Eq. 115 is represented by Eq. 116 that accounts for hydrodynamic effects.

$$F(\lambda, \Phi_0) = \exp(-a(\lambda_p) \Phi_0^{b(\lambda_p)}). \quad (\text{Eq. 116})$$

Further, the term  $S(\lambda_p, \Phi_0)$  in Eq. 115 accounts for steric or tortuosity effects:



$$S(\lambda, \Phi_0) = \exp\left(-0.84 \cdot f(\lambda_p, \Phi_0)^{1.09}\right), \quad (\text{Eq. 117})$$

with an adjusted volume fraction that reads as follows

$$f(\lambda, \Phi_0) = \left(1 + \frac{1}{\lambda_p}\right)^2 \Phi_0. \quad (\text{Eq. 118})$$

This model is applicable for small and moderate concentrations of obstacles in cytoplasm and nucleus since in this regime the mobility constraints imposed by a polymer network or a random obstacle distribution are similar (Fritsch and Langowski, 2010).

To fit the hindered diffusion model, the polynomial interpolation for the hindered diffusion parameters  $a(\lambda_p)$  and  $b(\lambda_p)$  as functions of the ratio  $\lambda_p = r_{\text{fiber}} / r_{\text{tracer}}$  of fiber radius  $r_{\text{fiber}}$  to tracer radius  $r_{\text{tracer}}$  as reported previously (Phillips, 2000) was replaced by an exponential interpolation (Figure 41). This approximation fitted similarly well as the polynomial approximation but avoided very large  $a(\lambda_p)$  and negative  $b(\lambda_p)$  parameters for  $\lambda_p$  values that were larger than the ones included by Phillips, which is advantageous for the fitting process and allowed for moderate extrapolation to larger  $\lambda_p$  values.

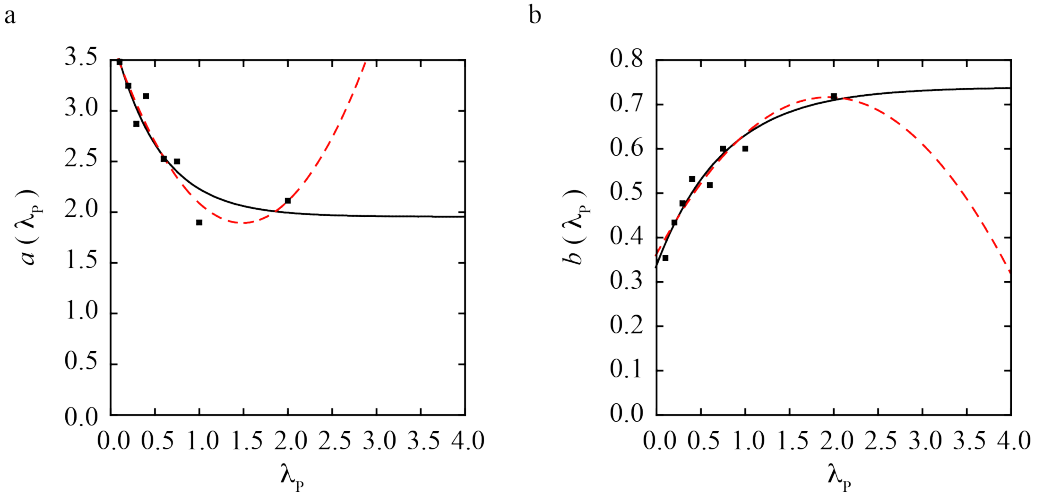


**Figure 41:** Interpolation of hindered diffusion parameters. The original polynomial interpolation for the hindered diffusion parameters  $a$  and  $b$  according to Philipps (Phillips, 2000) (red dashed lines) were compared to the modified exponential approximation (black lines). Both approximations yielded fits with reasonable quality. However, the modified interpolation avoided very large  $a$  parameters and negative  $b$  parameters for  $\lambda_p > 2$ , which could prevent successful fitting and preclude extrapolation for slightly larger  $\lambda_p$  values.

The empirical model function for diffusion in random fiber networks (Phillips, 2000) was fitted to the inverse values of the measured retardation of GFP<sub>1</sub>, GFP<sub>3</sub> and GFP<sub>5</sub> as a function of their molecular weights (Figure 38c). For the relation between the molecular weight  $M$  and effective hydrodynamic radius  $r_{\text{tracer}}$  the expression for ellipsoidal molecules with a rigid  $\alpha$ -helical shaped linker between neighboring GFP molecules was used (Pack et al., 2006). The effective hydrodynamic radius of monomeric GFP was calculated according to the Stokes-Einstein relation for the measured diffusion coefficient  $D_{\text{GFP}} = (88 \pm 3) \mu\text{m}^2/\text{s}$  in aqueous solution at temperature  $T = (295 \pm 1) \text{ K}$  as  $r_{\text{GFP}} = (2.8 \pm 0.1) \text{ nm}$ . The value for the diffusion coefficient of GFP in aqueous solution agreed well with results from scanning FCS measurements (Petrasek and Schwille, 2008). The hydrodynamic radii for GFP<sub>3</sub> and GFP<sub>5</sub> were calculated as 5.5 nm and 7.9 nm, respectively.

An occupied volume fraction of  $\Phi_0 = (12 \pm 9) \%$  and a fiber radius of  $r_{\text{fiber}} = (4 \pm 2) \text{ nm}$  were obtained for the cytoplasm. Similar values were determined for occupied volume fraction in the nucleus  $\Phi_0 = (18 \pm 5) \%$  and the obstacle fiber radius  $r_{\text{fiber}} = (6 \pm 2) \text{ nm}$ . The results for the fiber obstacle radii are of the same size as that of cytoskeletal filaments and chromatin fibers with a diameter of 10 nm.

#### **IV.5.2 Mobility of inert GFP<sub>3</sub> after degradation of cytoskeletal filaments**

Cytoskeletal filaments were degraded in living U2OS cells to measure their impact on protein transport in the cytoplasm. For this purpose, actin filaments that are built of actin protein subunits were degraded by addition of the drug cytochalasin D (CYTD) to the cell culture medium (Rubtsova et al., 1998). CYTD binds to the ends of actin filaments and thereby inhibits their dissociation and association. This results in almost complete disorganization of the actin network. Short actin filaments were observed in the cytoplasm (Cooper, 1987). The distribution of intermediate filaments was disrupted by treatment of the U2OS cells with withaferin A (WFA) that binds to their main building unit vimentin (Grin et al., 2012). Microtubule filaments that are built of  $\alpha$  tubulin and  $\beta$  tubulin proteins were depolymerized by nocodazole (NOC) (Jordan et al., 1992).

A confocal microscope was used to acquire images of U2OS cells with fluorescently labeled cytoskeletal filaments before and after treatment with cytoskeletal filaments

degrading drugs. After treatment of the U2OS cells, disassembly of the cytoskeletal filament networks was observed (Figure 42).

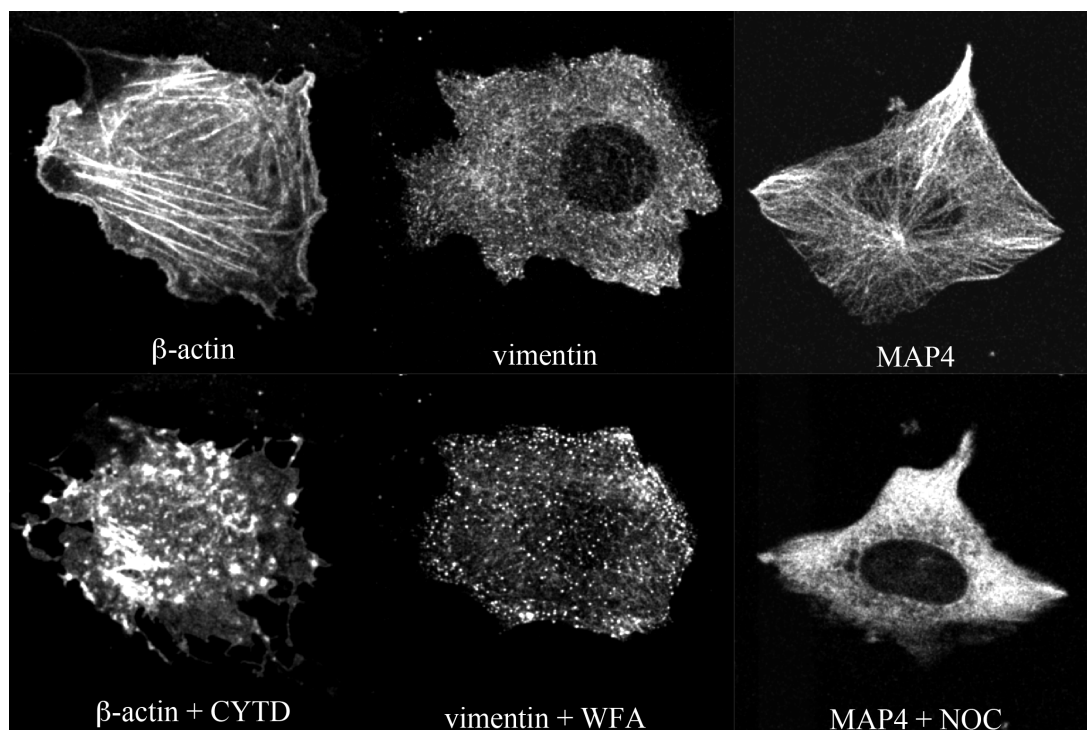


**Figure 42:** Fluorescence microscopy images of human U2OS cells before and after treatment with 8  $\mu$ M cytochalasin D (CYTD), 2  $\mu$ M withaferin A (WFA) and 10  $\mu$ M nocodazole (NOC). Actin filaments were stained with  $\beta$ -Actin-RFP, intermediate filaments were stained with vimentin-GFP and microtubule filaments were stained with MAP4-RFP. Disassembly of cytoskeletal filaments was observed after treatment with CYTD, WFA and NOC.

Cytoskeletal filaments' subunits were more heterogeneously distributed in the cytoplasm after treatment. Further, aggregation of filament components was observed.

After treatment, time-dependent apparent diffusion coefficients of GFP<sub>3</sub> were measured in the cytoplasm of at least 10 different U2OS cells by spatial FCCS with the line-confocal microscope. Eq. 110 was used for least squares fitting of the scale-dependent mobility data (Figure 43). The apparent diffusion coefficients as function of time deviated only moderately after treatment with WFA and NOC from that of unperturbed cells (Figure 43). Therefore, only minor effects of intermediate filaments and microtubuli on GFP<sub>3</sub> transport in the cytoplasm were revealed as compared to untreated cells. A significant difference was observed after treatment with CYTD (Figure 43). Here, the measured retardation of GFP<sub>3</sub> mobility was reduced compared to that in untreated cells, i.e. diffusing proteins

collide less frequently with barriers. However, the moderate effects observed here after disassembly of cytoskeletal filaments suggest that other cytosolic components also have a significant impact on molecular transport.

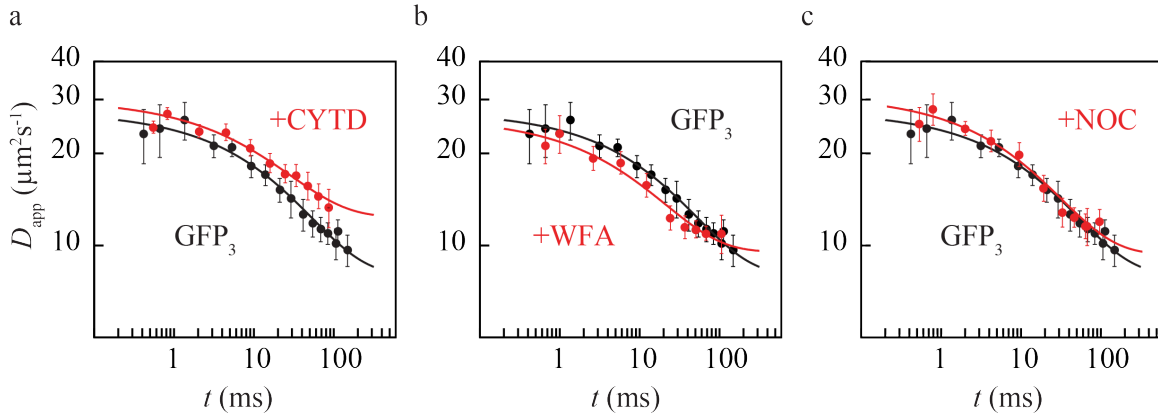


**Figure 43:** Time-dependent apparent diffusion coefficient (red) of inert GFP<sub>3</sub> in the cytoplasm of U2OS cells after degradation of cytoskeletal filaments with CYTD, WFA and NOC compared to that in unperturbed cells (black). **(a)** Depolymerization of actin filaments by cytochalasin D. **(b)** Disruption of intermediate filaments by withaferin A. **(c)** Disruption of microtubule by nocodazole.

All parameters that were obtained by least squares fitting of the model function for diffusion in porous media given by Eq. 110 to the measured mobility data for GFP<sub>3</sub> are summarized in Table 6. According to Eq. 113, the obstacle surface sensed by diffusing GFP<sub>3</sub> was calculated from the retardation  $R$  and the correlation length  $\lambda$ . The corresponding data for GFP<sub>3</sub> in the cytoplasm of unperturbed U2OS cells are listed in Table 5.

Treatment	$D_0$ ( $\mu\text{m}^2/\text{s}$ )	$R = D_0/D_\infty$	$S/V$ ( $\mu\text{m}^{-1}$ )	$\lambda$ ( $\mu\text{m}$ )
CYTD	$30 \pm 1$	$2.4 \pm 0.3$	$3.5 \pm 1.0$	$1.5 \pm 0.4$
WFA	$26 \pm 2$	$2.8 \pm 0.3$	$4.8 \pm 1.2$	$1.2 \pm 0.3$
NOC	$31 \pm 2$	$3.3 \pm 0.5$	$4.2 \pm 0.9$	$1.5 \pm 0.3$

**Table 6:** Result for least squares fitting of the model function for diffusion in porous media (Loskutov and Sevriugin, 2013) to the time-dependent apparent diffusion coefficient of GFP<sub>3</sub> in cytoplasm of U2OS cells after treatment with cytochalasin D (CYTD), withaferin A (WFA) and nocodazole (NOC).

#### IV.5.3 Mobility of inert GFP<sub>3</sub> after perturbations of the chromatin structure

Furthermore, the scaling behavior of protein transport was measured in the nucleus of human U2OS cells by spatial FCCS measurements after treatment with drugs that alter the

spatial organization of the chromatin. Trichostatin A (TSA) was used to modify the chromatin structure via epigenetic modifications of histone protein tails, more accurately the acetylation state (Fejes Tóth et al., 2004). Inhibition of histone deacetylation enzymes by TSA results in increased acetylation of histone tails and thus in decondensation of dense chromatin. Additionally, chloroquine (CQ) was used to modify the accessibility of the chromatin structure (Toiber et al., 2013). It intercalates into the DNA structure and thus changes the axial twist of linker DNA segments between neighboring nucleosomes.

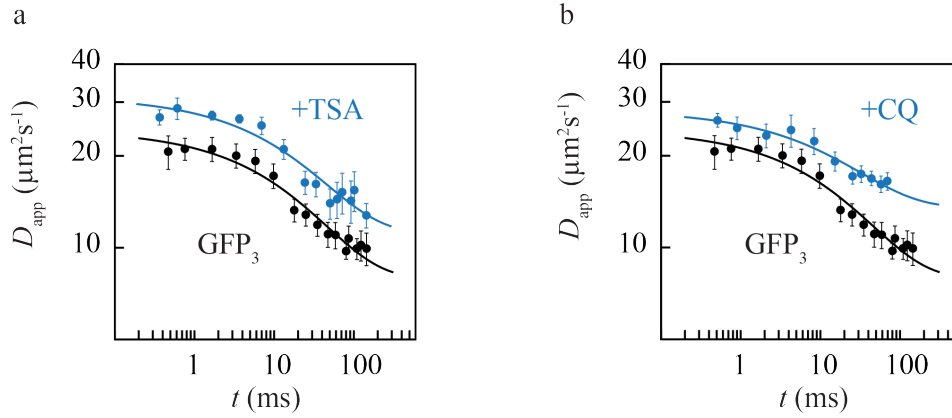


**Figure 44:** Time-dependent apparent diffusion coefficient (blue) of inert  $\text{GFP}_3$  in the nucleus of U2OS cells after perturbation of the chromatin structure with trichostatin A (TSA) and chloroquine (CQ) compared to that in unperturbed cells (black). **(a)** Perturbation of chromatin by TSA. **(b)** Perturbation of chromatin by CQ.

Spatial FCCS measurements were conducted in at least 10 different human U2OS cells after treatment with the chromatin decondensing drugs TSA and CQ. Figure 44 shows the averaged time dependence of the apparent diffusion coefficient for  $\text{GFP}_3$  molecules in the nucleus of perturbed cells as well as reference measurements in unperturbed cells. The mobility data were fitted by the model for diffusion of tracers in porous media given by Eq. 110. All determined parameters are summarized in Table 7.

Treatment	$D_0$ ( $\mu\text{m}^2/\text{s}$ )	$R = D_0/D_\infty$	$S/V$ ( $\mu\text{m}^{-1}$ )	$\lambda$ ( $\mu\text{m}$ )
TSA	$30 \pm 2$	$2.8 \pm 0.7$	$2.9 \pm 1.2$	$2.0 \pm 0.8$
CQ	$28 \pm 1$	$2.1 \pm 0.3$	$2.8 \pm 1.2$	$1.7 \pm 0.7$

**Table 7:** Result for least squares fitting of the model function for diffusion in porous media (Loskutov and Sevriugin, 2013) to the time-dependent apparent diffusion coefficient of  $\text{GFP}_3$  in the nucleus of U2OS cells after treatment with trichostatin A (TSA) and chloroquine (CQ).

The measured microscopic diffusion coefficients of GFP<sub>3</sub> in the nucleus were moderately increased after TSA and CQ treatment (Table 7) compared to that in untreated U2OS cells (Table 5). However, a significant effect was observed as reduced retardation value after treatment with CQ.

#### IV.5.4 Non-inert and endogenous STAT2 proteins and chromodomains

To study endogenous proteins' or respectively protein domains' time-dependent apparent diffusion coefficient, the mobility of STAT2 signaling pathway proteins (Stark and Darnell, 2012) in the cytoplasm and chromatin binding chromodomains (Brehm et al., 2004) in the nucleus of U2OS cells was measured by spatial FCCS.

Fluorescence microscopy images of typical cells that expressed GFP<sub>1</sub> labeled STAT2 proteins or chromodomains are shown in Figure 45.

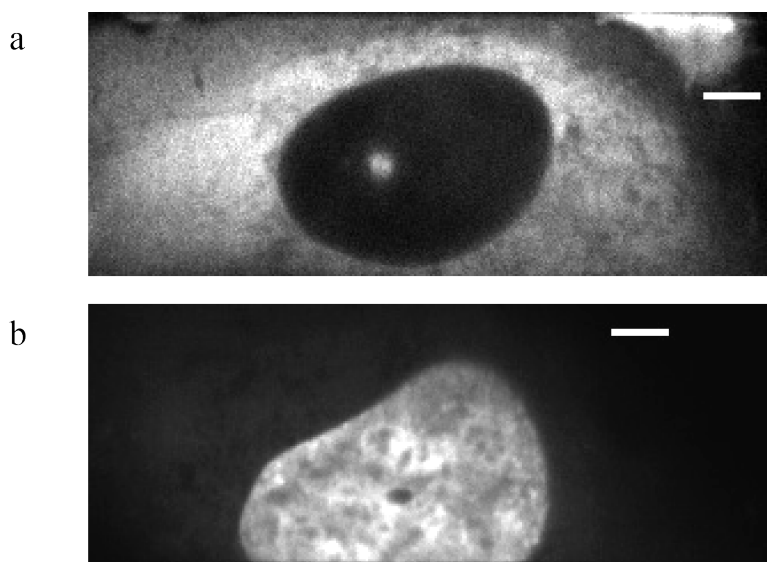


**Figure 45:** Fluorescence microscopy images of U2OS cells. The white scaling bars correspond to 5  $\mu$ m. **(a)** STAT2 proteins fluorescently labeled with GFP<sub>1</sub> (fusion proteins). STAT2 proteins were homogeneously distributed in the cytoplasm. The concentration of STAT2 was higher in cytoplasm as in the nucleus. The observable bright spot in the nucleus is an invagination of the cytoplasm. **(b)** Fusion proteins of the chromodomain and GFP<sub>1</sub>. In nucleus, chromodomains were enriched at the boundaries of nucleoli.

The fusion protein of the chromodomain (CD) and GFP<sub>1</sub> was chosen since it is comparable in molecular weight to the inert GFP<sub>1</sub>. Furthermore, a fusion protein of STAT2 and GFP<sub>1</sub> was used for comparison with the inert GFP<sub>5</sub>. The measured apparent diffusion coefficients were fitted by the model function for diffusion in porous media that is given by Eq. 110

(Loskutov and Sevriugin, 2013). Resulting parameters are summarized in Table 8. STAT2 proteins were faster than GFP<sub>5</sub> molecules in the cytoplasm (Figure 46a and Table 8) although both have comparable molecular weights of ~140 kDa. The difference between their mobility is assumed to originate from the difference in their molecular structures because GFP<sub>5</sub> is expected to have a more rod-like structure whereas for STAT2 proteins is expected (Dross et al., 2009).

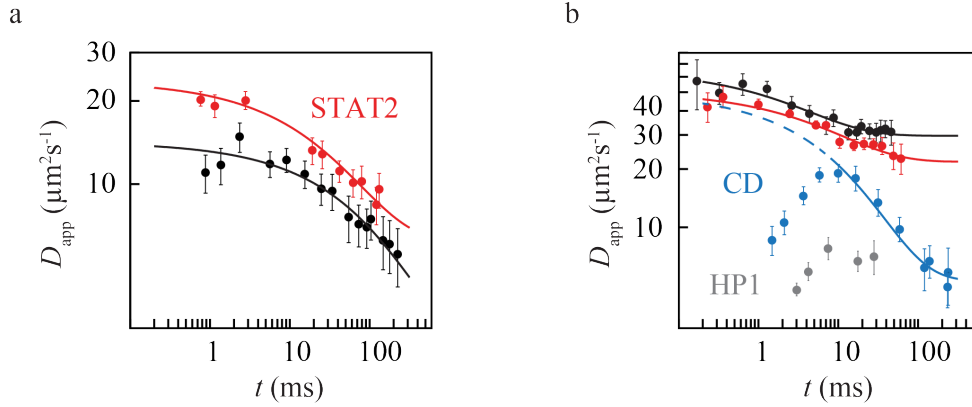


**Figure 46:** Time-dependent apparent diffusion coefficient of non-inert endogenous proteins and protein domains in the cytoplasm and nucleus of human U2OS cells. **(a)** Time dependent mobility of STAT2 proteins (red) in the cytoplasm compared to that of GFP<sub>5</sub> (black). **(b)** Mobility of chromodomain CD in the cytoplasm (red) and nucleus (blue) compared to that of GFP<sub>1</sub> (black) in the cytoplasm. Additionally, the measured time-dependence of the mobility of heterochromatin protein 1 (HP1) in the nucleus (grey) is depicted. These data could not be quantitatively analyzed, since only a limited time scale range was covered.

However, both proteins sense comparable environments (Table 8). In the cytoplasm, the time dependent mobility of CD was reduced compared to that of GFP<sub>1</sub> but revealed similar results for the intracellular structure (Table 8).

		$D_0$ ( $\mu\text{m}^2/\text{s}$ )	$R = D_0/D_\infty$	$S/V$ ( $\mu\text{m}^{-1}$ )	$\lambda$ ( $\mu\text{m}$ )
<b>CD</b>	<b>Cyt</b>	$51 \pm 2$	$2.3 \pm 0.2$	$3.9 \pm 0.9$	$1.3 \pm 0.3$
	<b>Nuc</b>	$51^*$	$9.4 \pm 0.9$	$5.4 \pm 0.4^\circ$	$1.5 \pm 0.1$
<b>STAT2</b>	<b>Cyt</b>	$24 \pm 1$	$3.8 \pm 0.8$	$3.3 \pm 1.3$	$2.0 \pm 0.8$

**Table 8:** The results for chromodomain (CD) and STAT2 protein in the cytoplasm (Cyt) and nucleus (Nuc) of human U2OS cells are listed. \* This value was fixed for least squares fitting to the microscopic diffusion coefficient of CD in the cytoplasm since these values should be similar in the short timescale limit. <sup>°</sup> Only an effective specific surface value can be determined since CD is binding to chromatin.

The mobility of CD in the nucleus was significantly reduced compared to that in the cytoplasm due to transient binding to chromatin. Additionally, a time-dependence of the

apparent diffusion coefficient was observed that is not implemented in the model for diffusion of inert tracers in porous media. It is assumed that the measured deviations from the sigmoidal functional relationship of the apparent diffusion coefficients originate from binding fluctuations on short time scales that are superposed with the hindrance by the intracellular structure. In the short time scale limit, the microscopic diffusion coefficient of CD in the nucleus should be similar to that in the cytoplasm. With this assumption, an increased effective retardation value could be estimated for CD in the nucleus (Table 8).

## IV.6 Protein interaction measurements by dual-color FCCS

### IV.6.1 Reference measurements

#### IV.6.1.1 TetraSpeck beads in aqueous solution

Dual-color FCCS with the implemented second detection channel for red fluorescence light was tested by measurements of diffusing TetraSpeck beads in aqueous solution. The TetraSpeck beads are made of polystyrene and have a diameter of 0.1  $\mu\text{m}$ . Their surfaces are labeled with blue, yellow-green, orange and dark red dyes. Accordingly, cross-correlation between red and green fluorescence signals was expected for dual-color FCCS measurements. Excitation and emission spectra for these dyes as well as illumination laser wavelength and optical filters are depicted in Figure 47.

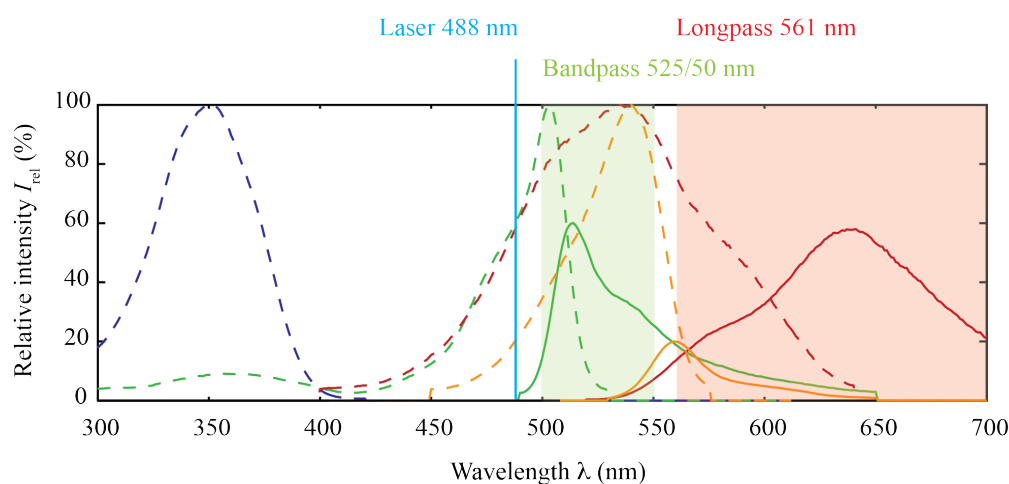


**Figure 47:** Fluorescence excitation (dashed lines) and emission (solid lines) spectra of the blue, yellow-green, orange and dark red dyes on the surface of polystyrene TetraSpeck beads. The wavelength of the laser (488 nm) is depicted as light blue line. Emission spectra are normalized according to the excitation efficiency with laser light of 488 nm. A bandpass filter (525/50 nm) in the detection light path was used for the green fluorescent light and a longpass filter (561 nm) for the red fluorescent light.



Spectral crosstalk was corrected according to an approach introduced previously (Erdel, 2012). Calculated auto-correlation curves for the crosstalk corrected signals acquired by the detection channel for green and red fluorescence light as well as the dual-color cross-correlation curve of both signals are depicted in Figure 48. Since the correlation amplitude of the green signal was higher than that of the red signal, it seems that either about every fourth TetraSpeck bead had photobleached green dyes or the labeling efficiency of TetraSpeck beads was not equal for the red and green dyes. Furthermore, the MDE of the line confocal microscope's green and red detection channels could be different. However, strong cross-correlation between the red and green fluorescence signals was obtained in a first proof-of-concept dual-color FCCS measurement with the line confocal microscope.

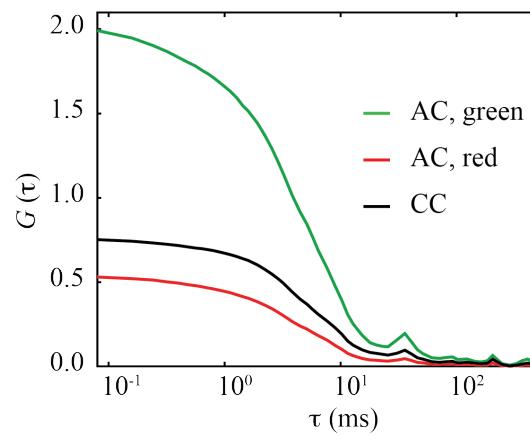


**Figure 48:** Auto-correlation (AC) and cross-correlation (CC) curves of TetraSpeck beads in aqueous solution calculated from the crosstalk corrected signals acquired by the green and red fluorescence detection channel. Since the amplitude of the AC curve of the green channel was higher than that of the red channel, it seems that about every fourth TetraSpeck had photobleached green dyes.

#### IV.6.1.2 Fusion protein of GFP and LSS-mKate2 in living cells

To validate dual-color FCCS with the setup developed here, the mobility of fusion proteins of LSS-mKate2 and GFP was measured by 1D-FCS with the line-confocal microscope in human U2OS cells. LSS-mKate2 is a monomeric red fluorescent protein that has a long Stokes shift between its excitation maximum at 460 nm and its emission maximum at 605 nm (Piatkevich et al., 2010). It allows for single wavelength excitation of GFP and LSS-mKate2 molecules, which intrinsically avoids potential misalignment between different illumination volumes in the sample (Hwang and Wohland, 2004). As a negative control, the mobility of GFP and LSS-mKate2 was measured in cells that expressed both proteins separately. The fluorescence signals of the red and green detection channels were either

auto-correlated or cross-correlated with the corresponding signal of the other detection channel at the same position. Subsequently, correlation curves were corrected for spectral detection crosstalk of the green fluorescent dye into the red detection channel according to Eq. 68. Calculated AC and XC curves acquired at 30 positions in the cell were averaged and fitted with Eq. 92 (Figure 49).

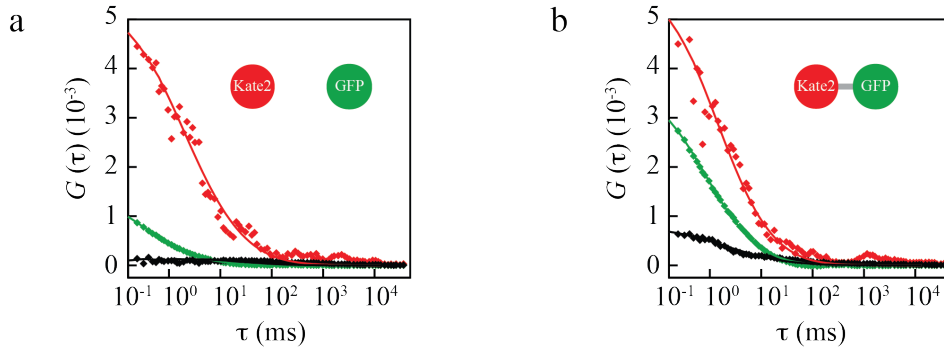


**Figure 49:** Negative and positive control for dual-color FCCS analysis of 1D-FCS measurements in the cytoplasm of U2OS cells. Experimental AC and CC curves acquired at 30 positions were averaged and corrected for spectral crosstalk. **(a)** AC and CC curves (diamonds) acquired in cells expressing GFP and LSS-mKate2 separately, including the fitted model functions (lines). After spectral crosstalk correction, no significant cross-correlation between the red and the green detection channels was observed. **(b)** Results of dual-color FCCS analysis of 1D-FCS measurements in cells that expressed a fusion protein of LSS-mKate2 and GFP. A significant cross-correlation between red and green detection channels remained after spectral crosstalk correction.

After spectral crosstalk correction, the cross-correlation amplitude of fluorescence signals from GFP and LSS-mKate2 vanished in cells that expressed both proteins separately (Figure 49a). However, significant cross-correlation was obtained in cells that expressed a fusion protein of GFP and LSS-mKate2 (Figure 49b). The fraction  $\theta_{\text{GFP}}$  of GFP molecules that were in a fusion protein with both fluorescent proteins in an active state was calculated from the amplitudes of the fit curves obtained by fitting Eq. 92 to the acquired AC and CC curves according to Eq. 119 (Bacia et al., 2006; Weidemann et al., 2002):

$$\theta_{\text{GFP}} = \frac{G_{\text{CC}}(0)}{G_{\text{r}}(0)} = \frac{N_{\text{Kate2-GFP}}}{N_{\text{GFP}} + N_{\text{Kate2-GFP}}}. \quad \text{Eq. 119}$$

$G_{\text{r}}(0)$  and  $G_{\text{CC}}(0)$  in Eq. 119 are the amplitudes at time  $\tau=0$  of the red channel's AC curve and that of the CC curve. The number of red and green fluorescent fusion proteins is

represented by  $N_{\text{Kate2-GFP}}$ , whereas the number of fusion proteins that were only green fluorescent is given by  $N_{\text{GFP}}$ . Accordingly, the ratio  $\theta_{\text{Kate2}}$  of LSS-mKate2 proteins that were in red and green fluorescent proteins reads:

$$\theta_{\text{Kate}} = \frac{G_{\text{CC}}(0)}{G_{\text{g}}(0)} = \frac{N_{\text{Kate2-GFP}}}{N_{\text{Kate2}} + N_{\text{Kate2-GFP}}}. \quad \text{Eq. 120}$$

From the fractions  $\theta_{\text{GFP}}$  and  $\theta_{\text{Kate2}}$ , the ratios between the numbers of only green, only red as well as green and red fluorescent fusion proteins was calculated as 6:4:1. The number of fusion proteins that were fluorescent both in the red and green channel might be reduced since not all fluorescent proteins are completely matured and therefore stay dark.

#### IV.6.2 Dimerization of STAT1 and STAT2 proteins in the cytoplasm

Dimerization of the signaling proteins STAT1 and STAT2 (Stark and Darnell, 2012) was measured in the cytoplasm of human U2OS cells with and without interferon stimulation by dual-color FCCS with single wavelength excitation. For this purpose, STAT1 proteins were fluorescently labeled with LSS-mKate2 and STAT2 proteins were fluorescently labeled with GFP. Representative fluorescence microscopy images are shown in Figure 50.

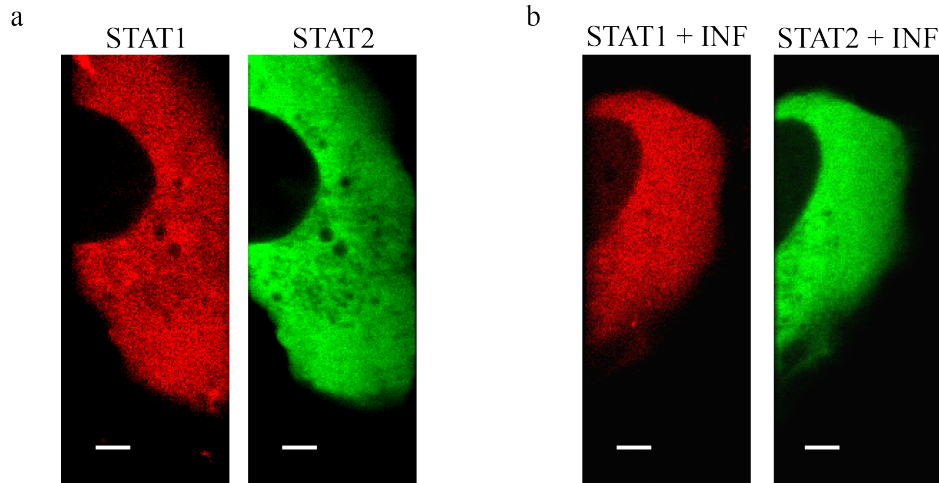


**Figure 50:** Fluorescence microscopy images of STAT1 and STAT2 proteins expressing human U2OS cells. STAT1 proteins were fluorescently labeled with LSSmKate2 and STAT2 proteins with GFP. The white scaling bars correspond to 5  $\mu\text{m}$ . **(a)** A representative cell without stimulation by interferon. **(b)** A representative cell after stimulation with interferon. A slight enrichment of STAT1 and STAT2 proteins in the nucleus was observed after stimulation with interferon (INF) compared to the unstimulated case.

Binding of interferon molecules to receptors on the plasma membrane finally leads to formation of heterodimers of STAT1 and STAT2. It is expected that the heterodimer protein of STAT1 and STAT2 is transported into the nucleus after interferon stimulation, where it binds to chromatin and activates gene expression. However, only a slight enrichment of STAT1 and STAT2 was observed in the nucleus after treatment with interferon (Figure 50), which might be due to inefficient stimulation or saturation by overexpressed STAT proteins. Interactions of STAT1 and STAT2 proteins were measured by dual-color FCCS analysis of 1D-FCS data acquired with the line-confocal microscope at 30 positions in the cytoplasm of living U2OS cells. The calculated AC and CC curves were averaged and corrected for spectral crosstalk of GFP into the red detection channel. Least square fitting with Eq. 92 yielded the amplitudes  $G(0)$  of AC and CC curves.

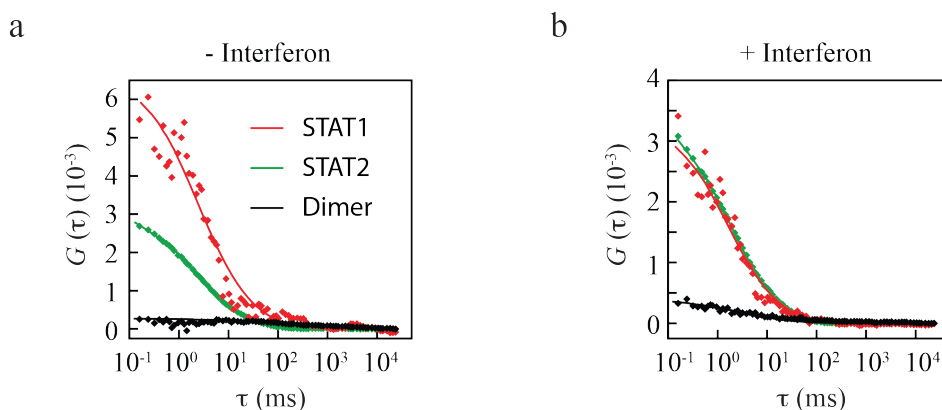


**Figure 51:** Interaction measurements of STAT1 and STAT2 proteins in the cytoplasm of U2OS cells by dual-color FCCS analysis of 1D-FCS data acquired with the line-confocal microscope. **(a)** AC and CC curves (diamonds) of the red and green detection channel acquired in unstimulated cells, including the fitted model functions (lines). **(b)** After treatment of the cells with interferon, significant cross-correlation was observed, indicating the presence of heterodimers between STAT1 and STAT2 in the cytoplasm.

After stimulation with interferon, a fraction of  $(11 \pm 1) \%$  STAT1 proteins were observed in a heterodimer with STAT2, whereas  $(7 \pm 1) \%$  STAT1 dimerized with STAT2 proteins without external stimulation. The fractions of STAT1 proteins that formed a heterodimer with STAT2 was calculated from the correlation amplitudes according to Eq. 120.

## V Discussion

### *V.1 Impact of the microscope's MDE on FCS measurement results*

The shape of AC and CC curves obtained from FCS measurements is affected by the concentration and mobility of fluorescent particles, optical saturation effects (Enderlein et al., 2005; Gregor et al., 2005) as well as photophysical effects of the fluorophore (Haupts et al., 1998) and the geometry of the MDE volume (Enderlein et al., 2004). In the correlation model function for FCS used for confocal microscopes, the MDE is typically described by a three-dimensional Gaussian function (Rigler et al., 1993). However, this does not represent the experimental situation accurately and thus causes deviations of the measured diffusion coefficients and concentrations (Enderlein et al., 2004; Hess and Webb, 2002). A more accurate model function for the MDE of confocal microscopes was reported previously (Dertinger et al., 2007). It uses a double cone shape of the excitation and detection volume in axial direction.

For determining the MDE of a microscope, fluorescent beads with diameters below the diffraction limit are commonly fixed on the surface of object slides and subsequently imaged. The resulting three-dimensional image stacks are then fitted by model functions that describe the MDE for quantitative analysis of FCS measurements. However, diffusion coefficients of inorganic dyes measured in aqueous solution by point FCS and three-dimensional Gaussian MDE model function were significantly underestimated compared to that measured by dual-focus FCS and the double cone MDE model (Dertinger et al., 2007; Müller et al., 2008), mostly due to the inaccurately described MDE geometry.

Multi-focus FCS measurements allow for precise quantification of absolute diffusion coefficients (Dertinger et al., 2007; Müller et al., 2008). The results of spatial FCCS become independent of the MDE volume geometry for large separation distances between the detection volumes. The measured diffusion coefficients are comparable to those obtained by pulsed field gradient nuclear magnetic resonance (PFG-NMR) experiments (Gendron et al., 2008), dynamic light scattering measurements (DLS) (Müller et al., 2008) and 3PEA (Erdel and Rippe, 2012). Accordingly, 1D-FCS underestimated diffusion coefficients in the AC analysis if the line-confocal microscope's MDE volume was described by a three-dimensional Gaussian function, as shown in Figure 52. However, accurate values were obtained by long-distance CC analysis. It is possible to address the

discrepancy between the diffusion coefficients determined by AC and long-distance CC analysis by adjusting the structural parameters of the three-dimensional Gaussian model function. However, the diffusion coefficients obtained by spatial FCCS for intermediate separation were nevertheless underestimated, i.e. no structural parameter set for a Gaussian MDE description was found that yielded consistent diffusion coefficients for all length scales.

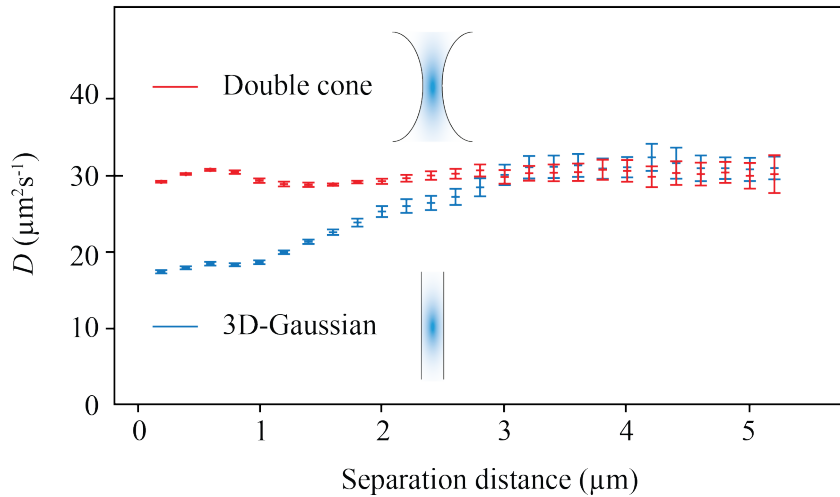


**Figure 52:** Diffusion coefficients obtained by spatial FCCS with the line-confocal microscope for a 3D-Gaussian and a double cone MDE model function. The measured diffusion coefficients were equal for large separation distances ( $> 3 \mu\text{m}$ ). However, AC analysis with 3D-Gaussian MDE model underestimated the diffusion coefficient significantly, although MDE model parameters were determined from the same image stacks of fluorescent beads.

Accurate diffusion coefficients could only be obtained from the AC and CC analysis if the double cone MDE model function derived here with multiple side lobes was employed (Eq. 82). However, the appropriate model function for the theoretical description of the correlation curves (Eq. 92) required numerical solution of a double integral. Hence, least square fitting of this model to the experimental data is somewhat more computationally intensive and time-consuming. The analysis of the correlation curves can be computed in parallel within less than an hour on modern computer hardware. A further speedup could be obtained with a theoretical model function for the line-confocal microscope's MDE of double cone geometry that allows for deriving an analytical model function for the correlation curves.

For correct diffusion coefficient measurements, the structural parameters of the MDE have to be determined accurately. However, image stacks of fluorescent beads fixed on the surface of object slides showed some distortions (Figure 27). Therefore, structural parameters for the MDE measured in this manner deviated significantly from that required for the FCS model functions in aqueous solution. In this thesis, an approach for optimizing the structural parameters determined by bead imaging on surfaces of object slides was developed. It uses a computer optimization routine and reference concentration and diffusion coefficient measurements of fluorescent dyes by spatial FCCS in aqueous solution where these parameters are independent from the separation distance between detection volumes (Figure 32). With this optimization routine, reliable diffusion coefficients were obtained by spatial FCCS on different time and length scales, as shown in Figure 19. The approach to characterize MDE functions for the quantitative analysis of FCS curves is generally relevant for FCS data acquisition with microscopy setups that have detection crosstalk due to overlapping detection volumes. This is the case for all optical setups that illuminate a region in the sample with continuous laser light and simultaneously detect emitted fluorescence signals from multiple positions with high spatial resolution, e.g. SPIM setups used for 2D-FCS measurements.

## ***V.2 Anomalous diffusion measurements in living cells***

Mobility measurements by conventional FCS, FRAP and SPT revealed that diffusion of particles in a crowded and heterogeneous environment followed an anomalous diffusion law (Brown et al., 1999; Kues et al., 2001; Wachsmuth et al., 2000; Weiss et al., 2004), i.e. the MSD of diffusing particles does not increase linearly with time. However, the actual relation between MSD and time could not be determined so far for the complete time scale range relevant for diffusion of molecules in living cells. For simplicity, the MSD of anomalous diffusion in living cells was described by a power law (Eq. 21), which is valid only for fractal obstacle distributions (Bouchaud and Georges, 1990; Bunde and Havlin, 1995). In perfect fractal structures that do not have a characteristic length scale, true anomalous diffusion will be observed on all length and time scales. In contrast, real physical systems have a finite number of characteristic length scales. As discussed previously, diffusion in a complex medium with one characteristic length scale  $\lambda$  should be normal for  $MSD \ll \lambda^2$  and correspond to that in fluids without obstacles (Banks and Fradin, 2005). For  $MSD \gg \lambda^2$ , diffusion of tracers should again be normal and correspond

to that in the composite medium. If the MSD is comparable to the characteristic length scale squared ( $MSD \approx \lambda^2$ ), diffusion has to be anomalous to bridge these two regimes with normal diffusion. This time-dependence was found for diffusion in environments with random barriers (Novikov et al., 2011) and in porous media (Loskutov and Sevriugin, 2013).

Accordingly, the mobility of diffusing particles has to be measured on multiple time and length scales to reveal diffusion laws in biological cells. Unfortunately, most conventional mobility measurement techniques are restricted to a small range of scales. For example, FCS measurements at a single point are restricted to the characteristic length of their MDE volumes. Anomalous diffusion is extracted from the slope at the point of inflection of the calculated AC curves that is related to the anomaly parameter  $\alpha$  of the anomalous diffusion propagator given by Eq. 91. The latter is affected by several experimental artifacts, e.g. photophysical effects of the fluorophore and the geometry of the MDE volume (Enderlein et al., 2004), occurrence of multiple diffusing species of fluorescent molecules as well as signal correction (Figure 24c). Based on the ill-defined anomaly parameter  $\alpha$ , conclusions for smaller and larger length scale ranges are drawn by extrapolation of the diffusing particles' MSD according to a power law (Eq. 21).

By increasing the size of the focus volume, the accessible scale range can be extended (Masuda et al., 2005) until the large number of fluorescent particles in the detection volume reduces the relative fluctuations beyond the range that can be reliably measured. Another approach is SPT that yields low statistics since single particles can only be traced for a limited period of time before they are either lost by the tracking routine or get photobleached. Furthermore, the temporal resolution of SPT is too low for tracking of most relevant proteins.

To overcome these limitations, an experimental and theoretical framework for spatial FCCS measurements with line-confocal microscopes was developed here. This methodology allows for mobility measurements on a length scale range from 200 nm to 3  $\mu\text{m}$ . With this approach the time dependence of the apparent diffusion coefficient  $D_{\text{app}}(t)$  was determined on multiple time and length scales by a single measurement. In living cells, it showed a sigmoidal curve in the double-logarithmic representation (Figure 38, Figure 43 and Figure 44) that is indicative for diffusion in porous media. By least squares fitting of Eq. 110 to the  $D_{\text{app}}(t)$  curves, microscopic diffusion coefficients were determined



that allowed for calculation of the apparent microscopic viscosity. Interestingly, it was dependent on the size of the fluorescent molecules (Figure 40 and Table 5). This finding is consistent with previous reports and shows that normal diffusion laws do not apply in living cells (Luby-Phelps, 1994; Luby-Phelps et al., 1986; Lukacs et al., 2000). Slow or even immobile cellular components might be sensed by small particles as obstacles whereas the same components contribute to an increased apparent viscosity for large particles. This is in accordance with the increase of the effective viscosity of the medium due to molecular crowding that is higher for large tracers (Zimmerman and Minton, 1993). Furthermore, the difference between microscopic diffusion coefficient  $D_0$  and the macroscopic diffusion coefficient  $D_\infty$  was measured (Figure 40 and Table 5). These results are consistent with the literature (Busch et al., 2000; Lavalette et al., 1999). They imply that anomalous diffusion occurs on the scale range of the crossover between both diffusion coefficients. Accordingly, the model for anomalous diffusion in fractal structures applies only for a limited scale range of this crossover regime as discussed previously (Bancaud et al., 2009). Multiple fractal dimensions are required for the description of the scale-dependence of anomalous diffusion in the complex environment of living cells. Mobility measurement techniques that operate on different time and length scales may yield deviating results in living cells due to the time-dependence of the apparent diffusion coefficient – even if the results are consistent for measurements in aqueous solution.

<b>Spatial FCCS in living cells (nucleus)</b>	<b><math>D</math> (<math>\mu\text{m}^2\text{s}^{-1}</math>)</b>
GFP <sub>1</sub>	$32 \pm 3^x$
GFP <sub>3</sub>	$14 \pm 2^x$
GFP <sub>5</sub>	$11 \pm 1^x$
<b>FRAP in living cells (nucleus)</b>	<b><math>D</math> (<math>\mu\text{m}^2\text{s}^{-1}</math>)</b>
RFP <sub>1</sub>	$31 \pm 7^o$
GFP <sub>3</sub>	$15 \pm 4^o$
GFP <sub>5</sub>	$10 \pm 1^o$

**Table 9:** Mobility parameters obtained for different tracer molecules in the nucleus of living cells by spatial FCCS and FRAP with radial profile analysis. Spatial FCCS results in living cells agreed very well with FRAP experiments on the same length scale. <sup>x</sup> Diffusion constants for spatial FCCS analysis with an effective distance of  $d_{\text{eff}} = 1.2 \mu\text{m}$ . <sup>o</sup> FRAP results for a bleach circle radius of  $w_b \approx 1.3 \mu\text{m}$ .

Therefore, the spatial FCCS approach developed here is ideally suited to obtain reference measurements for the comparison of results obtained with different methods. This is illustrated by the diffusion coefficient data for RFP<sub>1</sub>, GFP<sub>3</sub> and GFP<sub>5</sub> measured by FRAP with a bleach radius of 1.3  $\mu\text{m}$  in comparison for those obtained by spatial FCCS for 1.3  $\mu\text{m}$  separation distance (Table 9). The results of both methods are in excellent agreement when compared on the appropriate length scale. The time-dependence of the apparent diffusion coefficient impacts on the kinetics of diffusion-limited reactions in living cells (Gauthier and Bechhoefer, 2009) and on the efficiency of target search processes (Guigas and Weiss, 2008). Further, the stability of pattern formation processes is linked to anomalous diffusion (Weiss, 2003).

The scale range of the approach described here can be further extended in a straightforward manner. Shorter time and length scales down to 30 nm could be reached by using FCS in combination with stimulated emission depletion microscopy (STED) (Mueller et al., 2013). For reaching larger scales one would have to improve the detection sensitivity of the line-confocal optical system and/or use brighter and more photostable fluorescent dyes. Furthermore, the experimental and theoretical methodology developed here for 1D-FCS with a line-confocal microscope setup can be easily transferred to 2D-FCS measurements with SPIM instruments. One caveat could arise from the higher total laser light illumination exposure of molecules in the complete plane 2D-FCS as compared to that of 1D-FCS setup. This might result in higher photobleaching rates of fluorophores, although line-confocal setups illuminate regions in axial direction that are not detected. The intensity decreases rapidly in axial direction due to the diverging laser beam so that the laser intensity is distributed over larger areas with increasing distance from the focal plane. Therefore, the maximum total measurement time of 2D-FCS measurements will strongly depend on photobleaching of the limited amount of fluorophores present in the cell that is studied.

Due to simultaneous illumination of extended volumes in the sample with laser light, a notable fraction of fluorescent proteins is photobleached also in the 1D-FCS setup in mostly out-of-focus regions during an experiment. To reduce the amount of photobleaching, the excitation volume has to be confined. This can be achieved by two-photon excitation of fluorescent dyes with infrared light of pulsed lasers (Bhawalkar et al., 1996; Denk et al., 1990; Helmchen and Denk, 2005). Two-photon excitation was already applied for FCS measurements with conventional confocal microscopes (Berland et al.,

1995; Schwille et al., 1997). The intensity of the pulsed excitation laser light is high enough for nonlinear excitation processes only near the focal plane, which limits the extension of the microscope's MDE volume and thereby reduces the amount of bleached fluorophores. Besides, detection crosstalk due to overlapping neighboring detection volumes could be reduced. Multi-photon excitation by longer-wavelength laser light could also be valuable for 2D-FCS measurements with SPIM setups.

### ***V.3 Intracellular structure from a diffusing protein's point of view***

The measured time dependence of GFP monomers' and multimers' apparent diffusion coefficients in the crowded environment of living cells (Figure 38) were consistent with that obtained from PFG-NMR experiments in porous media, e.g. for diffusion of water molecules in biological tissue (Latour et al., 1994) and in rocks (Fordham et al., 1994). Therefore, a simple model for diffusion in such an environment was fitted to the experimental data (Loskutov and Sevriugin, 2013). In this manner the microscopic diffusion coefficient  $D_0$  for diffusion in the cellular fluid without obstacles, the mean diffusive displacement  $\lambda$  between two consecutive collisions with obstacles, and the macroscopic diffusion coefficient  $D_\infty$  were determined. From these parameters, the specific surface  $S/V$  (surface-to-volume ratio) that is sensed by diffusing particles and the retardation  $R$  of the apparent diffusion coefficient from its microscopic value to the macroscopic limit can be calculated. The retardation is a measure for the connectivity of the space that is accessible for diffusing particles or, in other words, the amount of long detours that particles have to diffuse around impermeable cellular obstacles. A small  $R$  value indicates a high permeability of the medium and a high connectivity of the accessible open space. The increase of  $R$  for larger effective hydrodynamic radii observed here (Table 5) is consistent with mobility measurement results in the literature (Busch et al., 2000; Lavalette et al., 1999).

The retardation measured here was further analyzed as a function of molecule size with an empirical model for diffusion of tracers in random fiber networks (Phillips, 2000). With this approach, the volume fraction that is occupied by obstacles and the fiber radius could be estimated for the cytoplasm and the nucleus. The experiments revealed that cytoskeletal filaments have only a moderate impact on the time-dependence of the apparent diffusion coefficients in the cytoplasm. Thus, other obstacles like membrane stacks or vesicles also

seem to hinder diffusing particles. The volume fraction of  $\Phi_0 = (18 \pm 5)\%$  and fiber diameter of  $r_{\text{fiber}} = (12 \pm 4)$  nm in the nucleus were in very good agreement with the width of 11 nm for nucleosome chains (Fussner et al., 2011; Maeshima et al., 2010) and the chromatin volume fraction of  $\sim 18\%$  (Fussner et al., 2011; Rippe, 2007).

Thus, in the framework of porous media, the cellular interior consist of obstacles that build a sponge-like structure with various pore sizes and geometries as well as an embedding viscous fluid due to macromolecular crowding. Retrieving information about confining geometries from the time dependence of the apparent diffusion coefficient is a well-established concept in the field of PFG-NMR spectroscopy (Sen, 2004). In contrast to the multi-scale spatial FCCS technique developed here, measurements of time-dependent diffusion coefficients in compartments of single are not feasible with PFG-NMR spectroscopy.

The results of least squares fitting of Eq. 111 to the apparent diffusion coefficients  $D_{\text{app}}(t)$  (Figure 38) of GFP<sub>1</sub>, GFP<sub>3</sub> and GFP<sub>5</sub> in the cytoplasm and nucleus of U2OS cells revealed that small particles sense a quite different environment than large particles since the characteristic length  $\lambda$  of the structure, the retardation  $R$  and the specific surface  $S/V$  were dependent on the molecules' size (Table 5). The increase of the characteristic length  $\lambda$  with molecules' effective hydrodynamic radius could be explained by a decreasing difference between the mobility of the tracers and the intracellular structure: Faster particles would be deflected from the bordering regions of dense domains, e.g. chromosome territories in the nucleus, more frequently than slower ones. Regions with moderate density are sensed as obstacles by small particles whereas they only enhance the macromolecular crowding effect for large particles. Furthermore, small particles can penetrate into smaller pores, which shift the mean pore size for their mobility to smaller length scales compared to that of large particles. The characteristic length scales measured here fit very well to the values reported for the interchromosomal space between chromosome territories in the nucleus (Cremer and Cremer, 2001).

The  $S/V$  values increased as a function of the molecules' effective hydrodynamic radii (Table 5). Small particles have access to dense regions that are impermeable for large particles. Thus, the total surface that is sensed by small particles is larger than that of large particles. The size-dependent accessibility of the intracellular structure could act as a molecular sieve. It allows for creating reaction volumes with different compositions of

interacting molecules. In the nucleus, denser regions, for example heterochromatic regions near the nuclear lamina and the interior of chromosome territories, exclude large particles so that preferentially smaller particles can interact in this environment (Cremer and Cremer, 2001). A schematic illustration for all structural parameters is depicted in Figure 53.

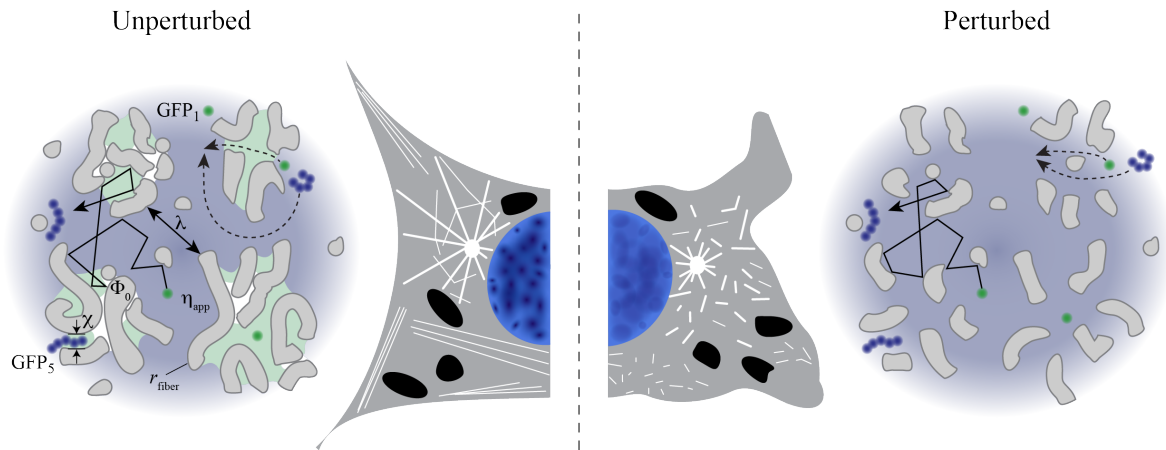


**Figure 53:** A model for the cellular structure as porous medium composed of randomly distributed obstacles. Smaller proteins have access to denser regions of the random obstacle network, and therefore have to take fewer detours around impermeable obstacles (i.e. their open space is more connected) that are measurable as lower retardation  $R$ . Further, small proteins sense more obstacle surface than larger ones (higher surface-to-volume values  $S/V$ ). The apparent viscosity  $\eta_{app}$  of the cellular fluid is lower for smaller proteins than for larger ones, since smaller components of the cellular interior appear for them as immobile obstacles whereas the same components enhance the apparent viscosity for larger proteins. Accordingly, their mean diffusive displacement  $\lambda$  between two consecutive collisions with obstacles is smaller.

The dynamic compartmentalization mechanism of chromatin unraveled here has important implications for the kinetics of enzymatic reactions, the target search process of proteins and the formation of chromatin states with different epigenetic modifications patterns and protein composition. In particular, permeation of small enzymes into distinct chromatin pores represents a simple but highly efficient mechanism to guide enzymatic reactions within compartments that are not partitioned by membranes. This mechanism might explain the differential enzymatic endowment in various parts of chromatin that serve distinct functions. Examples are the lamina-associated domains (Kind and van Steensel, 2010), the perichromatin compartment (Cremer and Cremer, 2010) or pericentric heterochromatin (Grewal and Jia, 2007). In these nuclear domains crucial enzymatic activities like transcription or recombination function very differently (Agmon et al., 2013;

Feuerbach et al., 2002) although the same soluble enzymes like polymerases or chromatin modifiers can access them. Thus, size-dependent protein mobility and permeability of chromatin are important aspects for the establishment of spatial patterns. This could include the formation of epigenetic patterns that are generated by the local enrichment or depletion of differently-sized complexes with distinct enzymatic activity that range from 100 kDa to several MDa in molecular weight as discussed recently for histone (de)methylases (Erdel et al., 2013).

#### ***V.4 Perspectives and conclusions***

Cells can dynamically regulate the accessibility to different compartments by adapting the compaction state and the plasticity of their nanostructure (Görisch et al., 2005; Hihara et al., 2012). As shown above, the multi-scale spatial FCCS approach developed here allows for noninvasively measuring the interplay between intracellular structure and diffusive protein transport. It can be used to investigate numerous other biological systems in addition to those described here. For example, a change from open and plastic chromatin structure to a more compact state was observed for the differentiation of embryonic stem cells, which is accompanied by a reduction of global histone acetylation (Gaspar-Maia et al., 2011). The more open chromatin state in embryonic stem cells was linked to an altered gene expression profile that is characterized by low-level expression of a large number of genes, which is referred to as “promiscuous transcription”, which is correlated with an increased mobility and accessibility of protein factors. Further, it was found here that treatment of U2OS cells with the DNA-intercalating drug chloroquine used for treatment of malaria significantly changes diffusive protein transport and accessibility within the nucleus. Likewise, other DNA intercalators like doxorubicin that is used for anticancer chemotherapies are expected to exert similar effects on chromatin structure. Thus, the altered protein mobility could be relevant to the clinical activities of these drugs in addition to their established mode of action. It is suggested that the multi-scale spatial FCCS methodology developed here can be a valuable tool for drug researchers to measure the impact of the intracellular structure’s compaction and plasticity state on the activity of different drugs.

Furthermore, it is noted that the integration of the second detection channel for red fluorescent light into the optical setup of the line-confocal microscope opens up another large field of application. It can be used for imaging the (co)localization of green and red

fluorescently labeled molecules in living cells as demonstrated in a proof-of-concept experiment for STAT1 and STAT2 proteins (Figure 50). Further, the dimerization of STAT1 and STAT2 proteins in the cytoplasm of human U2OS cells could be evaluated by dual-color FCCS. However, the full potential of 1D-FCS measurements with the line-confocal microscope was not taken advantage of since AC and CC curves were averaged due to the limited brightness of the fluorescent protein LSSmKate2. With an approach improved in this respect, spatially resolved protein interaction mapping, i.e. mapping of dissociation equilibrium constants will be feasible, which is highly relevant because the local molecular crowding impacts on the formation of molecular complexes (Ellis, 2001; Minton, 2001; Rivas et al., 2001; Zimmerman and Minton, 1993). Spatially resolved interaction mapping with dual-color 1D-FCS will thus be applicable to measure dimerization of STAT proteins in the nucleus of interferon-stimulated cells.

Another future extension of the present work would be to combine spatial FCCS analysis and dual-color FCCS analysis of fluorescence signals in a single experiment. Dual-color spatial FCCS allows for simultaneous measurement of the mobility of proteins and their complexes on multiple time and length scales. Thus, differences in the sensed cellular environment could be detected. Additionally, the kinetic dissociation rates of molecular complexes could be determined in living cells by measuring the lifetimes of these complexes. This approach could be used to dissect anomalous diffusion in relation to a so-called strange kinetics of reactions in cells (Shlesinger et al., 1993). Thus, one or two-color spatial FCCS yields experimental data for the scale dependence of diffusive molecule transport as well as protein association properties. It provides a novel approach to dissect inherent protein mobility, spatial confinements due to the intracellular environment and binding interactions with other proteins or nucleic acids, which is not possible with current fluorescence microscopy based approach. Thus, essential information is obtained for deriving quantitative descriptions of cellular functions in systems biology approaches.

## **VI Materials and Methods**

### **Fluorescence microscopy and spectroscopy**

Imaging and 1D-FCS measurements were performed on a further developed optical setup of a custom-made line-confocal microscope that had been introduced previously as Spatial and Temporal Fluctuation Microscope (STFM) (Heuvelman et al., 2009). The STFM continuously illuminates a line-shaped volume in the sample with coherent light at 488 nm from a continuous wave solid-state laser with 200 mW output power (Coherent). Emitted fluorescence signals from multiple detection volumes equally distributed along a line are recorded on pixels of a high quantum efficiency electron multiplying charge-coupled device (EM-CCD) camera (iXon Ultra DU-897, Andor Technology). Additionally, an acousto-optical tunable filter (AOTFnc-400.650, AA Opto-Electronic) was integrated into the microscopy system to minimize unintentional bleaching of fluorescence dyes by fine-adjustment of the illuminating laser beam power. Fluorescence signals of more than hundred detection volumes equally distributed on a line in the sample were detected on an EM-CCD pixel array detector and recorded on a personal computer via USB connection. For imaging, the illumination laser beam was deflected by a galvanometric mirror (GSI Lumonics) to scan a two-dimensional region of interest with the illumination line in one dimension. Integration of a commercially available optical component (OptoSplit II LS Image Splitter, Cairn Research) allowed for simultaneous imaging of two fluorescence emission wavelengths on the same EM-CCD camera's detector chip. The optical pathway in the OptoSplit II component was inspired by (Kinosita et al., 1991). It was optimized for imaging and 1D-FCS data acquisition of GFP and RFP by including a dichroic mirror that splits the green and red fluorescence light at 560 nm (HC – Beamsplitter BS 560 imaging, BFi OPTiLAS), a bandpass filter with a wavelength range between 500 nm and 550 nm (Bandpass ET 525/50m, BFi OPTiLAS) and a long pass filter (Edge Basic Long Pass Filter 561 LP, BFi OPTiLAS).

### **STFM Data Acquisition Software (STFM DAQS)**

Fluorescence images and data for 1D-FCS measurements were acquired by using software with graphical user interface (GUI) that was developed in this thesis. It allows for setting of camera acquisition parameters and the laser illumination intensity as well as controlling of the galvanometric mirror for imaging. Data are read from the EM-CCD camera and



either displayed in the profile panel for 1D-FCS measurements or in the image panel for imaging of the GUI. Further, users can toggle between the red and green detection channel of the line-confocal microscope.

The software was written in C# with Microsoft Visual Studio 2013 by using the NI Measurement Studio suite (National Instruments). A data input and output PCI board (NI PCI-6251, National Instruments) was used to control the galvanometric mirror and the AOTF. The EM-CCD camera was controlled with the Andor Software Development Kit (Andor Technology). The GUI of the STFM DAQS is shown in Figure 54.

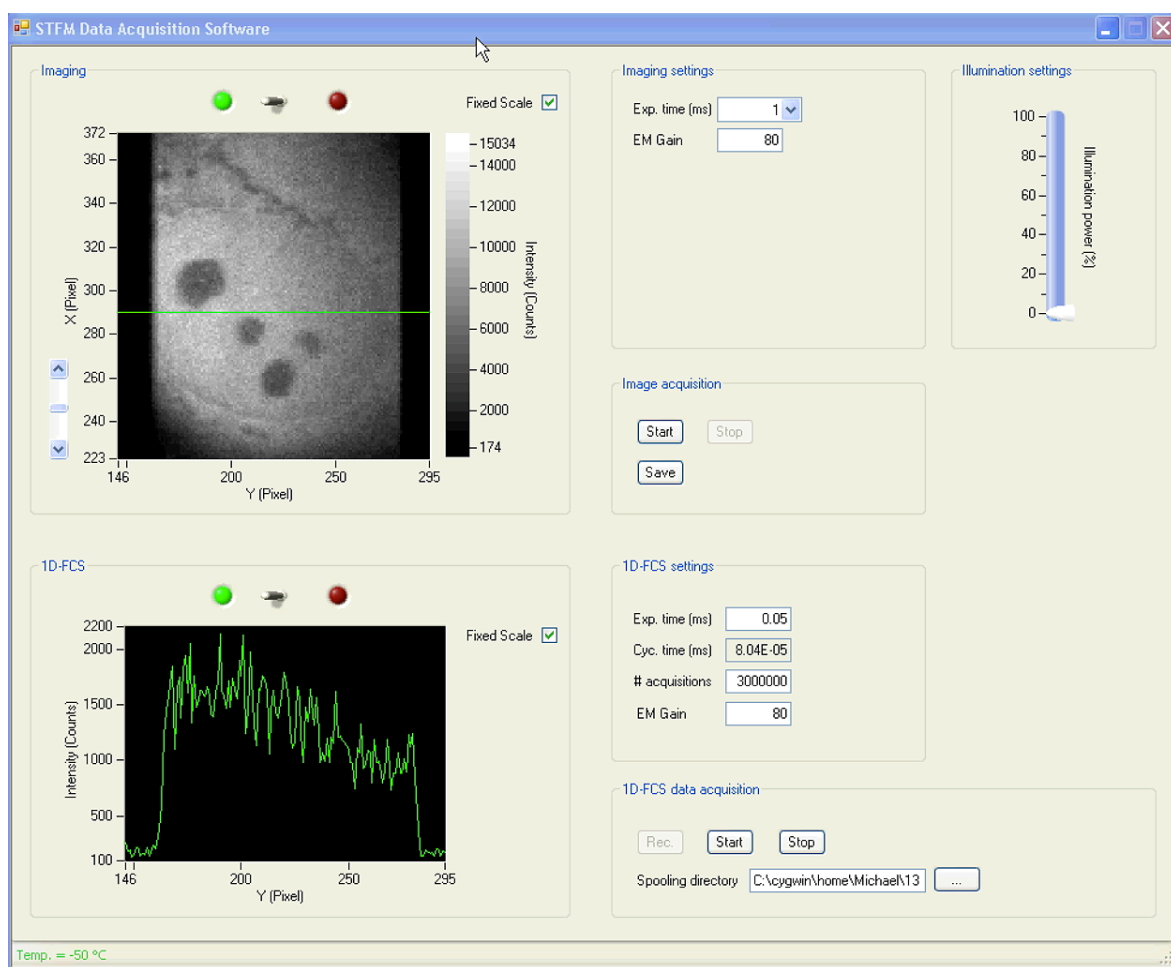


**Figure 54:** Graphical user interface (GUI) of the STFM Data Acquisition Software (STFM DAQS). Acquired fluorescence images are displayed in the imaging panel. Fluorescence profiles at the position of the green line cursor of the imaging panel are shown in the 1D-FCS panel. Users can toggle in both display panels between the green and the red detection channel of the line-confocal microscope. Further, the scaling is adaptable in both panels. Additionally, the imaging and 1D-FCS measurement parameters can be changed in the imaging and 1D-FCS settings control panels, respectively. The laser intensity can be controlled in the illumination settings panel.

### **Data processing and spatiotemporal analysis**

Acquired fluorescence signals of 1D-FCS measurements were trend-corrected according to a Fourier transformation-based approach developed in this thesis. For this purpose, the acquired signals were transformed with a fast Fourier transformation (FFT) routine and the resulting spectra were fitted by a least squares fitting routine of the GNU Scientific Library (GSL) (Galassi et al., 2003) on a computer cluster.

Trend-corrected fluorescence signals were analyzed by calculating the auto-correlation curves of each acquired signal and cross-correlation curves of each combination of signals from different detection volumes for a given separation distance as described previously (Heuvelman et al., 2009). Due to the large number of correlations, these were calculated by parallelized jobs on a computer cluster.

Further, the model function that describes the acquired correlation curves (Eq. 92) required numerical solution of a double integral, which was accomplished with a multidimensional numerical integration algorithm extension to the GNU Scientific Library (GSL) (Galassi et al., 2003). Fitting of the non-linear model function to the calculated correlation curves was done with a least-squares minimization algorithm of the GSL. Correlation curves were fitted with self-written software in C++ on a compute cluster. Results of the correlation analysis and least squares fitting routine were further processed and plotted with MATLAB (The MathWorks).

### **Sample preparation**

Measurements of the line-confocal microscopes MDE were carried out by acquiring image stacks of 100-nm-diameter fluorescent beads with an excitation maximum at 505 nm and an emission maximum at 515 nm (yellow-green carboxylate-modified FluoSpheres, Molecular Probes). FluoSpheres were fixed on Poly-L-lysine (Sigma-Aldrich) coated cover slides. Additionally, 13-nm-diameter fluorescent quantum dots with an emission maximum at 525 nm (yellow-green streptavidin conjugated QDots, Invitrogen) were used as fluctuating point light sources. QDots were immobilized on biotinylated bovine serum albumin (BSA) coated LabTek chambered coverglasses (Nunc) by incubating a 0.3 nM QDot solution for 1 hour. Unbound QDots were removed by rinsing the slides with 1× PBS buffer and water.

FCS measurements were conducted in LabTek chambers. The *in vitro* measurements were conducted with a solution of QDots in water or purified GFP diluted in 1x PBS buffer at

---

concentrations of 20 nM or 100 nM, respectively. For studies in living cells, GFP multimer plasmids (Pack et al., 2006) were transfected into human U2OS cells with Effectene (Qiagen). Cells were cultured in DMEM supplemented with penicillin-streptomycin and 10% fetal bovine serum at 37 °C and 5% CO<sub>2</sub>. For perturbation experiments, U2OS cells were incubated with either 8 μM Cytochalasin D for 20 minutes, 10 μM Nocodazole for 30 minutes, 2 μM Withaferin A for 3 hours, 400 nM TSA for 18 hours, or Chloroquine for 12 hours. The perturbations were validated based on the distribution of overexpressed β-Actin-mRFP, mCherry-MAP4 or GFP-Vimentin that was observed by confocal fluorescence imaging.

For constructing the STAT2-GFP plasmid, the coding sequence of human STAT2 was cloned into a pEGFP-N1 backbone (Clontech) via KpnI and AgeI. For constructing the CD-GFP plasmid, the chromodomain of human HP1β (aa 1- 69) was cloned into a pEGFP-N1 backbone (Clontech) via BglII and HindIII.

## VII References

- Agmon, N., Liefshitz, B., Zimmer, C., Fabre, E., and Kupiec, M. (2013). *Effect of nuclear architecture on the efficiency of double-strand break repair*. *Nat Cell Biol* **15**, 694-699.
- Alberts, B., Johnson, A., Lewis, J., Raff, M., Roberts, K., and Walter, P. (2002). *Molecular Biology of the Cell*, 4 edn (Garland Science).
- Axelrod, D., Koppel, D. E., Schlessinger, J., Elson, E., and Webb, W. W. (1976). *Mobility measurement by analysis of fluorescence photobleaching recovery kinetics*. *Biophys J* **16**, 1055-1069.
- Bacia, K., Kim, S. A., and Schwille, P. (2006). *Fluorescence cross-correlation spectroscopy in living cells*. *Nat Methods* **3**, 83-89.
- Bancaud, A., Huet, S., Daigle, N., Mozziconacci, J., Beaudouin, J., and Ellenberg, J. (2009). *Molecular crowding affects diffusion and binding of nuclear proteins in heterochromatin and reveals the fractal organization of chromatin*. *EMBO J* **28**, 3785-3798.
- Banks, D. S., and Fradin, C. (2005). *Anomalous diffusion of proteins due to molecular crowding*. *Biophys J* **89**, 2960-2971.
- Berg, H. C. (1993). *Random walks in biology* (Princeton University Press).
- Berland, K. M., So, P. T., and Gratton, E. (1995). *Two-photon fluorescence correlation spectroscopy: method and application to the intracellular environment*. *Biophys J* **68**, 694-701.
- Bernardi, R., and Pandolfi, P. P. (2007). *Structure, dynamics and functions of promyelocytic leukaemia nuclear bodies*. *Nat Rev Mol Cell Biol* **8**, 1006-1016.
- Bhawalkar, J. D., Shih, A., Pan, S. J., Liou, W. S., Swiatkiewicz, J., Reinhardt, B. A., Prasad, P. N., and Cheng, P. C. (1996). *Two-photon laser scanning fluorescence microscopy-from a fluorophore and specimen perspective*. *Bioimaging* **4**, 168-178.
- Blonk, J. C. G., Don, A., Aalst, J. v., and Birmingham, J. J. (1993). *Fluorescence Photobleaching Recovery in the Confocal Scanning Light Microscope*. *J Microscopy* **169**, 363-374.
- Boisvert, F., van Koningsbruggen, S., Navascués, J., and Lamond, A. (2007). *The multifunctional nucleolus*. *Nat Rev Mol Cell Biol* **8**, 574-585.
- Born, M., Wolf, E. (1999). *Principles of Optics: Electromagnetic Theory of Propagation, Interference and Diffraction of Light* 7th (expanded) edn (Cambridge University Press).

- 
- Bouchaud, J.-P., and Georges, A. (1990). *Anomalous diffusion in disordered media: statistical mechanisms, models, and physical applications*. Phys Reports **195**, 127-193.
- Braeckmans, K., Peeters, L., Sanders, N. N., De Smedt, S. C., and Demeester, J. (2003). *Three-dimensional fluorescence recovery after photobleaching with the confocal scanning laser microscope*. Biophys J **85**, 2240-2252.
- Braga, J., Desterro, J. M., and Carmo-Fonseca, M. (2004). *Intracellular macromolecular mobility measured by fluorescence recovery after photobleaching with confocal laser scanning microscopes*. Mol Biol Cell **15**, 4749-4760.
- Brehm, A., Tufteland, K. R., Aasland, R., and Becker, P. B. (2004). *The many colours of chromodomains*. Bioessays **26**, 133-140.
- Brinkmeier, M., Dorre, K., Stephan, J., and Eigen, M. (1999). *Two beam cross correlation: A method to characterize transport phenomena in micrometer-sized structures*. Anal Chem **71**, 609-616.
- Brown, E. B., Wu, E. S., Zipfel, W., and Webb, W. W. (1999). *Measurement of molecular diffusion in solution by multiphoton fluorescence photobleaching recovery*. Biophys J **77**, 2837-2849.
- Bunde, A., and Havlin, S., eds. (1995). *Fractals and Disordered Systems*, 2nd edn (Berlin, Springer-Verlag).
- Busch, N. A., Kim, T., and Bloomfield, V. A. (2000). *Tracer diffusion of proteins in DNA solutions. 2. Green fluorescent protein in crowded DNA solutions*. Macromolecules **33**, 5932-5937.
- Capoulade, J., Wachsmuth, M., Hufnagel, L., and Knop, M. (2011). *Quantitative fluorescence imaging of protein diffusion and interaction in living cells*. Nature biotechnology **29**, 835-839.
- Chung, I., Osterwald, S., Deeg, K. I., and Rippe, K. (2012). *PML body meets telomere: the beginning of an ALternate ending?* Nucleus **3**, 263-275.
- Cioce, M., and Lamond, A. (2005). *Cajal bodies: a long history of discovery*. Annu Rev Cell Dev Biol **21**, 105-131.
- Condamin, S., Tejedor, V., Voituriez, R., Benichou, O., and Klafter, J. (2008). *Probing microscopic origins of confined subdiffusion by first-passage observables*. Proc Natl Acad Sci U S A **105**, 5675-5680.
- Cooper, J. A. (1987). *Effects of cytochalasin and phalloidin on actin*. J Cell Biol **105**, 1473-1478.

- Cremer, T., and Cremer, C. (2001). *Chromosome Territories, Nuclear Architecture and Gene Regulation in Mammalian Cells*. Nat Rev Genet **2**, 292-301.
- Cremer, T., and Cremer, M. (2010). *Chromosome territories*. Cold Spring Harbor perspectives in biology **2**, a003889.
- De Sweit, T. M., and Sen, P. N. (1996). *Time dependent diffusion coefficient in a disordered medium*. J Chem Phys **104**, 14.
- Denk, W., Strickler, J. H., and Webb, W. W. (1990). *Two-photon laser scanning fluorescence microscopy*. Science **248**, 73-76.
- Dertinger, T., Loman, A., Ewers, B., Muller, C. B., Kramer, B., and Enderlein, J. (2008). *The optics and performance of dual-focus fluorescence correlation spectroscopy*. Opt Express **16**, 14353-14368.
- Dertinger, T., Pacheco, V., von der Hocht, I., Hartmann, R., Gregor, I., and Enderlein, J. (2007). *Two-focus fluorescence correlation spectroscopy: a new tool for accurate and absolute diffusion measurements*. Chemphyschem **8**, 433-443.
- Digman, M. A., and Gratton, E. (2009). *Imaging barriers to diffusion by pair correlation functions*. Biophys J **97**, 665-673.
- Dittrich, P. S., and Schuille, P. (2002). *Spatial two-photon fluorescence cross-correlation spectroscopy for controlling molecular transport in microfluidic structures*. Anal Chem **74**, 4472-4479.
- Dross, N., Spriet, C., Zwerger, M., Muller, G., Waldeck, W., and Langowski, J. (2009). *Mapping eGFP oligomer mobility in living cell nuclei*. PLoS One **4**, e5041.
- Dusch, E., Dorval, T., Vincent, N., Wachsmuth, M., and Genovesio, A. (2007). *Three-dimensional point spread function model for line-scanning confocal microscope with high-aperture objective*. J Microsc **228**, 132-138.
- Einstein, A. (1905). *Über die von der molekularkinetischen Theorie der Wärme geforderte Bewegung von in ruhenden Flüssigkeiten suspendierten Teilchen*. Annalen der Physik **17**, 549-560.
- Ellgaard, L., and Helenius, A. (2001). *ER quality control: towards an understanding at the molecular level*. Curr Opin Cell Biol **13**, 431-437.
- Ellis, R. J. (2001). *Macromolecular crowding: obvious but underappreciated*. Trends Biochem Sci **26**, 597-604.
- Ellis, R. J., and Minton, A. P. (2003). *Cell biology: join the crowd*. Nature **425**, 27-28.
- Elson, E. L., and Magde, D. (1974). *Fluorescence correlation spectroscopy. I. Conceptual basis and theory*. Biopolymers **13**, 1-27.

- 
- Enderlein, J., Gregor, I., Patra, D., Dertinger, T., and Kaupp, U. P. (2005). *Performance of Fluorescence Correlation Spectroscopy for Measuring Diffusion and Concentration*. ChemPhysChem **6**, 2324-2336.
- Enderlein, J., Gregor, I., Patra, D., and Fitter, J. (2004). *Art and artefacts of fluorescence correlation spectroscopy*. Curr Pharm Biotechnol **5**, 155-161.
- Erdel, F. (2012) *Tracing the Activity of ISWI Chromatin Remodelers in Living Cells with Fluorescence Fluctuation Microscopy based Approaches*, PhD thesis, Ruprecht-Karls-Universität Heidelberg, Heidelberg.
- Erdel, F., Müller-Ott, K., Baum, M., Wachsmuth, M., and Rippe, K. (2011). *Dissecting chromatin interactions in living cells from protein mobility maps*. Chromosome Res **19**, 99-115.
- Erdel, F., Muller-Ott, K., and Rippe, K. (2013). *Establishing epigenetic domains via chromatin-bound histone modifiers*. Ann N Y Acad Sci, in press.
- Erdel, F., and Rippe, K. (2012). *Quantifying transient binding of ISWI chromatin remodelers in living cells by pixel-wise photobleaching profile evolution analysis*. Proc Natl Acad Sci U S A **109**, E3221-3230.
- Fejes Tóth, K., Knoch, T. A., Wachsmuth, M., Stöhr, M., Frank-Stöhr, M., Bacher, C. P., Müller, G., and Rippe, K. (2004). *Trichostatin A induced histone acetylation causes decondensation of interphase chromatin*. J Cell Sci **117**, 4277-4287.
- Feuerbach, F., Galy, V., Trelles-Sticken, E., Fromont-Racine, M., Jacquier, A., Gilson, E., Olivo-Marin, J. C., Scherthan, H., and Nehrbass, U. (2002). *Nuclear architecture and spatial positioning help establish transcriptional states of telomeres in yeast*. Nat Cell Biol **4**, 214-221.
- Fick, A. (1855). *Über Diffusion*. Ann Phys **94**, 59-86.
- Fletcher, D. A., and Mullins, R. D. (2010). *Cell mechanics and the cytoskeleton*. Nature **463**, 485-492.
- Fokker, A. D. (1914). *Die mittlere Energie elektrischer Dipole im Strahlungsfeld*. Ann Phys **348**, 810-820.
- Fordham, E. J., Gibbs, S. J., and Hall, L. D. (1994). *Partially restricted diffusion in a permeable sandstone: observations by stimulated echo PFG NMR*. Magn Reson Imaging **12**, 279-284.
- Fritsch, C. C., and Langowski, J. (2010). *Anomalous diffusion in the interphase cell nucleus: the effect of spatial correlations of chromatin*. J Chem Phys **133**, 025101.
- Fussner, E., Ching, R. W., and Bazett-Jones, D. P. (2011). *Living without 30nm chromatin fibers*. Trends Biochem Sci **36**, 1-6.

- Galassi, M., Davies, J., Theiler, J., Gough, B., Jungman, G., Booth, M., and Rossi, F. (2003). *GNU Scientific Library: Reference Manual* (Network Theory Ltd.).
- Gaspar-Maia, A., Alajem, A., Meshorer, E., and Ramalho-Santos, M. (2011). *Open chromatin in pluripotency and reprogramming*. *Nat Rev Mol Cell Biol* **12**, 36-47.
- Gauthier, M. G., and Bechhoefer, J. (2009). *Control of DNA replication by anomalous reaction-diffusion kinetics*. *Phys Rev Lett* **102**, 158104.
- Gendron, P. O., Avaltroni, F., and Wilkinson, K. J. (2008). *Diffusion coefficients of several rhodamine derivatives as determined by pulsed field gradient-nuclear magnetic resonance and fluorescence correlation spectroscopy*. *J Fluoresc* **18**, 1093-1101.
- Görisch, S. M., Wachsmuth, M., Fejes Tóth, K., Lichter, P., and Rippe, K. (2005). *Histone acetylation increases chromatin accessibility*. *J Cell Sci* **118**, 5825-5834.
- Görisch, S. M., Wachsmuth, M., Ittrich, C., Bacher, C. P., Rippe, K., and Lichter, P. (2004). *Nuclear body movement is determined by chromatin accessibility and dynamics*. *Proc Natl Acad Sci USA* **101**, 13221-13226.
- Gorski, S. A., Dundr, M., and Misteli, T. (2006). *The road much traveled: trafficking in the cell nucleus*. *Curr Opin Cell Biol* **18**, 284-290.
- Gregor, I., Patra, D., and Enderlein, J. (2005). *Optical saturation in fluorescence correlation spectroscopy under continuous-wave and pulsed excitation*. *Chemphyschem* **6**, 164-170.
- Grewal, S. I., and Jia, S. (2007). *Heterochromatin revisited*. *Nat Rev Genet* **8**, 35-46.
- Grin, B., Mahammad, S., Wedig, T., Cleland, M. M., Tsai, L., Herrmann, H., and Goldman, R. D. (2012). *Withaferin A alters intermediate filament organization, cell shape and behavior*. *PLoS One* **7**, e39065.
- Guenther, R. (1990). *Modern optics* (John Wiley & Sons).
- Guigas, G., Kalla, C., and Weiss, M. (2007). *The degree of macromolecular crowding in the cytoplasm and nucleoplasm of mammalian cells is conserved*. *FEBS Lett* **581**, 5094-5098.
- Guigas, G., and Weiss, M. (2008). *Sampling the cell with anomalous diffusion - the discovery of slowness*. *Biophys J* **94**, 90-94.
- Handwerger, K., and Gall, J. (2006). *Subnuclear organelles: new insights into form and function*. *Trends Cell Biol* **16**, 19-26.
- Haupts, U., Maiti, S., Schwille, P., and Webb, W. W. (1998). *Dynamics of fluorescence fluctuations in green fluorescent protein observed by fluorescence correlation spectroscopy*. *Proc Natl Acad Sci USA* **95**, 13573-13578.



- 
- Havlin, S., Djordjevic, Z. V., Majid, I., Stanley, H. E., and Weiss, G. H. (1984). *Relation between dynamic transport properties and static topological structure for the lattice-animal model of branched polymers*. Phys Rev Lett **53**, 178-181.
- Hecht, E. (1989). *Optics* (Addison Wesley Longmann Inc. ).
- Helmchen, F., and Denk, W. (2005). *Deep tissue two-photon microscopy*. Nat Methods **2**, 932-940.
- Hess, S. T., and Webb, W. W. (2002). *Focal volume optics and experimental artifacts in confocal fluorescence correlation spectroscopy*. Biophys J **83**, 2300-2317.
- Heuvelman, G., Erdel, F., Wachsmuth, M., and Rippe, K. (2009). *Analysis of protein mobilities and interactions in living cells by multifocal fluorescence fluctuation microscopy*. Eur Biophys J **38**, 813-828.
- Hihara, S., Pack, C. G., Kaizu, K., Tani, T., Hanafusa, T., Nozaki, T., Takemoto, S., Yoshimi, T., Yokota, H., Imamoto, N., *et al.* (2012). *Local nucleosome dynamics facilitate chromatin accessibility in living mammalian cells*. Cell Rep **2**, 1645-1656.
- Hinde, E., Cardarelli, F., Digman, M. A., and Gratton, E. (2010). *In vivo pair correlation analysis of EGFP intranuclear diffusion reveals DNA-dependent molecular flow*. Proc Natl Acad Sci U S A **107**, 16560-16565.
- Hinde, E., Cardarelli, F., Digman, M. A., and Gratton, E. (2012). *Changes in chromatin compaction during the cell cycle revealed by micrometer-scale measurement of molecular flow in the nucleus*. Biophys J **102**, 691-697.
- Hofling, F., and Franosch, T. (2013). *Anomalous transport in the crowded world of biological cells*. Rep Prog Phys **76**, 046602.
- Hwang, L. C., and Wohland, T. (2004). *Dual-color fluorescence cross-correlation spectroscopy using single laser wavelength excitation*. Chemphyschem **5**, 549-551.
- Jordan, M. A., Thrower, D., and Wilson, L. (1992). *Effects of vinblastine, podophyllotoxin and nocodazole on mitotic spindles. Implications for the role of microtubule dynamics in mitosis*. J Cell Sci **102** ( Pt 3), 401-416.
- Kamal, A., and Goldstein, L. S. (2000). *Connecting vesicle transport to the cytoskeleton*. Curr Opin Cell Biol **12**, 503-508.
- Kind, J., and van Steensel, B. (2010). *Genome-nuclear lamina interactions and gene regulation*. Curr Opin Cell Biol **22**, 320-325.
- Kinosita, K., Jr., Itoh, H., Ishiwata, S., Hirano, K., Nishizaka, T., and Hayakawa, T. (1991). *Dual-view microscopy with a single camera: real-time imaging of molecular orientations and calcium*. J Cell Biol **115**, 67-73.

- Klonis, N., Rug, M., Harper, I., Wickham, M., Cowman, A., and Tilley, L. (2002). *Fluorescence photobleaching analysis for the study of cellular dynamics*. Eur Biophys J **31**, 36-51.
- Kues, T., Peters, R., and Kubitscheck, U. (2001). *Visualization and tracking of single protein molecules in the cell nucleus*. Biophys J **80**, 2954-2967.
- Lakowicz, J. R. (2006). *Principles of Fluorescence Spectroscopy*, 3 edn (Springer).
- Latour, L. L., Svoboda, K., Mitra, P. P., and Sotak, C. H. (1994). *Time-dependent diffusion of water in a biological model system*. Proc Natl Acad Sci U S A **91**, 1229-1233.
- Lavalette, D., Tetreau, C., Tourbez, M., and Blouquit, Y. (1999). *Microscopic viscosity and rotational diffusion of proteins in a macromolecular environment*. Biophys J **76**, 2744-2751.
- Loskutov, V. V., and Sevriugin, V. A. (2013). *A novel approach to interpretation of the time-dependent self-diffusion coefficient as a probe of porous media geometry*. J Magn Reson **230**, 1-9.
- Luby-Phelps, K. (1994). *Physical properties of cytoplasm*. Curr Opin Cell Biol **6**, 3-9.
- Luby-Phelps, K., Taylor, D. L., and Lanni, F. (1986). *Probing the structure of cytoplasm*. J Cell Biol **102**, 2015-2022.
- Lukacs, G. L., Haggie, P., Seksek, O., Lechardeur, D., Freedman, N., and Verkman, A. S. (2000). *Size-dependent DNA mobility in cytoplasm and nucleus*. J Biol Chem **275**, 1625-1629.
- Maeshima, K., Hihara, S., and Eltsov, M. (2010). *Chromatin structure: does the 30-nm fibre exist in vivo?* Curr Opin Cell Biol **22**, 291-297.
- Magde, D., Elson, E. L., and Webb, W. W. (1972). *Thermodynamic fluctuations in a reacting system - measurement by fluorescence correlations spectroscopy*. Phys Rev Let **29**, 705-708.
- Magde, D., Elson, E. L., and Webb, W. W. (1974). *Fluorescence correlation spectroscopy. II. An experimental realization*. Biopolymers **13**, 29-61.
- Masuda, A., Ushida, K., and Okamoto, T. (2005). *New fluorescence correlation spectroscopy enabling direct observation of spatiotemporal dependence of diffusion constants as an evidence of anomalous transport in extracellular matrices*. Biophys J **88**, 3584-3591.
- Medintz, I. L., Uyeda, H. T., Goldman, E. R., and Mattoussi, H. (2005). *Quantum dot bioconjugates for imaging, labelling and sensing*. Nat Mater **4**, 435-446.
- Minton, A. P. (2001). *The influence of macromolecular crowding and macromolecular confinement on biochemical reactions in physiological media*. J Biol Chem **15**, 15.

- 
- Moeendarbary, E., Valon, L., Fritzsche, M., Harris, A. R., Moulding, D. A., Thrasher, A. J., Stride, E., Mahadevan, L., and Charras, G. T. (2013). *The cytoplasm of living cells behaves as a poroelastic material*. *Nat Mater* **12**, 253-261.
- Mueller, V., Honigsmann, A., Ringemann, C., Medda, R., Schwarzmann, G., and Eggeling, C. (2013). *FCS in STED microscopy: studying the nanoscale of lipid membrane dynamics*. *Methods Enzymol* **519**, 1-38.
- Müller, C. B., Loman, A., Pacheco, V., Koberling, F., Willbold, D., Richtering, W., and Enderlein, J. (2008). *Precise measurement of diffusion by multi-color dual-focus fluorescence correlation spectroscopy*. *EPL (Europhysics Letters)* **83**, 46001.
- Muller, C. B., Weiss, K., Richtering, W., Loman, A., and Enderlein, J. (2008). *Calibrating differential interference contrast microscopy with dual-focus fluorescence correlation spectroscopy*. *Opt Express* **16**, 4322-4329.
- Müller, K. P., Erdel, F., Caudron-Herger, M., Marth, C., Fodor, B. D., Richter, M., Scaranaro, M., Beaudouin, J., Wachsmuth, M., and Rippe, K. (2009). *Multiscale analysis of dynamics and interactions of heterochromatin protein 1 by fluorescence fluctuation microscopy*. *Biophys J* **97**, 2876-2885.
- Nirmal, M., Dabbousi, B. O., Bawendi, M. G., Macklin, J. J., Trautman, J. K., Harris, T. D., and Brus, L. E. (1996). *Fluorescence intermittency in single cadmium selenide nanocrystals*. *Nature* **383**, 802-804.
- Novikov, D. S., Fieremans, E., Jensen, J. H., and Helpert, J. A. (2011). *Random walk with barriers*. *Nat Phys* **7**, 508-514.
- Pack, C., Saito, K., Tamura, M., and Kinjo, M. (2006). *Microenvironment and effect of energy depletion in the nucleus analyzed by mobility of multiple oligomeric EGFPs*. *Biophys J* **91**, 3921-3936.
- Pawley, J. B., ed. (2006). *Handbook of biological confocal microscopy*, 3rd edn (New York, Springer).
- Petrusek, Z., and Schwille, P. (2008). *Precise measurement of diffusion coefficients using scanning fluorescence correlation spectroscopy*. *Biophys J* **94**, 1437-1448.
- Phair, R. D., and Misteli, T. (2000). *High mobility of proteins in the mammalian cell nucleus*. *Nature* **404**, 604-609.
- Phillips, R. J. (2000). *A hydrodynamic model for hindered diffusion of proteins and micelles in hydrogels*. *Biophys J* **79**, 3350-3353.
- Piatkevich, K. D., Hult, J., Subach, O. M., Wu, B., Abdulla, A., Segall, J. E., and Verkhusha, V. V. (2010). *Monomeric red fluorescent proteins with a large Stokes shift*. *Proc Natl Acad Sci U S A* **107**, 5369-5374.

- Planck, M. (1917). Sitzber Press Akad Wiss, 324-341.
- Platanias, L. C. (2005). *Mechanisms of type-I- and type-II-interferon-mediated signalling*. Nat Rev Immunol **5**, 375-386.
- Politz, J. C., Browne, E. S., Wolf, D. E., and Pederson, T. (1998). *Intranuclear diffusion and hybridization state of oligonucleotides measured by fluorescence correlation spectroscopy in living cells*. Proc Natl Acad Sci USA **95**, 6043-6048.
- Qian, H., and Elson, E. L. (1991). *Analysis of Confocal Laser-Microscope Optics for 3-D Fluorescence Correlation Spectroscopy*. Appl Opt **30**, 1185-1195.
- Rarbach, M., Kettling, U., Koltermann, A., and Eigen, M. (2001). *Dual-color fluorescence cross-correlation spectroscopy for monitoring the kinetics of enzyme-catalyzed reactions*. Methods **24**, 104-116.
- Reits, E. A., and Neefjes, J. J. (2001). *From fixed to FRAP: measuring protein mobility and activity in living cells*. Nat Cell Biol **3**, E145-147.
- Rigler, R., Mets, Ü., Widengren, J., and Kask, P. (1993). *Fluorescence correlation spectroscopy with high count rate and low background: analysis of translational diffusion*. Eur Biophys J **22**, 169-175.
- Rippe, K. (2000). *Simultaneous binding of two DNA duplexes to the NtrC-enhancer complex studied by two-color fluorescence cross-correlation spectroscopy*. Biochemistry **39**, 2131-2139.
- Rippe, K. (2007). *Dynamic organization of the cell nucleus*. Curr Opin Genet Dev **17**, 373-380.
- Rivas, G., Fernandez, J. A., and Minton, A. P. (2001). *Direct observation of the enhancement of noncooperative protein self- assembly by macromolecular crowding: Indefinite linear self-association of bacterial cell division protein FtsZ*. Proc Natl Acad Sci U S A **98**, 3150-3155.
- Rubtsova, S. N., Kondratov, R. V., Kopnin, P. B., Chumakov, P. M., Kopnin, B. P., and Vasiliev, J. M. (1998). *Disruption of actin microfilaments by cytochalasin D leads to activation of p53*. FEBS Lett **430**, 353-357.
- Saxton, M. J. (1994). *Anomalous diffusion due to obstacles: a Monte Carlo study*. Biophys J **66**, 394-401.
- Saxton, M. J. (1996). *Anomalous diffusion due to binding: a Monte Carlo study*. Biophys J **70**, 1250-1262.
- Schwille, P., Haupts, U., Maiti, S., and Webb, W. W. (1999a). *Molecular dynamics in living cells observed by fluorescence correlation spectroscopy with one- and two-photon excitation*. Biophys J **77**, 2251-2265.

- 
- Schwille, P., J., K., and Webb, W. W. (1999b). *Fluorescence correlation spectroscopy with single-molecule sensitivity on cell and model membranes*. *Cytometry* **36**, 176-182.
- Schwille, P., Meyer-Almes, F. J., and Rigler, R. (1997). *Dual-color fluorescence cross-correlation spectroscopy for multicomponent diffusional analysis in solution*. *Biophys J* **72**, 1878-1886.
- Sen, P. N. (2004). *Time-dependent diffusion coefficient as a probe of geometry*. *Concepts in Magnetic Resonance Part A* **23A**, 1-21.
- Sen, P. N., Schwartz, L. M., and Mitra, P. P. (1994). *Probing the structure of porous media using NMR spin echoes*. *Magn Reson Imaging* **12**, 227-230.
- Sheppard, C. J. R., and Matthews, H. J. (1987). *Imaging in high-aperture optical systems*. *J Opt Soc Am A* **4**, 1354-1360.
- Shlesinger, M. F., Zaslavsky, G. M., and Klafter, J. (1993). *Strange kinetics*. *Nature* **363**, 31-37.
- Singh, A. P., Krieger, J. W., Buchholz, J., Charbon, E., Langowski, J., and Wohland, T. (2013). *The performance of 2D array detectors for light sheet based fluorescence correlation spectroscopy*. *Opt Express* **21**, 8652-8668.
- Stark, G. R., and Darnell, J. E., Jr. (2012). *The JAK-STAT pathway at twenty*. *Immunity* **36**, 503-514.
- Stelzer, E. H. K., and Lindek, S. (1994). *Fundamental reduction of the observation volume in far-field light microscopy by detection orthogonal to the illumination axis: confocal theta microscopy*. *Opt Commun* **111**, 536-547.
- Stewart, I. (2001). *Mathematics. Where drunkards hang out*. *Nature* **413**, 686-687.
- Toiber, D., Erdel, F., Bouazoune, K., Silberman, D. M., Zhong, L., Mulligan, P., Sebastian, C., Cosentino, C., Martinez-Pastor, B., Giacosa, S., *et al.* (2013). *SIRT6 recruits SNF2H to DNA break sites, preventing genomic instability through chromatin remodeling*. *Mol Cell* **51**, 454-468.
- Vale, R. D., and Milligan, R. A. (2000). *The way things move: looking under the hood of molecular motor proteins*. *Science* **288**, 88-95.
- van Kampen, N. G., ed. (1992). *Stochastic processes in physics and chemistry*, 2nd edn (Amsterdam, Elsevier).
- Wachsmuth, M., Caudron-Herger, M., and Rippe, K. (2008). *Genome organization: Balancing stability and plasticity*. *Biochim Biophys Acta* **1783**, 2061-2079.

- Wachsmuth, M., Waldeck, W., and Langowski, J. (2000). *Anomalous diffusion of fluorescent probes inside living cell nuclei investigated by spatially-resolved fluorescence correlation spectroscopy*. J Mol Biol **298**, 677-689.
- Weidemann, T., Wachsmuth, M., Tewes, M., Rippe, K., and Langowski, J. (2002). *Analysis of ligand binding by two-colour fluorescence cross-correlation spectroscopy*. Single Mol **3**, 49-61.
- Weiss, M. (2003). *Stabilizing Turing patterns with subdiffusion in systems with low particle numbers*. Phys Rev E Stat Nonlin Soft Matter Phys **68**, 036213.
- Weiss, M., Elsner, M., Kartberg, F., and Nilsson, T. (2004). *Anomalous subdiffusion is a measure for cytoplasmic crowding in living cells*. Biophys J **87**, 3518-3524.
- Weiss, M., Hashimoto, H., and Nilsson, T. (2003). *Anomalous protein diffusion in living cells as seen by fluorescence correlation spectroscopy*. Biophys J **84**, 4043-4052.
- Wilhelm, S., Grobler, B., Gluch, M., and Heinz, H. (2003). *Confocal Laser Scanning Microscopy. Principles*. (ZEISS).
- Wohland, T., Shi, X., Sankaran, J., and Stelzer, E. H. (2010). *Single Plane Illumination Fluorescence Correlation Spectroscopy (SPIM-FCS) probes inhomogeneous three-dimensional environments*. Opt Express **18**, 10629.
- Woodcock, C. L., and Ghosh, R. P. (2010). *Chromatin higher-order structure and dynamics*. Cold Spring Harb Perspect Biol **2**, a000596.
- Zimmerman, S. B., and Minton, A. P. (1993). *Macromolecular crowding: biochemical, biophysical, and physiological consequences*. Annu Rev Biophys Biomol Struct **22**, 27-65.







## **Acknowledgments**

Ich bedanke mich bei allen, die mich während der Zeit meiner Doktorarbeit unterstützt haben. Insbesondere danke ich aber:

Priv.-Doz. Dr. Karsten Rippe für sein Vertrauen in mich und meine Arbeit - von ihm habe ich gelernt, bei den technischen Problemen des Laboralltages das große Ziel nicht aus den Augen zu verlieren,

Prof. Ulrich Schwarz für seine Bereitschaft, als Zweitgutachter für meine Arbeit und als Prüfer zur Verfügung zu stehen,

Prof. Annemarie Pucci und Prof. Christoph Cremer dafür, als Prüfer an meiner Verteidigung teilzunehmen,

meinen Kollegen in der AG Rippe für die angenehme Arbeitsatmosphäre und ihre Hilfsbereitschaft bei Fragen aller Art, besonders aber bei

Dr. Fabian Erdel, für viele inspirierende Diskussionen und die Beherbergung in Heidelberg, wenn es mir abends nicht mehr zurück nach Ulm gereicht hat,

meinen Eltern, meinen Brüdern und meinem Opa, weil sie immer für mich da sind, wenn ich sie brauche,

und natürlich meiner Freundin Sabrina für ihre Liebe und ihre Geduld während der Zeit des Schreibens, wenn ich mit den Gedanken noch bei der Arbeit war!





